UNIVERSITY OF Southampton

University of Southampton Research Repository

Copyright © and Moral Rights for this thesis and, where applicable, any accompanying data are retained by the author and/or other copyright owners. A copy can be downloaded for personal non-commercial research or study, without prior permission or charge. This thesis and the accompanying data cannot be reproduced or quoted extensively from without first obtaining permission in writing from the copyright holder/s. The content of the thesis and accompanying research data (where applicable) must not be changed in any way or sold commercially in any format or medium without the formal permission of the copyright holder/s.

When referring to this thesis and any accompanying data, full bibliographic details must be given, e.g.

Thesis: Author (Year of Submission) "Full thesis title", University of Southampton, name of the University Faculty or School or Department, PhD Thesis, pagination.

Data: Author (Year) Title. URI [dataset]

UNIVERSITY OF SOUTHAMPTON

FACULTY OF PHYSICAL SCIENCES AND ENGINEERING

ELECTRONICS AND COMPUTER SCIENCE

Integrated photonic crystals platform for biosensing

by

Jingxing Shi

Thesis for the degree of degree of Doctor of philosophy

January 2018

UNIVERSITY OF SOUTHAMPTON

ABSTRACT

FACULTY OF PHYSICAL SCIENCES AND ENGINEERING

School of Electronics and Computer Science

Thesis for the degree of Doctor of Philosophy

INTEGRATED PHOTONIC CRYSTALS PLATFORM FOR BIOSENSING

Jingxing Shi

Photonic crystals have been shown to be a promising technology for improving the performance of light emitting diodes, solar cells and optical communication components. More recently there has been interest in the application of photonic crystals for bio-chemical sensing since they provide the potential benefits of high sensitivity, label free, real time detection with low limit of detection. Optical sensing mechanisms such as Surface Plasmon Resonance (SPR), and Evanescent Field (EF) sensing methods are currently popular. These are all sensitive to small changes in refractive index (RI) of part of the device. To date SPR methods provide the highest level of sensitivity but have the disadvantage of requiring an expensive gold coating.

AROMA Sensor:

As a high sensitivity, low cost alternative to conventional SPR methods, this thesis investigates a new concept for bio-chemical sensing recently developed at Southampton, which uses vertical projection of leaky transmitted modes of a photonic crystal as the sensing method. We call this Angle Resolved Out-coupled Mode Analysis (AROMA). This method is highly sensitive to small changes in refractive index at the sidewalls of the holes of a photonic crystal resulting in a strong angular shift of an out coupled beam of light. Changes in RI causes a shift in the projected spot position that can be recorded by a CCD/ CMOS camera.

Sensor performance is shown to far exceed normal SPR. Simulation and experimental results demonstrate a sensitivity of 10 degree/RIU from a non-optimised sensor and simulation results indicate an improved sensitivity of 6500 degree/RIU by optimising the sensor operating point. Responsivity of the sensor was investigated by sequentially depositing a series of sub nm ZnO layers, and was found to be highly linear.

Photonic crystal coupler and system integration:

Apart from the sensor, a new concept for light coupling is developed and optimised. We extend photonic crystal technology to create a combined light coupler / splitter component allowing arbitrary N-channel light coupling to a simple slab waveguide device. The coupler is combined with multiple sensors to make a fully functional multi-channel (4-12 channels) sensor operating at 785nm. This is integrated into a high refractive index (n=1.7) Silicon Oxynitride (SiON) slab waveguide deposited onto a transparent borosilicate glass substrate. The aim for the slab waveguide was to mimic the refractive index of available polymer materials so that the entire system could eventually be fabricated on a flexible polymer substrate by nanoimprint lithography.

Design and modelling:

This thesis describes the design and optimisation of each component (sensor, coupler and slab waveguide), presenting in depth background physics and rigorous design methods for each component. 3D models were developed based on Rigorous Coupled Wave Analysis (RCWA) and Finite-Difference Time-Domain (FDTD) methods. RCWA models allowed accurate prediction and optimisation of light coupling and projection angles for any selected operating wavelength. FDTD methods allowed careful analysis of the interaction between the light field in the slab waveguide and materials placed in the holes. It also predicts the far-field projected beam pattern for the sensor.

Applications:

Capability to detect (dry) monolayer coatings was proven for a simple self-assembled monolayer molecule coating (p-tolyltrichlorosilane (TTCS)) and also deoxyribonucleic acid (DNA) was successfully detected, close to physiological levels. To achieve this a complex hybridisation process was developed. Sensor response as a function of self-assemble molecule (SAM) length and distance from the sidewalls was investigated in detail by using reversible chains of long chain charged molecules (lysine, poly-lysine, bovine serum albumin protein). A detector surface with a layer of poly-lysine-g-PEG was successfully replaced by a poly-lysine molecule with larger molecule weight. Sequentially additional bovine serum albumin protein binding with the Poly-lysine was detected.

Capability to detect biomolecules in an aqueous environment is intrinsically difficult for most bio-sensors. By fabricating the device on a transparent glass substrate, and designing the device to project light backwards through the substrate, it became possible to detect small changes in refractive index for liquids placed on the exposed top surface with no detriment to the readout

method. The bulk sensitivity of the sensor for liquids was evaluated by measuring a sequence of glucose solutions with increasing concentrations. A highly linear response was again observed.

Table of Contents

List of Tables

List of Figures

DECLARATION OF AUTHORSHIP

I, Jingxing Shi declare that this thesis and the work presented in it are my own and have been generated by me as the result of my own original research.

Integrated photonic crystals platform for biosensing

I confirm that:

1. This work was done wholly in candidature for a research degree at this University;
2. Where any part of this thesis has previously been submitted for a degree or any other qualification at this University or any other institution, this has been clearly stated;
3. Where I have consulted the published work of others, this is always clearly attributed;
4. Where I have quoted from the work of others, the source is always given. With the exception of such quotations, this thesis is entirely my own work;
5. I have acknowledged all main sources of help;
6. Where the thesis is based on work done by myself jointly with others, I have made clear exactly what was done by others and what I have contributed myself;
7. Parts of this work have been published as:

   Jingxing Shi, Michael Pollard, Cesar Angeles, RuiQi Chen, James Christopher Gates, Martin D. B. Charlton, "Photonic crystal and quasi-crystals providing simultaneous light coupling and beam splitting within a low refractive-index slab waveguide", Nature Scientific Report, vol.7, 1812(2017).

   Jingxing shi, Michael Pollard, James Christopher Gates, and Martin Charlton, “Design and fabrication quasiperiodic photonic crystals for simultaneous slab waveguide coupling and splitting, ” Cleo, JW2A.130, 2017.

   Huang-Yu Lin, Yung-Min Pai, **Jingxing Shi**, Xin-Yin Chen , Chuang-Hsiang Lin, Chi-Ming Weng, Tzu-Yu Chen, Chien-Chung Lin, Martin David Brian Charlton and Hao-Chung Kuo, “Optimization of nano-honeycomb structures for flexible w-LEDs,” Optics Express, vol. 25, 20466, 2017.

Signed: .....

Date: .....

Acknowledgements

First I would like to thank my supervisors Prof Martin Charlton and Dr James Gates for supporting me during the three years of my PhD life. Prof Martin Charlton, thank you for offering me a three year scholarship and the opportunity of studying in the interesting area of photonic crystals. Also thank you for offering me the opportunity to work in a high standard cleanroom to realize the devices in this thesis. Dr James Gates, thank you for sharing the knowledge about photonics and discussing the problems of fabrication and measurement.

I would like to thank Dr Michael Pollard, you are the pioneer of the quasicrystal photonic crystal. Thank you for sharing your knowledge and giving suggestions, even though the majority of our discussions were via email. I also would like to thank Dr Tracy Melvin for preparing the DNA sequences for me and offering me free access and permission to work in your bio-labs. Dr Jonathan West, thank you for your guidance in the field of biology sensing and our weekly meetings in the last half year in order to help me improve the quality of my experiments.

Thankyou Chirenjeevi and Tasmiat, you made PhD life less boring because of those funny and unforgettable stories. I would also like to thank ZiLong Wang, Zhuo Cao and JunYan Liao for the gym workouts and basketball games.

I would like to dedicate my thesis to my Dad and my family for their support and encouraging me to finish my PhD.

I need to thank you, mom and grandmamma during the three years. I know you are watching and guarding me in the heaven, you are the reason I always remind myself I need accomplish the PhD and never give up.

Definitions and Abbreviations

a	lattice pitch
n_{eff}	effective refractive index
Λ	point pitch
θ	angle (degrees)
k	wavevector
$k_{//}$	in-plane wavevector
c	speed of light
λ	free space wavelength
n	refractive index
E(r)	electric field profile
PhCs	photonic crystals
PhQCs/QPCs	photonic quasicrystals
FDTD	finite-difference time-domain
PML	perfectly matched layer
SEM	scanning electron microscope
PMMA	polymethylmethacrylate
f	fill factor / Fourier coefficient
$\hat{x}$, $\hat{y}$, $\hat{z}$	Cartesian unit vectors
G	Fourier space vector
H(r)	magnetizing field profile
RCWA	rigorous coupled wave analysis
MZI	Mach-Zehnder Interferometer
RIU	Refractive index unit

ALD	Atom layer deposition
SPR	Surface plasmon resonance
FNA	Fuming nitric acid
SAM	Self assemble molecule
SPW	Surface plasmon wave

Chapter 1: Introduction

The generation and manipulation of electromagnetic fields is the one of the most well understood area of science and consequently the most sophisticated field in engineering. All of these technologies are governed by Maxwell's equations, one of the most influential scientific discoveries that is still being exploited to develop new technologies on a daily basis. Researchers around the world have been pursuing new technologies to manipulate light. One of the most promising methods to control electromagnetic fields in the optical domain is by structuring materials at a length scale comparable to the wavelength of light. Such structures are call photonic crystals.

One application area of optics and photonics is bio-sensing. Different techniques have been investigated such as interferometric based refractive index sensing, Raman spectroscopy, reflectometry sensing and so on. Various optical components have been used to implement these techniques, for example waveguides, ring resonators, photonic crystals, prisms and gratings. Researchers have been trying to improve the performance of these devices, the most critical factors are the sensitivity, detection limit, level of integration and miniaturization.

The ultimate goal of this work is to research and develop a photonic crystals sensor for label free bio-sensing with the potential for mass production.

1.1 Light manipulation

Dense integration of optical components is desirable if not a key requirement to create mass-producible functional devices. High index contrast waveguides, power splitters (MMI or Y-junction) and grating couplers are widely used in integrated photonics as key components [1-7]. Waveguides are used for in-plane light confinement and route light to other functional components[8-10]. Grating couplers are often used as a route to couple light from free space into the waveguides and play another important role in order to overcome the mode mismatch issue between optical fibre and high index contrast waveguides. However, the integration of such components with a small footprint can result in complicated designs and fabrication processes. An alternative approach to provide the functionality previously discussed is photonic crystals. These have attracted much attention and have been used to improve device properties such as in light emitting diodes, solar cells and biological/chemical sensors.

Photonic crystals (PCs) are structured materials with refractive index periodically modulated in one, two or three dimensions. PCs can provide nonlinear dispersion and band gaps in one or more

directions. With correct designs (i.e. dielectric contrast, pitch of the lattice and size of the lattice points) a photonic crystal can prevent light, with a certain range of wavelengths, propagating through in the material in certain directions.

PCs can overcome some the problems of light propagating in conventional optical waveguides. Theoretically light can be guided without loss along a line defect of a two-dimensional PC with bends up to 120 degrees [11]. In addition, it is possible to guide light in the core layer of a fibre with refractive index lower than the cladding. PCs can also be used as two-dimensional grating couplers. They can not only provide light coupling between optical fibres and waveguides, but also power and polarization separation functionality[12-13][12][13][14]. The compatibility with integrated optics makes PCs a promising functional part in planar lightwave circuits (PLCs)[15]. To date the progress of integrating PCs with PLCs is slow, the reason is that a wide absolute bandgap in low refractive index materials is extremely hard to realize. High refractive index semiconductors such as silicon can be used but it suffers from high scattering loss. This issue is not inherent but due to the waveguide sidewall roughness and non-vertical wall profile[16]. The most successful application of the aforementioned PCs are highly efficient LEDs and solar cells [17], with developments in this area for more than 20 years.

Photonic Crystals are also proving to be a promising candidate in the bio/chemical sensing field. The sensing performance of most optic based sensors including Mach-Zehnder interferometers[18], grating waveguide structures[19] and optical ring resonators[20], relies on interaction with the evanescent field of the waveguide mode[21]. Molecular probes attached to the surface of the waveguide will affect the waveguide mode and permit detection. However, the main issue is that the interaction between the probe molecules and light is very limited. This exponentially decaying field extends into surrounding environment by only tens to hundreds of nanometres depending on the refractive index contrast. Most of the energy of the waveguide mode does not interact with the molecular probes. In addition, some methods like SPR require heavy metals (gold), which complicates fabrication process and increases the cost.

1.2 Bio-sensing methods

Bio-sensing as a detective technology for biological substances has been developed for decades. It takes advantage of biological components such as enzymes, antibodies and gene probes to recognise a specific target. Typically, such sensors are used in monitoring, which can be analysed easily such as via changes in the optical spectrum. Such sensors are used in monitoring and screening interactions of ligand-receptors such as the interaction between biotin and streptavidin and even studies on cell morphology. Moreover, such biosensors are not only applied to the

biological field but also environmental detection, medical treatment, public health and even food safety. Depending on the detection mechanism used in these devices, they can be divided into bio-electrode sensors, piezoelectric biosensors and optical based biosensors.

Optical sensors are powerful detection and analysis tools and are successfully commercialised in many fields including biomedical research, healthcare, and pharmaceutical and environmental monitoring. The different approaches can be divided into fluorescence-based detection and label-free detection.

Target molecules can be labelled with fluorescent tags (dyes) in fluorescence-based detection and the intensity of the fluorescence indicates the presence of target molecules and the interaction between the target molecule and bio-recognition molecules. The sensitivity of this approach is high, down to single molecules. The disadvantage of this approach is that the fluorescence labelling process may interfere with the biomolecule functions. Also quantitative analysis is hard to achieve due to the imprecise control of the number of phosphors or dye molecules on each molecule[22].

Alternatively, label-free detection is based on the natural characteristics of the target, which is easy, cheap and allows for quantitative measurement for molecular interaction. Such biosensor exploit optical methods of signal transduction, bypassing the requirement for fluorescent and enzymatic labels. For example the sample can be measured by observing refractive index (RI) changes[23], which are related to the sample concentration or the surface density. In that case the detection result will not be degraded when shrinking the sample volume. Besides, RI detection, optical absorption detection[24] and Raman spectroscopic detection[25] is also applied in label-free biosensors. The label-free method can exhibit enhanced sensitivity and specificity over labelling approaches. Using the example of an antigen and antibody binding event, such labels will interfere with the interaction and non-specifically adsorb on the surface thereby complicating the chemistry of the detection reaction. Among the different detection technologies, optical sensors are the most promising, as they can offer low limits of detection, high sensitivity and the ability to multiplex detection[26].

1.3 Motivation and novelty

Traditional analytical detection technologies are usually expensive, which is generally due to the high cost of the equipment and the long processing and detection time.

The aim of this thesis is to develop a compact, multi-parameter, high sensitivity, low cost and spectrometer free (easy readout) biosensor by integrating PCs structures onto a common slab-

waveguide technology platform. I am aiming to use PCs/QPCs to couple a single monochromatic light source into a planar waveguide and generate multi-parameter channels. The in-plane guided light will radiate out from PCs sensors, which are distributed in each channel path. The radiation angle is sensitive to the refractive index change of surroundings. A CMOS/CCD camera is used to monitor the change of radiated angle by translating projecting angle changes to radiation spot shift in pixels.

1.3.1 AROMA Sensor

As a high sensitivity, low cost alternative to conventional SPR methods, a new concept for bio-chemical sensing is developed (Figure 1). This uses vertical projection of leaky transmitted modes of a photonic crystal as the sensing method. We call this Angle Resolved Out-coupled Mode Analysis (AROMA). This method is highly sensitive to small changes in refractive index at the sidewalls of the holes of a photonic crystal resulting in a strong angular shift of an out coupled beam of light. Change in RI causes a shift in projected spot position which casn be recorded by a CCD camera.

1.3.2 Photonic crystal coupler and system integration

To allow extension to a multi-channel sensor we extend photonic crystal technology to create a combined light coupler / splitter component allowing arbitrary N-channel light coupling to a simple slab waveguide device. The coupler is combined with multiple sensors to make a fully functional multi-channel (2-12 channels) sensor operating at 785nm.

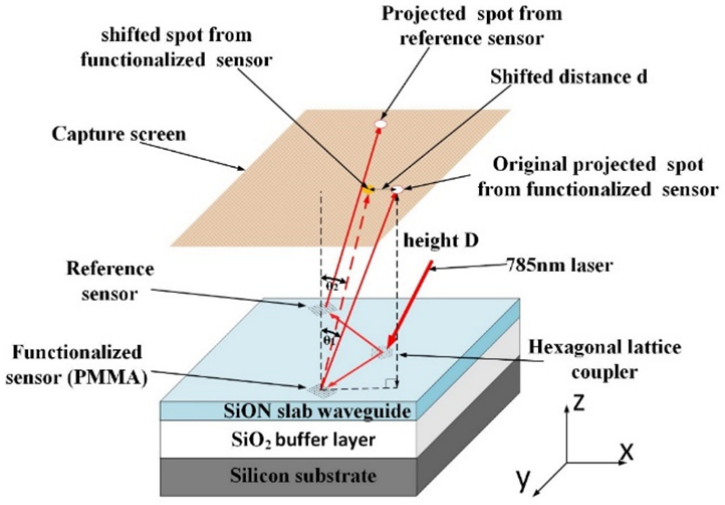

Figure 1 Shows the projection sensor concept, which is explained in detail in chapter 6. A multi-channel, multi parameter sensor device is developed by combining several sensors onto a common slab waveguide along with a single coupler/ splitter.

1.3.3 Slab waveguide and integration

This is integrated into a high refractive index (n=1.7) Silicon Oxynitride (SiON) slab waveguide deposited onto a transparent borosilicate glass substrsate. The aim for the slab waveguide was to mimic refractive index of available polymer materials so that the entire system could eventually be fabricated on a flexible polymer substrate by nanoimprint lithography. A schematic of quasi-crystal lattice coupler/splitter and slab waveguide integration is shown in Figure 2, which couples one monocolor laser beam and splits it into 12 sub beams in the slab waveguide.

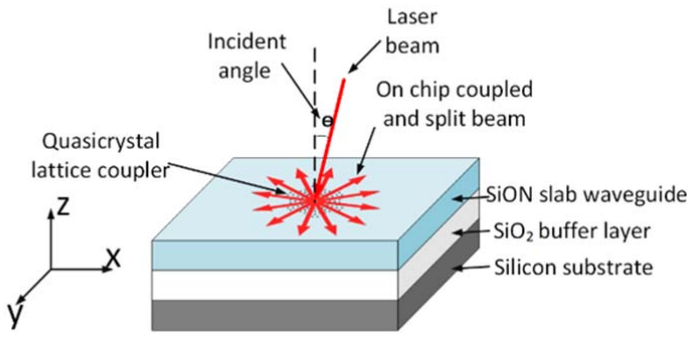

Figure 2. Shows a schematic of the coupler/splitter concept and slab waveguide configuration. This will be explained in detail in chapter 3.

1.4 Structure of the thesis

This thesis is divided into study of photonic crystals, literature review and original results. Chapter 2 introduces the basic background theory of photonic crystals. Chapter 3 reviews the progress in bio-sensing applications including electrochemical sensors and optical sensors. Chapter 4 illustrate the development of the photonic crystal coupler and beam splitter. Chapter 5 introduces the optimization of the vertical coupler for PC sensing system. Chapter 6 presents the sensing principle of PCs sensor (AROMA) and the simulation methodology. Chapter 7 describes the monolithic integration of the PC coupler and the PC sensor. Chapter 8 introduces the sensor performance and improvement. Chapter 9 testifies and calibrates the performance through a ZnO ALD experiment, SAM molecules and hybridization process of oligo-DNA probes. Chapter 10 describes how the sensor fabrication is transferred onto a glass substrate to achieve the goal of detection in an aqueous environment. Chapter 11 summarizes the development of the PC sensing system and introduces the future work.

.

Chapter 2: Background theory to photonic crystals

In this chapter, key physical concepts relating to photonic crystals (PCs) are introduced. By way of example, three lattices types are explained, and characteristics in real and reciprocal space introduced. Particular attention is paid to fundamental properties of PCs and the way that periodic structure modulates the propagated wave. The difference between ideal PCs with infinite height and real-world PCs slab is illustrated. The aperiodic PCs known as photonic quasicrystals (PQCs) has been investigated as a way to increasing symmetry and diffraction directions. Fabrication methods of these PCs are also introduced.

Two-dimensional PCs (4-fold Square lattice and 6-fold hexagonal lattice structure) are described in detail. This includes lattice structures in reciprocal lattice and in-plane interaction between lattice point (holes) and light. As an alternative, a true 12-fold PQCs with Stampfli-inflated tilling is introduced.

1. Light propagation in periodic media

A photonic crystal is defined as a crystal with dielectric constant that periodically varies spatially in certain directions. Back to 1887, an English physicist called Lord Rayleigh discovered that a band-gap exits in a periodic multilayer dielectric stacks. In the 1990s much attention was drawn to the research result about photonic crystals from Yablonovitch[17]and Sajeev John[27], subsequently the related research grew exponentially. However, researches were mainly theoretical due to the fabrication challenge at optical scales. In 1996, the first two-dimensional photonic crystal device, which operates in near infrared wavelengths, was demonstrated by Thomas Krauss[28], this led the way to fabricate photonic crystals in the same way that semiconductor devices are fabricated.

The concept of reciprocal lattice was first introduced by Josiah Willard Gibbs[29]. The reciprocal lattice is the Fourier transform of the periodic real spatial lattice, and so represents the lattice in frequency space (frequency space is often referred to as momentum or k-space). This is convenient because it allows simple analysis of interaction of waves with periodic structures through comparison of wave vector in relation to reciprocal lattice vector size. If the lattice vector of a crystal is $\boldsymbol{a}$, then the relation between lattice vector $\boldsymbol{a}$ and reciprocal lattice vector G can be expressed as:

$$G=N\frac{2\pi}{\boldsymbol{a}} \qquad 2.1$$

Where N is an integer[30].

In translation symmetry structures like photonic crystal, the electromagnetic modes can be classified by the wave vector $\boldsymbol{k}$. However, different $\boldsymbol{k}$ may lead to the same mode. Specifically the mode of $\boldsymbol{k}$ is equal to the mode of $\boldsymbol{k} + \boldsymbol{G}$, where G is the reciprocal lattice vector (harmonic series) [31]**.**

By combinig Ampere' law and Faraday's law we can obtain an eigenvalue equation. Assuming we have a plane wave $\mathbf{H}(r)$ = **a** $\exp(ik \cdot r)$.

$$\nabla \times \frac{1}{\varepsilon(r)} \nabla \times \mathbf{H}(r) = \left(\frac{\omega}{c}\right)^2 \mathbf{H}(r) \qquad 2.2$$

where the eigenvalue is $\left(\frac{\omega}{c}\right)^2$. The eigenvectors $\mathbf{H}(r)$ are harmonic modes spatial patterns.

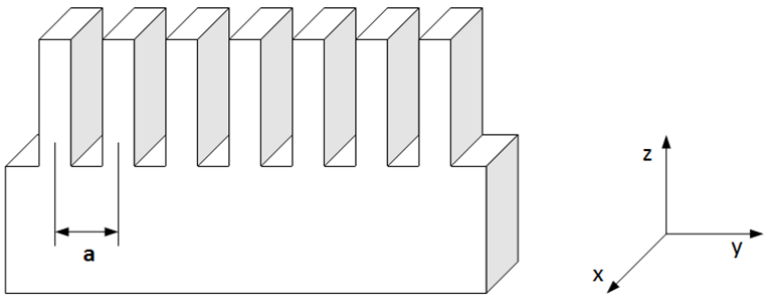

Figure 3. One dimension periodic structure

An example of periodic structure with discrete translational symmetry along $\hat{y}$ direction is illustrated in *Figure 3*. We can also have dielectric constant invariant in a fixed step from the equation $\varepsilon(r) = \varepsilon(r \pm a)$, then we can have $\varepsilon(r) = \varepsilon(r \pm ma)$, where m is the integer. For each integer distance, a translation operator **T** can be defined, in which way it shows the repetitive function by the dielectric changing. So we will have,

$$\mathbf{T}_y e^{ik_y y} = \left(e^{-ik_y ma}\right) e^{ik_y y} \qquad 2.3$$

Modes with wave vector $k_y$and k_y+m2π/a they all have the same **T** eigenvalue of $e^{-ik_y ma}$. If taking all the modes with the same **T** eigenvalue,

$$\mathbf{H}_{k_y}(r) = \sum_m c_{k_y,m}(z) e^{i(k_y + m2\pi/a)y} \qquad 2.4$$

$$= e^{ik_y y} \cdot \sum_m c_{k_y,m}(z) e^{im(\frac{2\pi}{a})y}$$

$$= e^{ik_y y} \cdot u_{k_y}(y, z)$$

where **H** is the magnetic mode, c is the expansion coefficients and $\boldsymbol{u}$ is the periodic function in y direction. The equation above shows that the interaction between the plane wave and periodic

structure results in a plane wave multiplied by a periodic function, in which case the plane wave becomes modulated by the periodic function. This conclusion is called Bloch's theorem[32].

We can also convert **H**(r) to **E**(r) by equations

$$\nabla \times \mathbf{E}(\mathrm{r}) - \mathrm{i}\omega\mu_0\mathbf{H}(\mathrm{r}) = 0) \qquad 2.5$$

Where μ_0 is the vacuum permeability.

2. Classification of Photonic crystals

From the dimension point of view, photonic crystal can be divided into one-dimensional PCs, two-dimensional PCs and three-dimensional PCs. The details of each type are introduced.

- **One-dimensional photonic crystals**

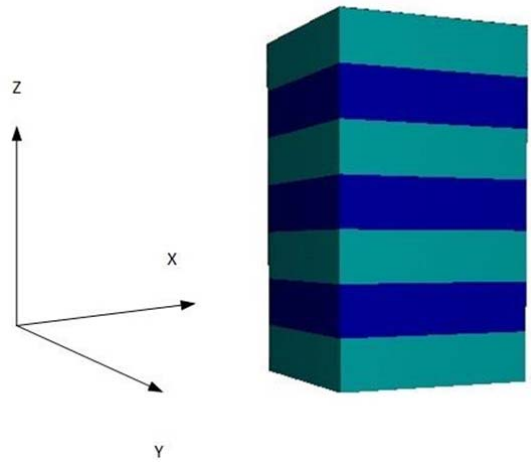

Figure 4. Schematic of one-dimensional PCs

A One-dimensional PC is the one of the simplest PCs. It consists of alternating material in one direction. An example of one-dimensional PCs is traditional multilayer films[33], which is illustrated in *Figure 4*. This photonic crystal can act as a perfect mirror in a sharp gap of frequency. By incorporating a defect layer, it can localize light modes[34]. This multilayer structure is widely used in dielectric mirrors and optical filters[35].

Since the periodicity is along only one direction and the structure is symmetrical with respect to the origin point. The first Brillouin zone is formed by the intervals between -2π/a and 2π/a, where a is the lattice constant. We can assume that the dielectric constant is altered with different layers. According to the translation symmetry (homogeneous in xy plane and periodic in z direction), we can classify the modes by applying $k_{\|}$ and k_z($k_{\|}$ is the wave vector is parallel to xy plane, and k_z is vertical to xy plane). $k_{\|}$ can be any value due to being homogeneous in xy plane, while k_z will

be confined in a finite interval. The wave vectors, which we use here, can describe the transforms of mode by the translation operator. According to the Bloch form introduced previously, the Bloch form of the modes can be written as:

$$\mathbf{H}_{k_\parallel,k_z}(r) = e^{ik_\parallel g} e^{ik_z z} u(z) \qquad 2.6$$

We can assume light incidents at a normal angle, which means the component of k vector $k_\parallel$ can be ignored. Now we can only consider the z direction. So the Bloch form of equation above can be rewritten as

$$\mathbf{H}_{k_\parallel,k_z}(r) = e^{ik_z z} u(z) \qquad 2.7$$

- **Two-dimensional photonic crystals**

Different from 1D PCs, the periodicity of 2D PCs exists in two dimensions, and the structure is homogeneous along the third dimension. Square lattice and hexagonal lattice are two of the simplest 2D photonic crystal structures.

In *Figure 5*, the periodicity exits in x and y directions and z direction is homogeneous. For simplicity, a square lattice is used as an example.

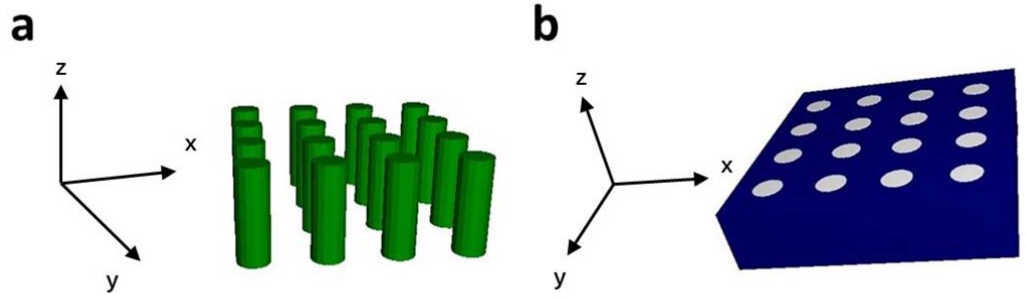

Figure 5. Schematic of two dimensional photonic crystal (a) lattice point is rod (b) lattice point is hole

In this case 2D PCs has discrete translation symmetry in the $\hat{x}\hat{y}$ plane, the periodic function is given as,

$$\varepsilon(r) = \varepsilon(r + i\hat{x}a + j\hat{y}a) \qquad 2.8$$

$$\varepsilon(r) = \varepsilon(r + R) \qquad 2.9$$

where i and j are integer, **R** is the linear combination of primitive vector in $\hat{x}$ and $\hat{y}$ directions. The Bloch mode of 2D PCs is described as,

$$H_{k_{\parallel},k_z}(r) = e^{ik_{\parallel}r}e^{ik_z z}u(r) \qquad 2.10$$

The noticeable difference between the 2D PCs and the 1D PCs is that the $k_{\parallel}$ will be confined in the Brillouin zone rather than k_z. Due to the mirror symmetry of the $\hat{x}\hat{y}$ plane, the modes can be classified by Transverse-electric (TE) mode, whose magnetic field component H is perpendicular to the $\hat{x}\hat{y}$ plane and Transverse-magnetic (TM) mode whose electric field component E is perpendicular to the $\hat{x}\hat{y}$ plane.

A more complicated photonic structure base on hexagonal lattice (hexagonal lattice) is shown *Figure 6*.

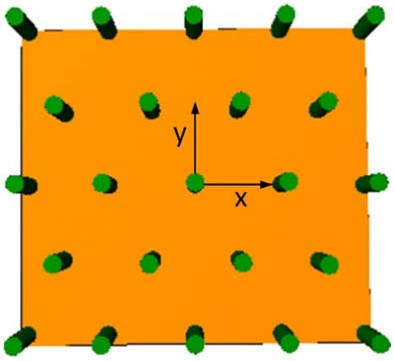

Figure 6. Schematic of hexagonal lattice photonic crystal

- **Three-dimensional photonic crystals**

In addition to the periodic $\hat{x}\hat{y}$ plane, if $\hat{z}$ direction is also periodic, it becomes 3D photonic crystal. There are several typical three-dimensional photonic crystals such as Yablonovite woodpile crystal, inverse opals and a stack of two-dimensional crystal[36-38][36][37][38]. An example of three dimensional photonic crystal is shown in Figure 7. This structure shows a wide band gap at from 10.6 µm to 12.9µm wavelength.

Manufacture of 3D PCs is challenging [39-41] [39][40][41]. In the case of the Yablonovite the dielectric bulk will be drilled along three certain lattice vectors to form a 3D FCC structure. In the case of the woodpile 3D structure, it can be fabricated layer by layer by patterning via lithography. By infiltration of opals with high dielectric index material in order to form the inverted structure and then removal of the spheres, 3D PCs can also be achieved[42].

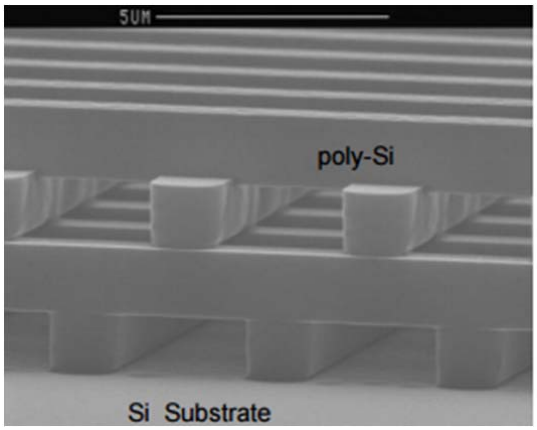

Figure 7. 3D photonic crystal fabricated on Si substrate extracted from [43]

3. Photonic quasicrystal

- **Definition of Photonic quasicrystal**

Before ten-fold rotational symmetry found in $\mathrm{Al}-\mathrm{Mn}$ alloy from Shechtman et al[44] , the rotational symmetries order was thought to be restricted to 2,3,4 and 6. The definition of crystal is redefined as 'any solid having an essentially discrete diffraction diagram' from International Union of Crystallography (IUC)[45]. Two categories are defined in crystals: periodic crystals and aperiodic crystals known as quasicrystals.

Conventional two dimensional photonic crystal lattice shapes such as square and hexagonal lattices have symmetries limited to four and six-fold, respectively.

However, higher order symmetry lattices can be achieved by using quasi-crystal designs. For example octagonal, dodecagonal and decagonal quasiperiodic photonic crystals display 8, 10 and 12-fold rotational symmetry, respectively [46] [47]. According to the class of quasi-crystal lattice, and the associated mathematical construction algorithm, an arbitrary level of symmetry can be achieved [48].

- **Constructing quasicrystals and 12-fold rotational symmetry quasicrystals**

Unlike the periodic square lattice and hexagonal lattice, a large number of cells are required to construct the quasicrystal structure in order to preserve the long term periodicity of the lattice. Substitution tiling is one of the common ways to generate quasicrystals. In the case of the Stampfli quasicrystal, the square-triangle cell with an inflation constant of $2+\sqrt{3}$ is scaled up followed by placing dodecagons on the parent square-triangle tiling. The total size of the parent cell is $\boldsymbol{a} \times 13.92$, where a is the distance between lattice point. The centres of the dodecagons

locate at the vertices and sides are perpendicular to the tile edges. Each of the dodecagons is composed of 6 squares and 12 triangles. The gap among three dodecagons will be tiled with a single triangle and gap among four dodecagons is filled with four triangles and a square[49]. The random-stampfli inflation of 12 fold structure is shown in *Figure 8*.

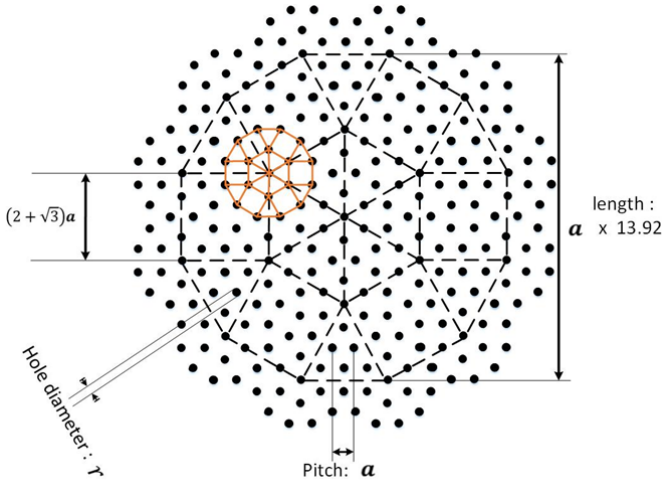

Figure 8. Random-stampfli inflation of 12 fold rotational symmetry, One of the offspring dodecagons is now shown as the orange solid lines.

Chapter 3: Review of progress in bio/chemical sensing applications

Bio-sensing as a detective technology for biological substance has been developed for decades[50-52][50][51][52]. It takes advantage of biological components such as enzymes, antibodies and gene probes to recognize a specific target. Typically, such sensors are used in monitoring bio-reaction events, converting the special signals (e.g. refractive index change by molecular hybridization process) to readable signals, which can be analysed easily. Sensors are used for screening interactions between ligand-receptors (such as biotin and streptavidin), DNA hybridization processes, detection of viral particles and also studies of cell morphology. Furthermore, biosensors are not only applied to biological fields, but also environment detection, medical treatment, public health and even food safety. They can be categorised by electrochemical [53][54][55]and optical [56][57][58] sensing mechanisms respectively. This chapter briefly reviews each technology, with particular focus on optical sensors.

3.1 Electrochemical biosensors

An electrochemical biosensor is a self-contained integrated sensor, in which the biological-recognition elements attach directly to the transduction element electrode or field effect transistor. Electrochemical biosensors can provide specific quantitative analytical detection. Electrochemical biosensors are divided into amperometric/voltammetric biosensor, impedance/conductance biosensors and piezoelectric sensors.

3.1.1 Amperometric biosensors

Amperometric sensors show outstanding performance with a relative low detection limit and high sensitivity. This type of sensor is normally used in the antigen and antibody binding event[59-61][59][60][61]. The current change will be the transduction signal, which is generated by an electro-chemical reaction under a certain voltage. Amperometric sensors use electroactive compounds to generate current[62]. The analyte will be bound with the working electrodes, the changed current is due to the oxidation or reduction of the electroactive species on the electrode[63]. Carolin Lau et al used heated electrodes for detecting glucose, it is based on glucose oxidase immobilized on the electrode. The amperometric signal is presented by the electrochemical oxidation of enzymatically resulted H_2O_2 releasing at the working electrode[64].

In addition to the electrodes, there is also a reference electrode existing, which is used for comparison. The working electrode uses a conductive material such as: Pt, Au, graphite, carbon or a conducting polymer[65-68][65][66][67][68].

3.1.2 Potentiometric sensor

Unlike the Amperometric sensor, the potentiometric sensor is based on the voltage response on an electrode. A selective outer layer and a bioactive material (enzyme) are used. This will give great selectivity for the target electrochemical species without the interference from other species. The response of such sensors is logarithmic. Normally a field effective transistor (FET) is used in the sensor design. An insulator gate is built between source and drain. An example of n-channel ion selective field-effect transistor is shown in Figure 9:

s

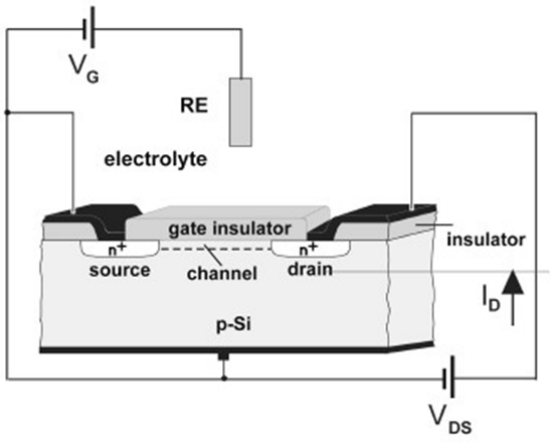

Figure 9. N-channel ion selective FET extracted from[48]

This field transistor sensor employs a p-type substrate and a n-type source and drain. The short channel is covered with a gate insulator, normally the insulator gate consists of one SiO_2 layer or double layer insulators (SiO_2-Si_3N_4, SiO_2-Al_2O_3, or SiO_2-Ta_2O_5)[69][70]. Those top layers are used as selective layer, which is selective towards other ions (K+,Ca_2+ et al). When a positive gate voltage V_G is applied, a N-type inversion layer forms underneath the gate oxide between the source and drain. The drain current is controlled by the effective electrical resistance of the inversion layer. Take an example of standard pH FET sensor, the materials like Si_3N_4, Al_2O_3 and Ta_2O_5 as insulator gate can sense the H^+ ion concentration and the charges build up at the surface, in that way the gate potential is changed[71]. Shul'ga et al represented an Ion-selective field-effect transistor, with a Si_3N_4/SiO_2 double layer covering the FET upper surface. The source voltage changes with

the pH-dependent changes in the threshold voltage, this representing the output signal[72]. As an ion-selective sensor, drain source current can be the output signal with constant V_{ds} and V_G [73].

3.1.3 Conductance/Impedance biosensor

When the binding between antibodies and antigens (Ag-Ab) happens, the electric field will be altered and the overall electrical conductivity of an electrochemical interface will be changed. It depends on whether a redox related charge transfer on the electrode interface occurs during the measurement time. Electrochemical impedance spectroscopy (EIS) is used for probing bioaffinity interaction at the surface of electrically conducting polymer or other electrodes[74], the first published EIS dates back to the 1970s[75]. The EIS can be further classified by whether there will be a redox related charge transfer across the electrode interfaces, they are named as Faradaic EIS and non-Faradaic EIS respectively. The difference between Faradaic EIS and non-Faradaic EIS is whether it relies on a redox process[76].

Tully's group used electropolymerization of a planar screen-printed carbon electrode with polyaniline to fabricate a conductive substrate. Polyclonal $anti-lnlB$ antibody was immobilized at the conductive polymer layer. The sensor measures the interaction with $lnlB$ antigens. A small voltage change is introduced by the binding event at the interface of an electrically conducting polymer[77].

3.1.4 MEMS cantilevers sensor

MEMS cantilevers sensor are also widely applied in biological detection. It is able to transduce bio/chemical reaction into mechanical response. A selective chemical layer is required and coated on the MEMs cantilever in order to interact with specific biomolecules (covalent binding of receptor). As a consequence, mass of cantilever increases and the natural frequencies are altered[78]. Normally the cantilever beams are excited by a sine wave voltage. The peaks frequency, which provides the maximum amplitude vibration, is called resonance frequency. The peak frequency changes when the mass on cantilever being changed. Femandez developed a porous silicon/polysilicon cantilever sensor for triglycerides sensing. It shows the ability to detect the triglycerides in human blood below the concentration range of 150-250 mg/L[79]. Chen was using micro-cantilever MEMS sensor to detect C-reactive Protein in a concentration range of 0.5 µg/ml – 500 µg/ml[80].

3.1.5 Piezoelectric sensor

With the help of external alternating electrical field, some materials like quartz crystals can resonate. The oscillation frequency is a function of quartz mass. Therefore the mass change on the quartz crystal surface will result a frequency shift. If the interaction between the antigen and antibody happens on the surface of the quartz, it will lead to a mass change and result in the oscillation frequency shift [81]. Tong et al used a piezoelectric quartz crystal sensor to monitor osteosarcoma cell adhesion, spreading, proliferation and apoptosis with quantitative analyses in real time[82].

3.1.6 Summary of electrochemical biosensors

Up to date many electroanalytical methods have been proved that they can offer outstanding sensitivity and low detection limit $(sub\ ng/mL)$. However, the main problem is that the measurement is hard to transfer from the clean solutions of the research environment to a practical clinic environment. Also another problem of those sensors is that it is not easy to perform multiplexing sensing. Normally, reliable diagnosis needs to utilize assays with multiple biomarkers, therefore this requirement for multiplexed biosensors is urgent for diagnostic purposes.

Table 1. The pros and cons of the different types of electrochemical biosensors.

Types	Advantages	Disadvantages
Amperometric biosensors	Small size, robust, economical, repeatable outside laboratory	Indirect sensing system, poor sensitivity for oxygen/hydrogen peroxide detection
Potentiometric sensor	Simple operation, Small size, Easy to fabricate	Relative lower sensitivity Nonspecific effect of binding (interference from other ions in the sample), Low signal to noise ratio

Piezoelectric sensor	High sensitivity, simplicity of use, low cost, real-time	Result varies between a targe with low ionic strength to an target with high ionic strength, Established technology
Impedance sensor	Easy to miniaturize, rapid response, low detection limits, cost-effectiveness, real-time monitoring	Easy to generate false result and affects the detection limit

3.2 Optical biosensors

Optical sensors have become the most popular sensors for bio-analysis in recent years[83][84][85]. There are more advantages of using optical methods than other mechanisms. First of all visible radiation/IR radiation can be applied in optical transducer technology[86][87]. Secondly it can provide a non-destructive operation with molecules. Thirdly, a rapid signal response and readout system can be realized. Furthermore, they are also electrically noise free.

Different mechanisms can be used in optical sensors: Reflectometric interference spectroscopy (RIFS) [88-90][88][89][90], Interferometry[91-93][91][92][93], optical waveguide light mode spectroscopy[94][95][96], fiber mode spectroscopy[97][98] and surface plasmonic resonance[99]. An overview of mainstream label free optic sensing technologies are introduced in this section.

3.2.1 Reflectometric interference spectroscopy (RIFS)

RIFS is a direct bio-sensing reflectometric technique. A white incident light will be reflected partially when it pass through the interface with different refractive indices. Those reflected light will superimpose with each other and result in a special interference spectrum. For instance binding events between antibody and antigen results in a change of thickness and the refractive index, this change will cause a frequency shift in reflectance [100] . A schematic of RIFS is shown in Figure 10.

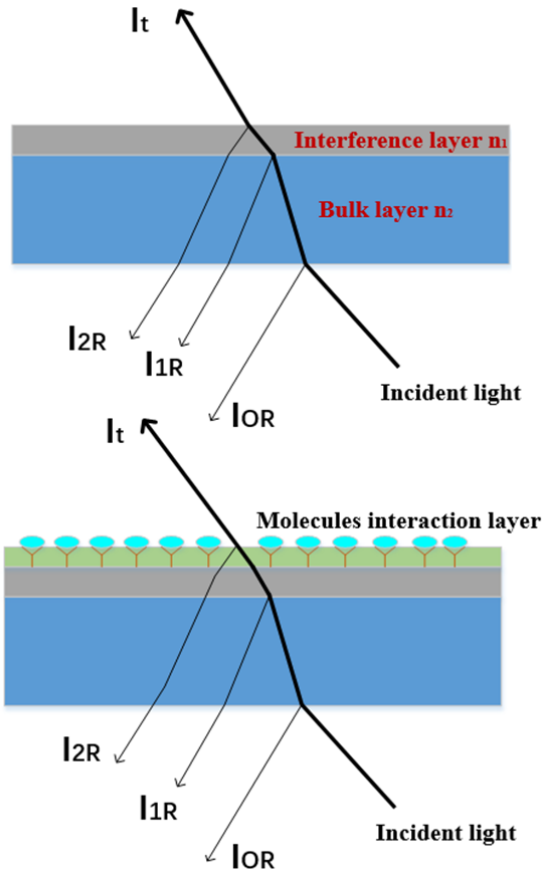

Figure 10. Schematic of RIFS senor, I_{or} is the reflection from the first interface (from bottom to top) . I_{IR} is the reflection from the second interface. And I_{2R} is from the layer where the binding event happens

3.2.2 Interferometry

The evanescent field of modes propagating in a waveguide will be affected when bio-reaction occurs on the surface of the waveguide. Taking an example of Mach-Zehnder interferometry (MZI), an optic waveguide splits into two waveguide arms with different length, and they will be connected in the end. The antigen and antibody interaction occurs on the surface of one arm called the sensing arm, where there will be a refractive index change. During the light travelling in the sensing arm, there will be a phase shift. It results in total phase change in the output port which affects the transmission.

Yu's group used two trimethylene terephthalate fibers to fabricate an ultra-compact MZI-based sensor with very high sensitivity up to 1100nm/RIU and detection limit is down to 1.8×10^{-6} RIU [101]. Phase change was induced by changing surroundings, which reflects on the transmission signal from the output of the two fibers. Figure *11* shows an SEM image of the MZI sensor.

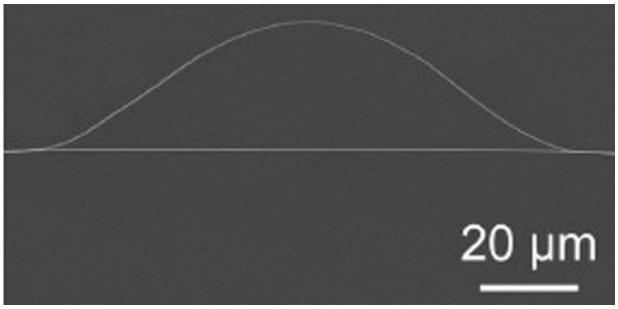

Figure 11. SEM image of MZI biosensor[75]. One arm is longer than the other, this distance difference leads to phase changes at the end of MZI.

3.2.3 Surface plasmonic resonance biosensor

Charge density will be oscillated at the interface between a metal and one dielectric (low refractive index layer) and is called a surface plasmonic resonance (SPR)[102]. Plasma is defined as free electrons of a metal layer being excited. This excitation is provided by energy transferring from light. The amplitude of the plasmon electromagnetic/evanescent wave will be maximum at the interface of the metal and ambient (analyte). The evanescent field will penetrate into the aqueous target with by approximately one wavelength's depth. Normally the p-polarized TM component of an electromagnetic wave is applied for coupling plasmon oscillation. The resonance can also be achieved by changing the wavelength or frequency with a special angle or by changing the angle at a fixed wavelength. The incident light will be partially adsorbed and the reflected light is faced with attenuation when the resonant condition is satisfied. A refractive index change is introduced by a biomolecule attaching on the metal surface, this results in altering the resonance state. For example the angular position, which leads to the minimum reflectance, will change[103].

SPR sensors can be divided into prism coupling configuration, waveguide coupling configuration, optical fiber coupling configuration, side-polished fiber coupling configuration and grating coupling configuration, the plasmonic mechanisms of these configurations will be introduced in the following section.

3.2.3.1 Prism coupling configuration SPR biosensor

A simple prism coupling configuration is shown in Figure *12*. The incident light will be totally reflected at the interface between the prism and metal. The photons will be coupled into surface plasmon waves when the propagation constant of the evanescent field matches that of surface plasmon wave at the resonate wavelength[104]. Prism coupling sensors have the merit of excellent sensitivity and low detection limits[105][106], however it is impossible to be integrated with other optic components because the prism has a large volume.

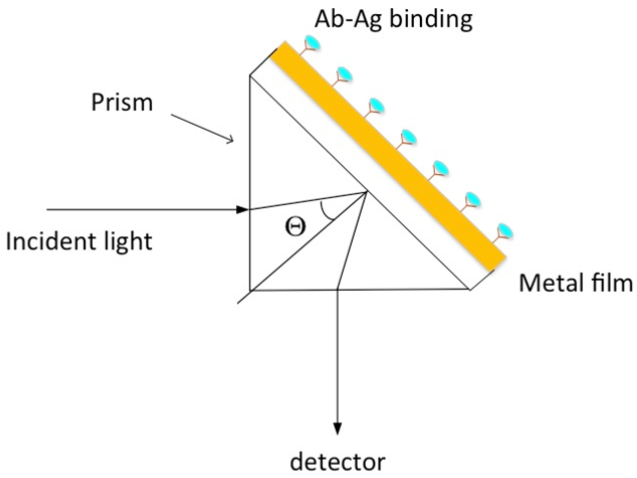

Figure 12. Schematic of prism coupling SPR sensor

3.2.3.2 Waveguide coupling SPR configuration

Light can propagate in the waveguide by the internal reflection and also an evanescent field will be generated at the interface between metal and waveguide, where the surface plasmon wave (SPW) can be excited. Surface plasmon wave (SPW) are electromagnetic excitations propagating at the interface between a conductor and a dielectric. An example of an integrated optical waveguide SPR sensor is shown in Figure 13. A planar multilayer structure to support surface plasmon. If the phase of the surface plasmon matches the waveguide mode, the surface plasmon will be excited. The surface plasmon strongly depends on the wavelength and only a narrow spectral band will be supported. This leads to a narrow dip on the transmitted spectrum, it is related to the energy transfer from waveguide mode to surface plasmons. A tantalum pentoxide layer was used to tune the operation point towards aqueous conditions. A chromium layer is used

for the adhesion promoting purpose. By using this SPR sensor configuration, a bulk sensitivity of 2000nm/RIU was achieved[107].

Waveguide coupling configuration is more easily integrated with optical and electrical components comparing with prism coupling configurations[108][109].

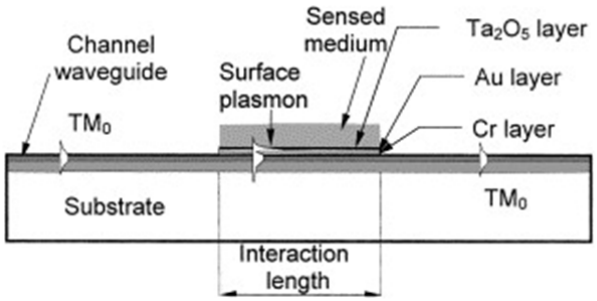

Figure 13. Waveguide-coupled SPR sensor extracted from [107]

3.2.3.3 Fiber coupling configuration

In fiber coupling configurations, a small part (cladding) of a fiber will be removed and a layer of metal (gold for example) will cover the gap. In the similar way, SPR will be excited. When the target is attached onto the sensing area, the intensity of the detected signal will be different. The propagation constant of the exited SPW is dominated by the refractive index of the atmosphere near the metal film and the interaction between the SPW and fiber mode. Changes in the refractive index of the sample will result changes in the transmitted optical power or spectra. Because the SPW can be excited under the conditional of only the light with magnetic field parallel to the metal film, the fiber optic coupling plasmonic sensor is highly polarization dependent[110]. An example of a fibre SPR sensor (silver coated optical fibre probe) and measurement setup are shown in Figure 14. It achieved a sensitivity of 1.483nm/(mg/ml).

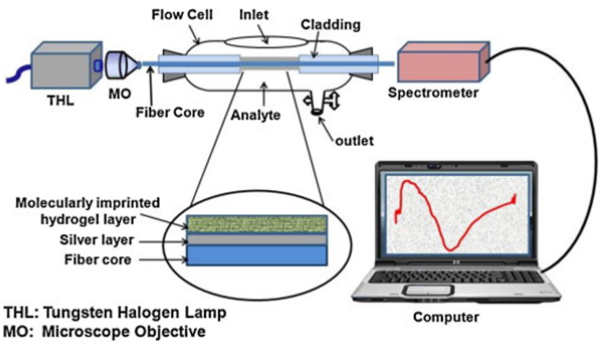

Figure 14. Schematic of fibre SPR sensor and measurement setup extracted from [21]

3.2.3.4 Grating coupling configuration

Grating coupling can also excite the SPS. When the momentum of diffracted light, which is parallel to the metal grating surface, the diffracted light can be coupled with the SPW. In the metal grating coupler structure shown in Figure 15, the incident light coming to the grating, the wave will be split into a reflect wave and a diffract wave. Under the condition of the propagation constant matching between the optical wave and SPW, a coupling phenomenon occurs. This coupling will lead to a decreased intensity of the reflected wave, therefore a narrow absorption dip occurs in the spectrum of reflection[111].

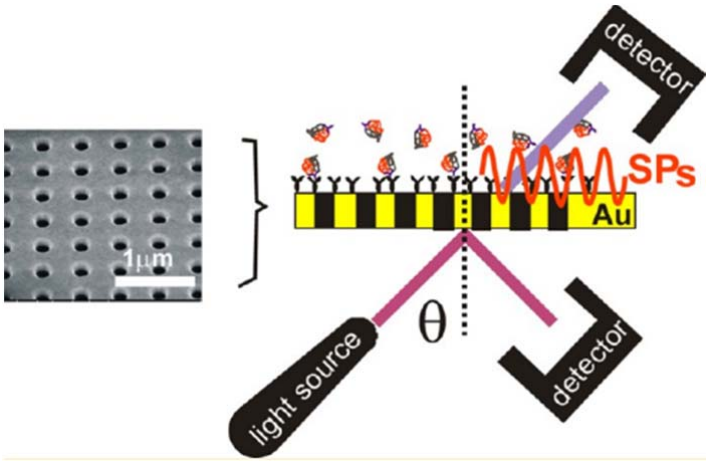

Figure 15. Grating coupler with periodic plasmonic structure for chemical sensing [112].

3.2.4 Optical waveguide light mode spectroscopy

Optical waveguide uses the advantage of an evanescent field for detecting surface condition change. Linearly polarized laser light can be coupled into a thin waveguide layer with a certain angle by a grating coupler. The coupling is a resonance event, which happens at a special incidence angle. It depends on the refractive index of the target on the waveguide surface. Light will be confined in the waveguide by total internal reflection and the signal will be collected by a detector (spectrometer) in the terminal. A schematic of waveguide coupling configuration is described in Figure 16. light is coupled into the waveguide via grating, the output intensity is measured as a function of incident angle. In the experiment of detecting bio-event, the photodiode as a detector will sense the intensity of the coupled light after the monochromatic light being coupled into the waveguide by the grating. In presence of biomolecules the effective index in the grating area is changed. Surface of waveguide the coupling angle is altered (coupling

condition). Michelle developed an optical waveguide light mode spectroscopy sensor to monitor the adsorption kinetics of 0.1 mg human serum albumin (BSA) solution[113].

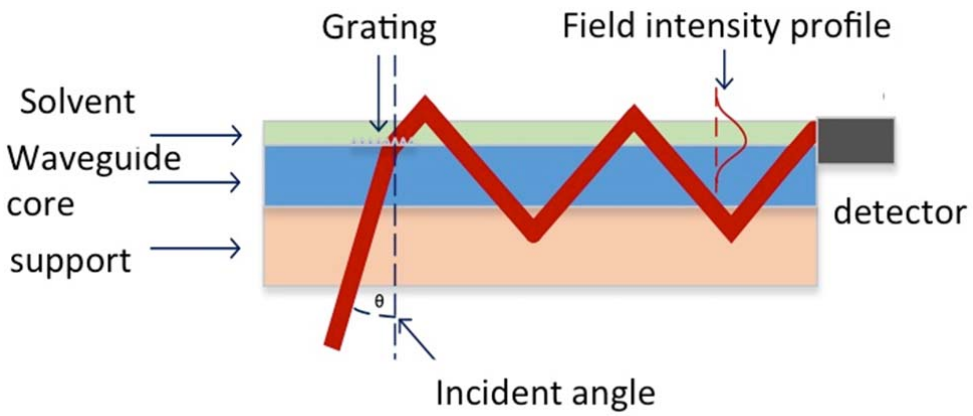

Figure 16. Schematic of an optical waveguide light mode spectroscopy.

3.2.5 Summary

To date optical sensors have been developed intensively for label free detection and the performance is comparable to traditional electrochemical biosensors in different fields including bulk solution, protein, DNA, bacteria and virus. Some optical sensors like SPR and waveguides sensors are already commercialized. Table 2 compares the optical sensing platforms discussed in this chapter. It is difficult to make a direct comparison due to different analyte and detection configuration.

The limitation of such sensors are obvious. Firstly almost every type of SPR sensor requires a metal layer in order to support surface plasmons, the fabrication step is relative complex and critical. Secondly, prism type and fibre types are hardly integrated with other optical function components (e.g grating, waveguides). Thirdly, multi-parameter sensing is hard to achieve.

On the contrary PC sensing systems are much easy to integrate with other optic components (e.g slab waveguide), PC coupler and PCs sensors can be integrated on one slab waveguide with monolithic fabrication. Metal layers are not required which simplifies the fabrication process.

Table 2. Performance of different optical biosensors.

SENSING PLATFORM	OPTICAL TYPE	TARGET	DETECTION LIMIT
Surface plasmon resonance	Surface plasmon resonance	Bulk solution	$10^{-5} - 10^{-8}$ RIU[114]
	Angle modulated SPR	Protein	0.15 $ngmL^{-1}$[115]
	Wavelength modulated SPR	DNA	10pM[56]
	Prism-based SPR	Bacteria	10^{6} $cfu\ mL^{-1}$[116]
	biacore™ system(GE healthcare)	Antibodyscreening/ Immunogenicity testing	1ng mL^{-1} [117]
Interferometer	Mach-Zehnder	Bulk solution	10^{-7} RIU [118]
	Young's interferometer	Virus	1000 particles mL^{-1} [119]
	Porous silicon	DNA	2pM[120]
	Bio-Layer Interferometry	Protein	sub-ngmL^{-1} [121]
Waveguide	Resonant mirror	Cell	10^{6} cells mL^{-1}[122]
	Metal-clad waveguide	Cell	10 cells mm^{-2}[123]
	Reverse symmetry waveguide	Cell	60 cells mm^{-2}[124]
Optical fiber	Fiber bragg grating Fiber coupler	Bulk solution Protein	10^{-6} RIU[125] 0.5 μgmL^{-1}[126]

Chapter 4: Development of combined photonic crystal waveguide coupler / channel splitter.

In this Chapter the Photonic crystal coupler / splitter device design is introduced and the design developed from first principles. Background literature relating to waveguide couplers is reviewed, and shortcomings of current grating couplers identified. Constraints on slab waveguide design are explained along with choice of materials and fabrication methods. Background physics relating to coupler design is explained in detail. Modelling methods (RCWA) are then developed based on established physical principles such as Ewald circle construction. Key parameters such as polarizations, propagation directions, hole diameter and waveguide core thickness are explored with RCWA modelling. Design choices and fabrication methods for the coupler are explained in detail. Finally, experimental measurements on fabricated devices working for 630nm/785nm light are presented exploring the full spectral and angular coupling properties for a number of different photonic crystal lattices.

4.1 Brief review of conventional waveguide coupling and splitter methods

Couplers and power splitters are key components for integrated optics and have been studied extensively for decades. Grating couplers are usually used to couple light into optical waveguides in order to overcome the mode mismatch issue between the waveguide mode and fiber mode. They also allow wafer scale test for devices on SOI substrates. There are many grating coupler designs with potential for high efficiency and good alignment tolerance for fiber-to-chip coupling. Once coupled, light is guided to the input of a beam splitter using etched waveguides thereby providing splitting of optical signals. Common splitter implementations include multimode interference filters (MMI)[127] or Y-junction splitters[128][129]. Using a Y-junction splitter approach, the overall size of the combined system becomes very large (of the order of mm) for large channel counts (>8) [130]. MMI splitters have the advantages of near equal power output over the output channels, and small overall footprint size. However, the optical power throughput of MMI splitters is low due to the requirement for single mode input / output waveguides. These two approaches also require rib or ridge waveguide structures to be etched, incurring loss due to waveguide side wall roughness. The need for waveguide tapers (or integrated reflector) usually limits the input light source to a single mode fiber positioned close to the surface with a few microns squared spot area. Silicon photonics applications generally only need single mode input coupling due to the nature of the applications. Many applications such as bio-sensing do not require fibre coupling, and can benefit from larger area free space coupling from light sources

such as LEDs and Laser devices. They can benefit from higher power input coupling from highly multimode light sources. Hence our device targets different applications areas than conventional grating coupler devices.

Photonic crystal based power splitters have recently been demonstrated for 'in-plane' waveguide configurations, but the number of power-split channels was limited to two, and they were also polarization dependant. They also did not provide dual functionality. To date, there have been few attempts to perform free space light coupling and power splitting function in one single device in order to decrease the size, and cost, of the full chip.

Most of these approaches were also based on high index contrast waveguides such as SOI working at a IR wavelength[131]. Silicon is particularly common due to its importance in integrated optics and compatibility with CMOS devices. However, low refractive index materials are also highly useful for biological and chemical optical sensing fields.

4.2 Photonic crystal coupler splitter concept

Coupler / splitters based on two-dimensional photonic crystal (PCs) and photonic quasicrystal (PQCs) lattices benefit from very small overall footprint (microns rather than mm for the combined system). The lattice points are formed by etched holes into the core layer of a slab waveguide. The operating wavelength of 633nm/785nm was chosen for compatibility with sensing applications[132][133], and availability of cheap semiconductor lasers. Couplers based on periodic and quasi-periodic 2-dimensional photonic crystals lattices provide several key advantages. Firstly, coupling over a large azimuthal angular range with a particular incident angle (especially normal incidence) is possible. Secondly the lattice can be tailored such that there is improved mode match to the circularly symmetric Gaussian shape of the incident laser beam. The third and the most important factor is that they can simultaneously act as both couplers and beam splitters for the incident beam. Fourthly they provide very high optical power throughput since the in-plane split beams are laterally multi-mode, as would be the case for a very wide rib / ridge waveguide. We utilize this feature to yield multiple in-plane propagating modes in a slab waveguide. The split beams are perfectly confined and 'collimated' (a square lattice provide 4 propagation modes, hexagonal lattices provide 6 propagation modes and quasi crystal lattices provides 12 propagation modes), which eradicates loss incurred by rib / ridge waveguide fabrication process. Furthermore, a functional waveguide taper component is not needed in this work, and the coupling area can be scaled in size to match the input source size.

The concept of a PCs coupler (square/hexagonal lattice) used for coupling and beam splitting is shown in Figure 17.

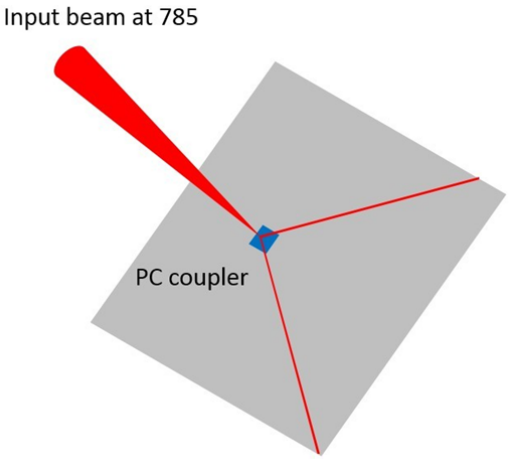

Figure 17. PCs coupler couples and splits monochromatic light at 785 nm simultaneously

Square and hexagonal lattices are chosen because of their stronger diffractive effect, sharp resonance and high coupling efficiency, which is due to the stronger Fourier peaks in the spectrum. Furthermore a 12-fold PQCs is introduced in order to achieve more in-plane multiple modes, which provide more data channels (up to 12).

The coupling and mode splitting principle is based on Bragg diffraction. When light hits the photonic crystals, the incident light will be diffracted into several coupled modes, the maximum number of coupled modes depends on the rotational symmetry of the photonic crystal lattice, as defined by the number of primary Bragg spots in its diffraction pattern. At near normal incidence, splitting is symmetric with equal included in-plane angle. Lower order diffracted light, which matches the waveguide modes, is then confined in the slab waveguide.

Before moving onto coupler design it is important to first define some conventions which will be used for component design throughout this thesis and review some physical concepts relating to photonic crystals and diffractive structures. The definitions of light polarization and photonic crystal lattice type are complex but important. Hence they are described in this section, and will be referred to throughout this thesis. For a basic introduction to photonic crystals please refer to Appendix A.

4.3 Background physics relating to coupler design

4.3.1 Incident light Polarization

Figure 18 shows the polarization of incident light in the plane of the lattice and in free space. The blue arrows indicate the orientation of electric field vector for electromagnetic fields. In the case

of free space propagation the S polarization is identified as the $\boldsymbol{E}$-field being perpendicular to the incident plane and $\boldsymbol{H}$-field being parallel to the incident plane, while **P** polarization corresponds to $\boldsymbol{E}$-field being parallel to the incident plane and H-field being perpendicular to the incident plane. For free guided modes, TE polarization corresponds to the E-field vector being parallel to the waveguide plane and $\boldsymbol{TM}$ polarization corresponds to the E-field perpendicular to the waveguide plane. In general, S polarization light will excite $\boldsymbol{TE}$ modes in the waveguide, while P polarization light will excite $\boldsymbol{TM}$ modes.

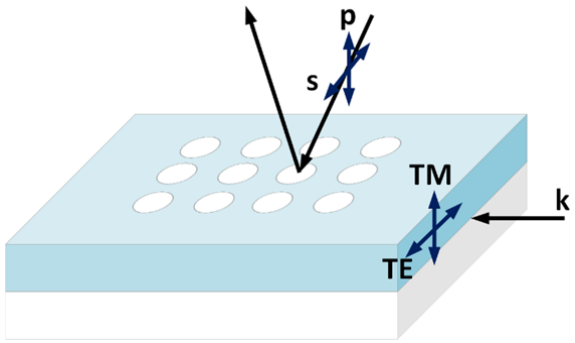

Figure 18. Polarization convention of TE and TM modes. Blue arrows indicate the E-field vector orientation of different polarizations and black arrow means propagation direction.

4.3.2 Photonic crystal lattice types and reciprocal lattice

As explained in Appendix A, photonic crystals can be categorised into 2 lattice families: periodic and Quasi-periodic. The concept of quasi-periodicity in PCs has been instigated and developed at Southampton since 1996. In this thesis both types of lattices are utilised for different components. For the coupler the quasi-crystal has some advantages, but for simplicity I start with periodic lattices.

A reciprocal space representation of a photonic crystal lattice has many advantages. This is basically a Fourier transform of the real space lattice leading to a 'frequency' (or k space) domain representation of the lattice. This reveals more information regarding true periodicity.

4.3.3 Diffraction in periodic structures

Diffraction happens when light is incident on a periodic structure. Figure 19 shows how several diffraction orders can be generated in both reflection and transmission for a transparent (non-metallic) grating structure, as is the case for a photonic crystal lattice.

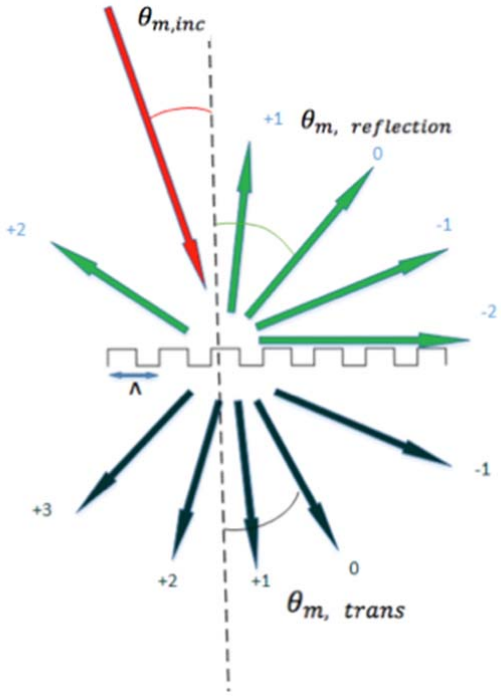

Figure 19. Schematics of diffraction happens on grating structure

Angles are governed by the grating equation[134]:

$$n_{ref} sin\theta_m = n_{inc} sin\theta_{inc} - m\frac{\lambda_0}{\Lambda} \quad 4.1$$

where n_{ref} is the refractive index of the media of the reflection area. The first order diffraction (corresponding to primary Bragg peak) provides the strongest coupling efficiency and so is best used for device applications. Therefore we can set θ_m to 0, and m equal to 1 to ensure most of the power is distributed in the first order diffraction. The diffraction in transmission area is the same as reflection but the refractive index of the media is different.

4.4 Outline of input coupler design methodology

Designing photonic crystal couplers requires two major steps. Firstly, the diffraction pattern of the lattice is investigated to determine the location of the primary Bragg peaks. The diffraction pattern is essentially the reciprocal space (frequency domain) representation of the lattice.

Secondly, in order to achieve phase matching between the lattice and an incident Laser beam, lattice parameters and size of lattice point (here holes) must be chosen such that the 'in-plane' component of the wave-vector corresponding to the photonic crystal Bloch mode, matches the location of the primary Bragg peaks. The photonic crystal Bloch mode wave-vectors depend strongly on the slab waveguide material and thickness, and the photonic crystal fill factor. This can be rigorously calculated from the band diagram, which provides information about the effective index of the Bloch waveguide mode, but this is very complex as an extended plane wave method must be used. A more simplistic average index approach gives a very good 1st approximation and is used for initial design. The exact coupling angle for a given design can then be determined by generating the angle resolved dispersion map, which can be calculated by RCWA method. This is analogous to the band diagram.

4.4.1 Introduction of rigorous coupled wave analysis

RCWA is about the electromagnetic fields, which summarize all the coupled waves. And the coupled waves are related to different Fourier harmonics, in that way the Maxwell's equation can be solved in the Fourier domain.

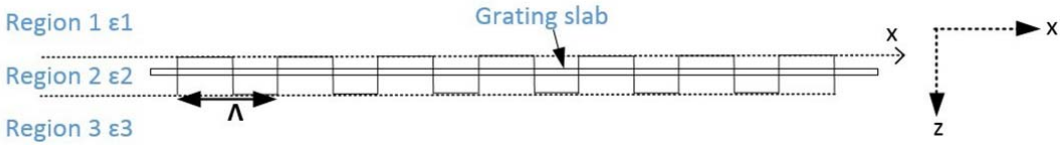

Figure 20. Grating structure for RCWA explanation

The space is divided into three regions: the region 1, region 3 and the grating region 2. The input region and bulk region are homogeneous dielectric with relative permittivity (dielectric constant) ε_1 and ε_3. Grating region has the relative permittivity ε_2. The grating in region two can be divided to many planar grating slabs, which are perpendicular to the z axis. The rigorous coupled wave analysis is applied in such slabs grating. The electric and magnetic field can be expended in terms of space harmonics, this is corresponded to the diffraction order outside the grating. If the planar grating layer is thin enough, any grating structure can be built and analysed [135].

4.4.2 Slab waveguide mode characteristics

Before taking PCs into account, the initial optical property of the slab waveguide consisting of the substrate, buffer layer and core layer need to be acknowledged. An asymmetric 4 layer slab waveguide is constructed from air/SiON/SiO_2/Si shown in Figure 21. SiON acts as the core layer and its thickness an

d RI are adjusted to support single mode guiding at the operating wavelength. SiO_2 (n=1.46) is provides a buffer layer between the Si substrate and SiON core layer. Our SION material deposition process was tuned to give a refractive index of 1.7 at 780 nm.

Figure 21. Cross section of the SiON/SiO_2/Si slab waveguide structure.

Figure 22 shows the effective index for TE/TM modes supported by the un-patterned SiON/SiO_2/Si slab waveguide and is calculated by FDTD method. It shows that single mode transmission is only supported when with the thickness of the SiON core layer is below 600 nm at wavelength of 785nm. The fundamental TE mode effective index value is about 1.58 and TM mode of 1.55 according to the calculation.

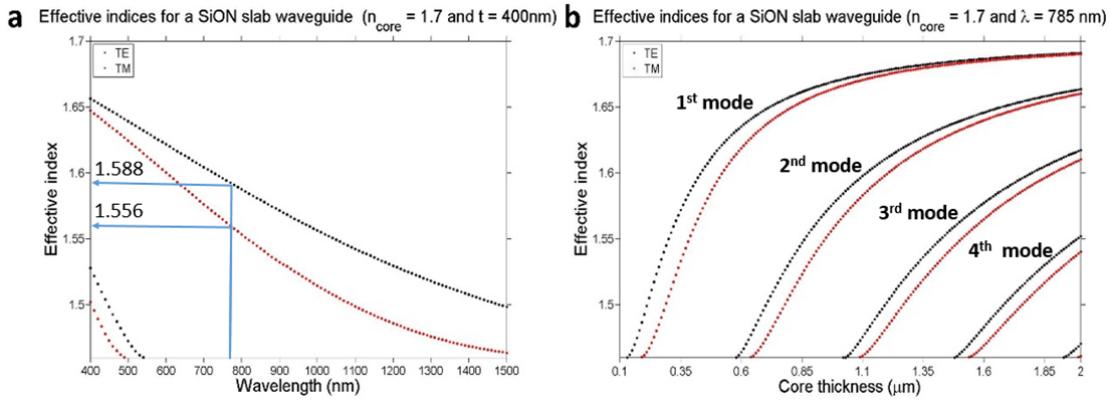

Figure 22. Effective index for TE/TM modes in SiON/SiO2/Si slab waveguide. a) Changing the wavelength with 400nm thick SiON layer, b) changing thickness of core layer with 785nm wavelength

4.4.3 Ewald circle construction and coupling demonstration for 633nm

The coupling angle can then be predicted by generating the angle resolved dispersion map, calculated by A RCWA method, using the effective mode index for the high dielectric material. As an example of a square lattice (a:450nm d:140nm) PCs and a hexagonal lattice (a:450nm, d:200nm), the angle-resolved zero-order reflection is shown in Figure 23. Sharp features (dotted lines) correspond to guided mode coupling conditions. In this case coupling angles θ_{in} for 633nm is approximately 41° and 7 ° for square and hexagonal lattice, respectively .

Since the PC slab has 2-dimensional periodic patterning across its surface, coupling conditions can be visualized by examining the reciprocal lattice. The directions of the coupled beams of the incidence light can be determined via the Ewald sphere construction.

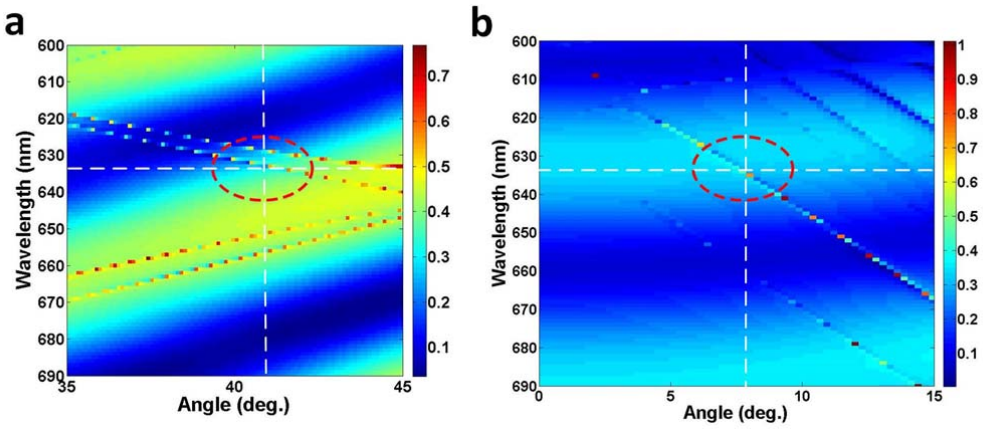

Figure 23. RCWA calculated angle-resolved zero-order reflectance a) a square lattice PC (a=450nm, d=140nm) b) a hexagonal lattice PCs (a=450nm, d=180nm)

Figure 24 shows the Ewald circle construction for square and hexagonal lattices to determine the diffraction direction and coupling conditions at 633nm. The real space lattice pitch and hole diameter are defined as $\boldsymbol{a}$ and $\boldsymbol{d}$. The reciprocal space lattice period is defined as **G**. For a square lattice (a:450nm d:140nm) the **G** is expressed as $\frac{2\pi}{\boldsymbol{a}}$ = 13.963 μm^{-1}. The magnitude of wave vector k_0 of incident light at 633nm is expressed as $\frac{2\pi}{\lambda}$ = 9.926 μm^{-1}. At the incident angle of 40.5 °, the in-plane k vector is given by: $k_x = k_0 \cdot sin\theta$=6.446$\mu m^{-1}$. This is indicated by the cross section graph inset to the *Figure 24*. A vector with magnitude of k_x is drawn terminating at a reciprocal lattice point along $\Gamma - X$ direction. The red circle, which is centered at the starter of k_x, has a radius of $n \cdot k_0$ = 15.3 μm^{-1} (n is mode effectvie refractive index of PCs material). It indicates the maximum modal propagation constant in the PCs slab waveguide.

The intersection between the circle and any lattice point leads to an 'in-plane' guide mode. The arrows indicate the direction of these modes.

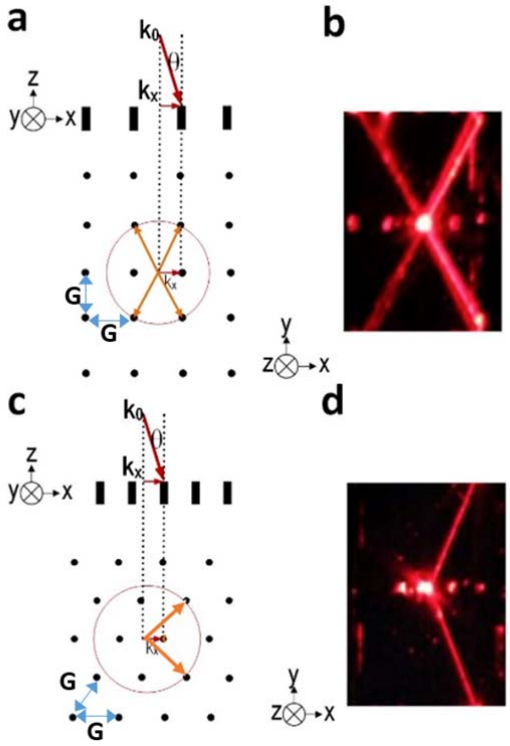

Figure 24. Ewald circle construction and related experiment result at 633nm for a square lattice (a: 450nm, d: 140nm) and a hexagonal lattice (a:450nm, d:180nm)

A coupler with a hexagonal lattice structure (a:450nm, d:180 nm) was analysed with the Ewald sphere methodology. The reciprocal lattice is 30 ° rotated compared with respect to the real space lattice. The reciprocal lattice period G=$\boldsymbol{4\pi/a\sqrt{3}}$=16.123 μm^{-1}. In-coupling angle is approximately 7.1 ° according to the RCWA calculation. Therefore the in-plane wave vector $k_{\mathrm{x}} = k_0 \cdot sin\theta$=2.08$\mu m^{-1}$ (oriented along $\Gamma - \mathrm{X}$ direction of reciprocal lattice). Three lattice points are located within the red circle and two of them interact with Ewald circle (red circle), this indicates that two coupled modes propagate backwards with an angle separation of 134 °. The directions are shown as orange arrows.

By using the coupling angle (AOI) and effective mode indices (n_{eff}) to construct the Ewald sphere, the coupling directions can be predicted. Strong coupling can be achieved by tuning in-coupling angle and effective index in order to intersect lattice points with the red circle. This can be achieved by changing the diameter of the holes and lattice constant, which in turn changes the effective mode index. For lower order bands, n_{eff} can be estimated by the fill factor weighted average of the slab mode effective index due to the E-field distributed in the high index material.

Using this design methodology, successful coupling at a specific angle of incidence (AOI) and simultaneous light splitting was experimentally demonstrated for both square and hexagonal lattice couplers at 633nm.

4.4.4 Ewald circle construction and coupling demonstration for 785 nm

It is possible to scale the lattice period and holes size to shift the operating wavelength to another wavelength due to the linear scaling law of PCs. Here we shift the working wavelength from 633 nm to 785nm, which gives a scaling factor of 785nm/633nm= 1.24. Therefore a lattice period of 558 nm and hole diameter of 174nm are required. While in a real device the thickness of the core layer is not altered, this will affect the coupling angle but only by a small amount.

Square lattice coupler with a period of 550nm and diameter of 170nm was calculated by RCWA method (s-polarization and along $\Gamma - X$ direction), which indicates the coupling angle is 41°. Comparing with the result from the square lattice coupler (450nm period and 140nm hole diameter) at 633nm, the coupling angle is close.

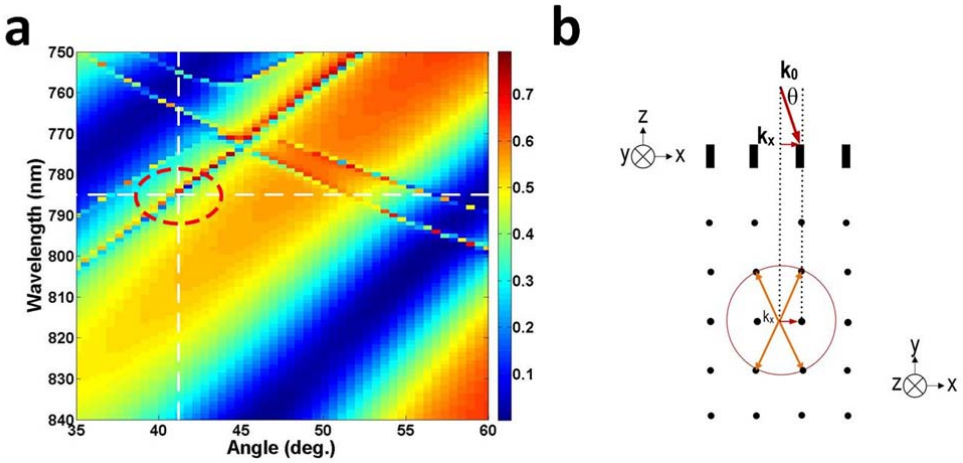

Figure 25. Square lattice coupler with period of 550nm and hole diameter of 170 nm a) RCWA calculation b) Ewald circle construction

Figure *25* (b) shows the Ewald circle construction for this coupler. The in-plane component of the wave vector ($k_{//} = k_0 \cdot sin\theta_{in}$=5.25$\mu m^{-1}$) is oriented along $\Gamma - X$. This time fill factor and effective index of slab waveguide mode are used to estimate PCs mode effective index. The TE and TM mode index of the slab waveguide are 1.5881 and 1.5560 respectively, calculated by FDTD for a 400 nm SiON thin film. Because of the PC structure holes the mode index is reduced. As an example of square lattice, the fill factor f is give by $\pi \cdot (\frac{r}{a})^2$ = 0.075, where r is the radius of the holes and a is the lattice constant (pitch). The average refractive index is expressed as:

$$n_{eff} = (1 - f) \times n_{slab} + f \quad [136] \qquad 4.2$$

The n_{eff} of the TE and TM PCs modes are 1.54 (TE) and 1.51(TM) respectively. By using the value of 1.54 for TE mode, it gives the propagation constant k_0 of 12.326 μm. Two more reciprocal lattice points now intersect with the Ewald circle (solid red), which provides four in-plane coupled modes indicated by yellow arrows.

Couplers with a large in-coupling angle (AOI) are not robust from azimuthal coupling angle perspective (a small change in in-plane propagation direction will affect the coupling angle a lot), which means the in-plane wave vector needs to be precisely along a specific direction in order to achieve intersection between the Ewald circle and reciprocal lattice points. However by changing the coupling angle (AOI) near 90°, azimuthal rotation will not be an issue for coupling. The detail will be introduced in Chapter 5.

4.5 Effect of PCs parameters on coupling conditions for hexagonal lattice.

Coupling conditions such as coupling strength, wavelength and angle are dependent on a number of geometric parameters. Effect of incident light polarization state (TE and TM), lattice period, hole diameter, propagation direction and thickness of slab waveguide core layer are now investigated for a hexagonal lattice PC in order to better understand how these parameters affect coupling performance. Angle resolved dispersion maps are created by RCWA simulation and analysed.

4.5.1 Effect of polarization state

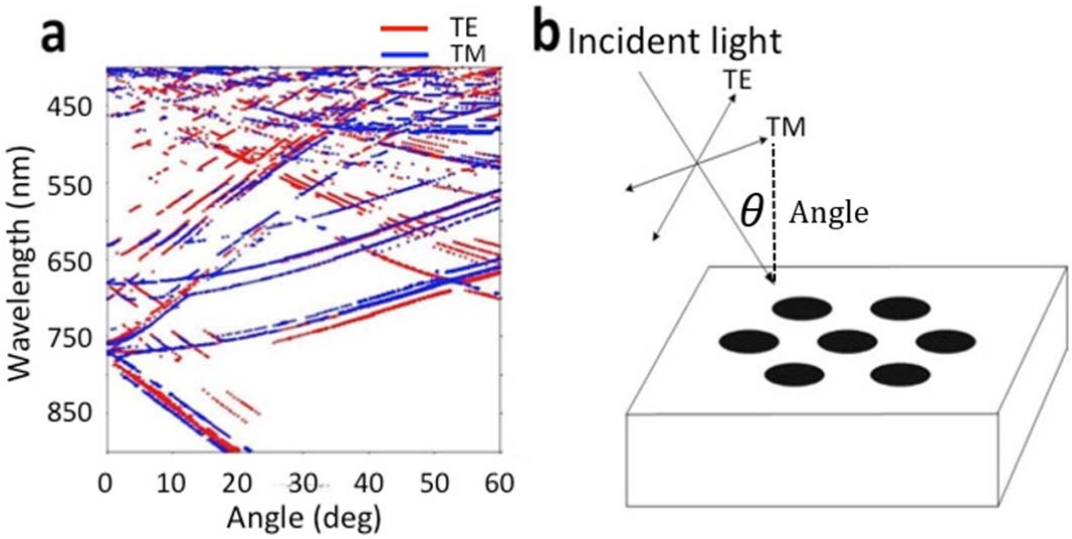

Figure 26. a) Photonic crystal bands extraction from RCWA-calculated dispersion maps of hexagonal lattice with 570nm lattice constant and 114nm hole diameter b) polarization convention.

Figure 26 shows the dispersion curves generated by RCWA simulation for TE and TM polarized incident light. In this case the direction of incident light propagation is along the Γ- X symmetry direction. Arrows show the orientation of the electric field vector for electromagnetic fields. We observe that the coupling conditions change slightly (1.5°)for TE (red curve) and TM (blue curve) polarizations.

4.5.2 Effect of direction of 'in-plane' wave vector

Figure 27 shows Photonic crystal bands extracted from RCWA-calculated dispersion maps for a hexagonal lattice with 570nm lattice constant and 114nm hole diameter. Blue and red bands correspond to incident wave vector oriented along the $\boldsymbol{\Gamma - M}$ and $\boldsymbol{\Gamma - X}$ symmetry directions respectively.

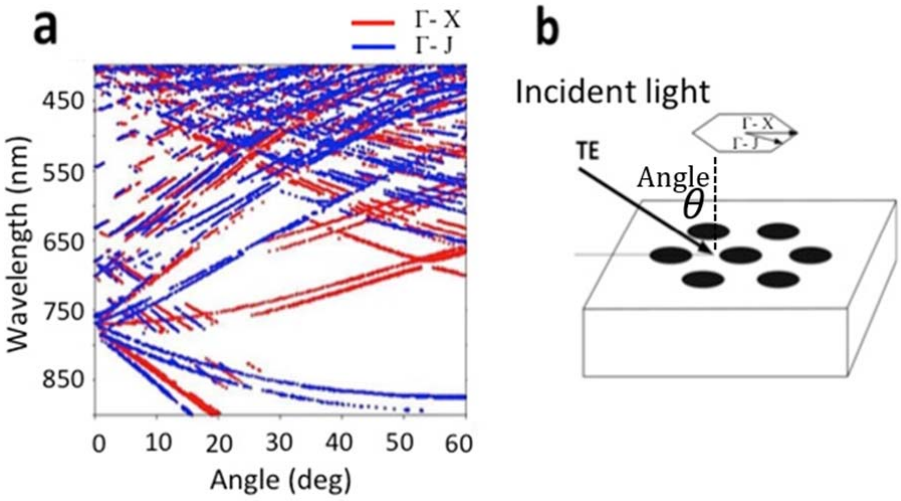

Figure 27. Different in-plane wave vector of incidence (TE polarization) on PCs with hole diameter of 120 nm and lattice constant 580nm.

We expect that in-coupling conditions should be almost the same for both Γ- X and Γ- J directions close to the Γ point (corresponding to normal incidence). It is noticeable that bands diverge in different ways with increasing angle of incidence. This is because the mode effective indices are different for the two propagation directions due to a difference in air fill factor.

4.5.3 Effect of hole diameter

Hole size is another crucial PC parameter. *Figure 28* shows comparison of coupling conditions for hexagonal lattice (pitch : 570nm), TE polarized incident light oriented along the $\Gamma - X$ direction. Change in holes size causes change in air fill factor which in turn changes the effective mode index

and so affects photonic crystal coupling angle. The simulation shows that the bands blue shift as the holes size becomes smaller (increasing mode effective refractive index). Hence operating wavelength can be tuned slightly by changing the hole diameter.

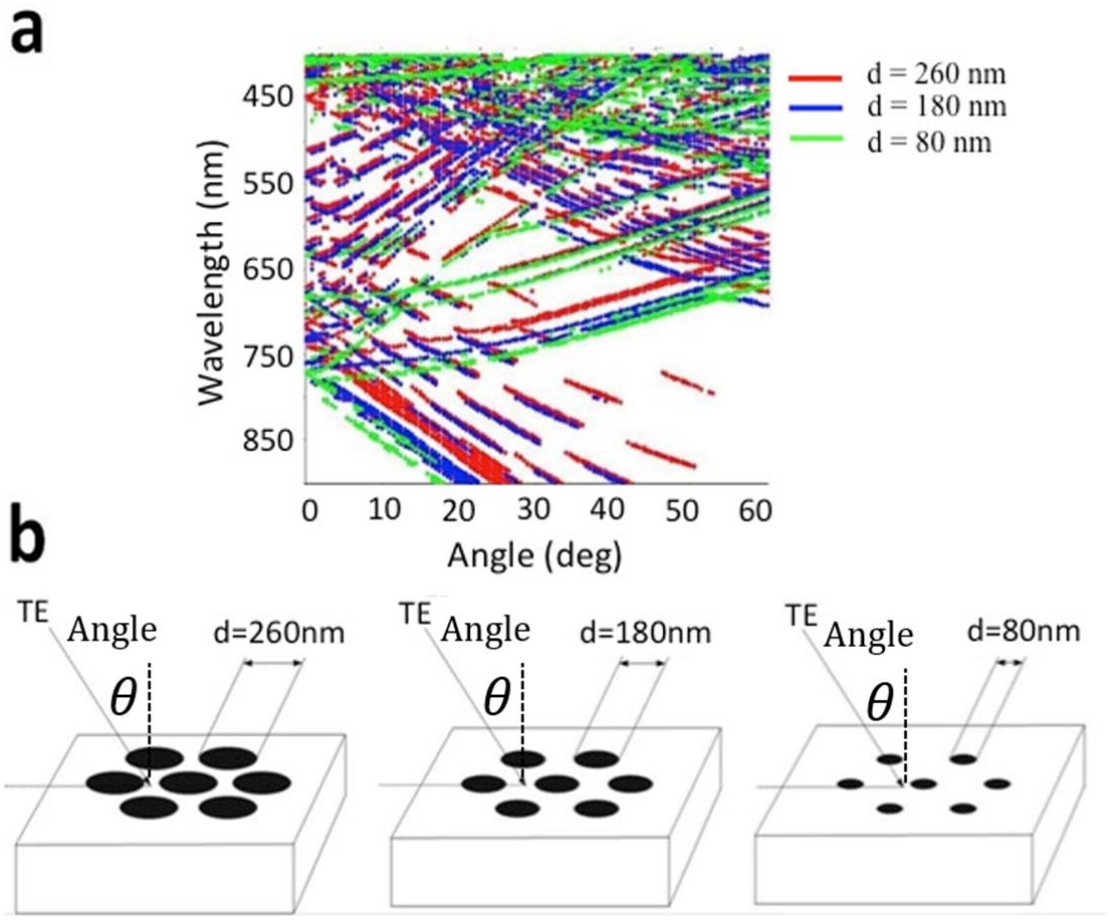

Figure 28. a) Photonic crystal bands extraction from RCWA-calculated dispersion maps of hexagonal lattice with 570nm lattice constant and different holes diameter. Red bands represent the hole diameter of 260nm, Blue bands represent the hole diameter of 180nm and green bands represent the hole diameter of 80nm. The source is injected along $\boldsymbol{\Gamma - X}$ *direction. B) schematics of simulation models.*

4.5.4 Effect of slab waveguide core thickness.

Slab waveguide core thickness is another parameter that will affect the coupling angle at the working wavelength. It also directly affects the mode effective index. *Figure 29* compares coupling conditions for several SiON core thickness (300nm, 400nm and 530nm) and fixed lattice constant and hole diameter, with TE polarized incident light oriented along $\Gamma - X$ direction. Again bands consistently shift to shorter wavelength as the core thickness decreases from 530nm to 300nm.

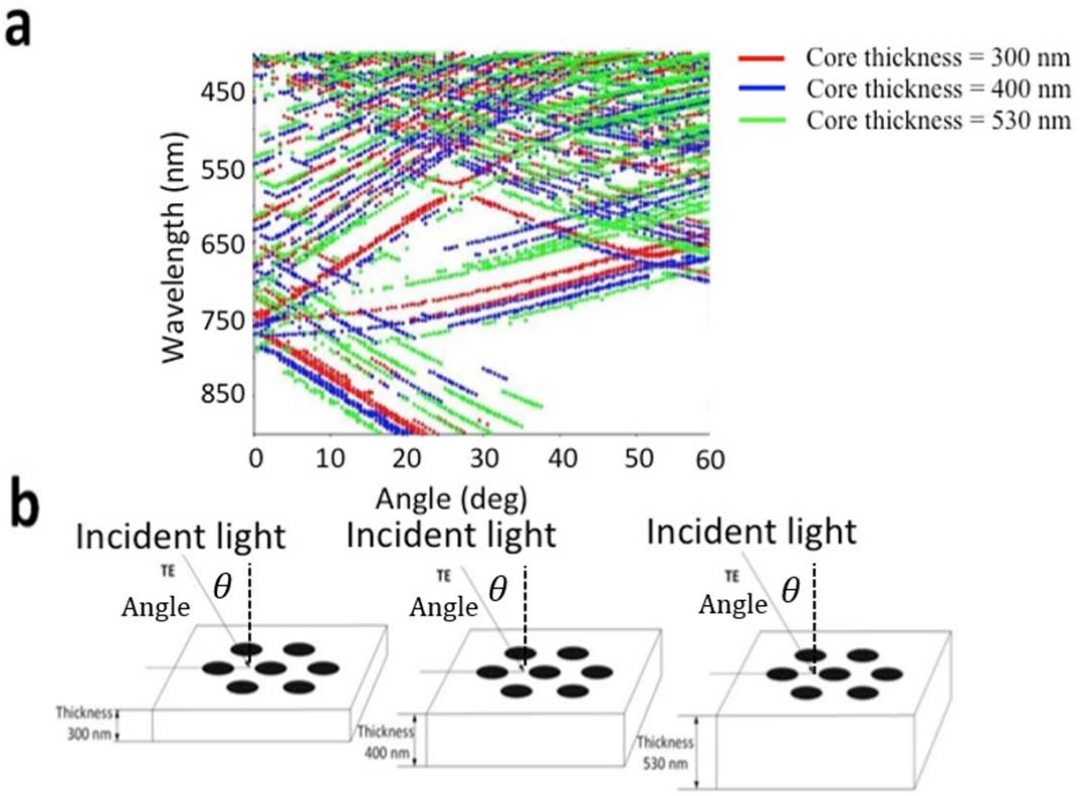

Figure 29. a) Photonic crystal bands extraction from RCWA-calculated dispersion maps of hexagonal lattice with 570nm lattice constant and 114nm hole diameter with core thickness of 530nm (green), 400nm (blue) and 300nm (red). b) schematics of simulation models.

4.5.5 Effect of lattice constant.

Figure 30 compares coupling for several lattice pitches with fixed hole diameter, slab waveguide core thickness and TE polarized incident light oriented along the $\Gamma - X$ direction. If hole size is constant lattice pitch will affect the effective fill factor: $f = (2\pi/\sqrt{3})(r/a)^2$. f will decrease $\propto \frac{1}{a^2}$ with increasing pitch. The mode effective index from equation 3.2 can be reformed as:

$$\mathrm{k} = \frac{2\pi}{\lambda}[\mathrm{n_{core}} + \mathrm{f} \times (\mathrm{n_{hole}} - \mathrm{n_{core}})] \qquad 4.3$$

As a result the mode effective index will reduce with decreasing f. From the plot we observe that bands again move to shorter wavelength as the lattice constant decreases.

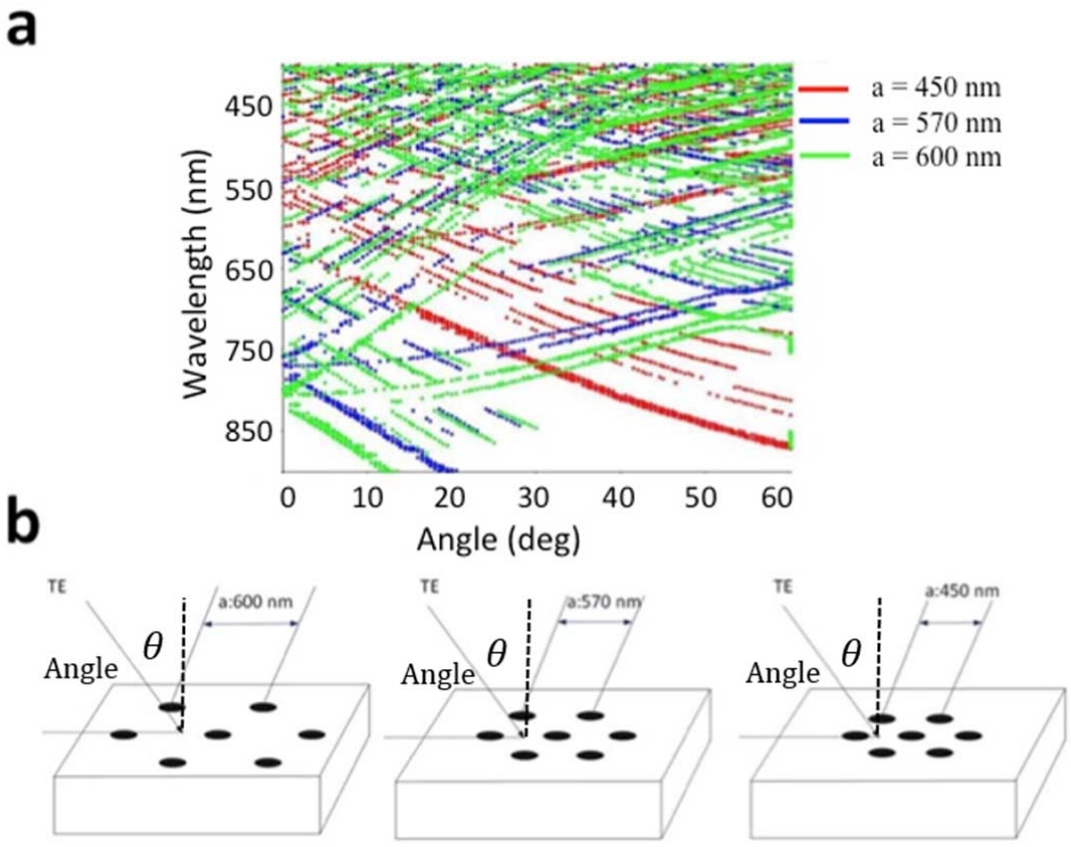

Figure 30. a) Photonic crystal bands extraction from RCWA-calculated dispersion maps of hexagonal lattice with 114nm hole diameter, 400nm core thickness and different lattice constant 450nm (red), 570nm(blue) and 600 (green). b) schematics of simulation model.

4.6 Summary

In this chapter the photonic crystal coupler is introduced. Firstly, the fundamental diffraction physics as the key theory of this coupler device is described. Secondly the structure of PCs integrated on slab waveguide are illustrated. Thirdly the design methodology of the coupler is explained in detail including Ewald circle construction. The rigorous coupled wave analysis is conducted in order to investigate the coupling condition by changing the parameters of PCs and incident light source. Coupling and splitting 633nm laser beam is achieved by proper PCs design (square lattice and hexagonal lattice), coupling for 785nm light source is also verified by RCWA simulation and Ewald circle construction.

Chapter 5: Optimised vertical coupler for integrated sensor system

As shown in the previous section, with careful selection of lattice period and etched hole size it is possible to couple and simultaneously split a monochromatic laser source at any chosen wavelength (633nm/785nm) to a slab waveguide. By adjusting the PC lattice shape to control the symmetry, it is possible to arbitrarily determine how many split beams will be generated in the slab waveguide after coupling. Tuning the geometrical design parameters discussed in the last section allows precise vertical coupling. Couplers based on square and hexagonal lattice with small vertical offset angles, and preferential coupled channels were demonstrated.

5.1 Design of vertical coupler with square lattice and hexagonal lattice structure

To move forward to development of a large channel count sensor, the coupler must now be optimised to provide vertical coupling, along with large channel count. This section deals with how to determine the number of split beams generated in the slab waveguide. This relates to PC lattice symmetry number. Photonic quasicrystals provide a means to arbitrarily select the symmetry number above and beyond the maximum 6 found in nature. Hence 12-fold symmetric photonic quasi-crystal lattices are now explored in comparison to 6-fold symmetric hexagonal lattice. Couplers with vertical input angle devices are designed, fabricated and tested.

Schematics of near vertical coupling and beam splitting at 785nm are shown in Figure 31. As before, it is instructive to visualize the phase matching conditions in frequency (k space) using the Ewald sphere construction [137]. As mentioned before, although higher order Bragg peaks can be used for coupling, primary Bragg peaks (corresponding to first order diffraction conditions) yield the strongest coupling efficiency [138][139] and typically eliminate additional out-of-plane diffraction losses.

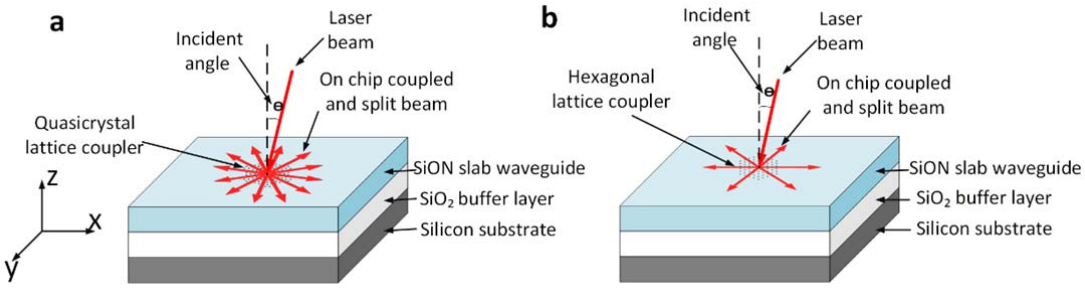

Figure 31. Schematics of light coupling and splitting on photonic crystal structures. a, quasicrystal lattice and b, hexagonal lattice couplers/splitters.

The diffraction pattern (reciprocal lattice) of the hexagonal photonic crystal and 12-fold quasicrystal are shown in Figure 32. The diffraction pattern clearly demonstrates the expected 6-fold rotational symmetry for hexagonal and 12-fold rotational symmetry for PQC, with the strongest points (primary Bragg peaks) located in the inner circle (shown in red). The 1st Brillouin zones are shown as insets. The central red circle encloses the primary Bragg peaks. It should be noted that unlike the hexagonal lattice there are several additional peaks in close proximity in the diffraction pattern for the PQC lattice. Those peaks have very low diffraction efficiency but can cause some diffraction loss, bearing in mind that diffraction strength is proportional to the Fourier coefficient[140] amplitude. *Figure 32* a) is generated by hexagonal lattice (holes diameter : 114 nm, lattice constant : 575nm) and *Figure 32* b) is generated 12-fold quasicrystal lattice (holes diameter: 114 nm, lattice constant: 570nm), all the diffraction patterns are produced by FFT (Fast Fourier Transform Algorithm).

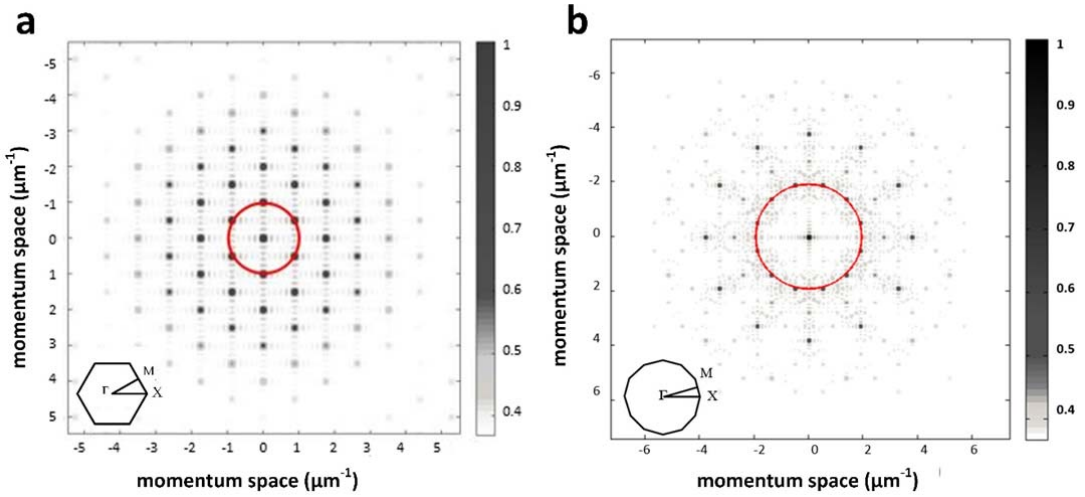

Figure 32. Comparison of hexagonal lattice and quasicrystal lattice in reciprocal space. a) hexagonal lattice in reciprocal space. b) 12-fold quasicrystal lattice in reciprocal space.

To achieve uniform symmetric coupling and splitting, it is necessary to couple incident light at normal (vertical) or near normal incidence to the surface. This yields 6 split beams for the hexagonal coupler and 12 split beams for the 12-fold quasicrystal coupler. The center of the Ewald circle is co-located with the most central Bragg peak. According to Braggs law the primary Bragg peaks are caused by first order diffraction given by equation 5.1:

$$\Lambda = \frac{\lambda}{n_{eff} - sin\theta} \qquad 5.1$$

where Λ is the distance between two lattice points (black filled circle), n_{eff} is the effective index of the stable photonic crystal waveguide mode, λ is the free-space wavelength, and θ is the incident angle (θ is depicted in Figure 31) relative to the surface normal. In order to construct the Ewald circle, we convert the equation above to its reciprocal space representation to give equation 5.2:

$$\beta - k_0 sin\theta = G \qquad 5.2$$

where β is the mode propagation constant ($k_0 n_{eff}$), k_0 is the wave vector in free space and G is a reciprocal lattice vector given by $2\pi/a$. As discussed previously the mode propagation constant (in-plane wave vector) in the photonic crystal area lies between $k_0 n_{core}$ and $k_0 n_{sub}$ and is lower than the effective index of the SiON slab waveguide mode.

There will be a tradeoff between diffraction efficiency and even splitting of the beams. Normal (vertical) incidence of light to the photonic crystal surface results in even beam splitting to n-channels where n is the lattice symmetry. However it also allows 'in-plane' second order Bragg reflection back into free space reducing total coupled power [141]. In Figure 32 the Ewald sphere is shown as a solid circle with radius β for both the hexagonal and quasicrystal lattice. The intersection of this circle with the primary Bragg peaks yields the 'in-plane' guided mode conditions. The power coupled to the in-plane guided mode relates to the magnitude of associated Bragg peaks.

Computer modelling of the hexagonal lattice coupler was again performed using the Rigorous Coupled Wave Analysis method. Total reflected power is calculated for a wide range of incident angles (θ) and wavelengths. RCWA method is far preferable to conventional plane wave band structure calculations as the results take into account the complete geometry of the 3-dimentional system including the slab waveguide layers and substrate.

Once designed, devices were fabricated and using the automatic spectroscopic reflectometry system (described in Appendix A), a collimated super continuum light source with wavelength range 400 nm to 900 nm was incident to the coupler device over an angular range of 0 to 60 degrees. After normalising data to the Laser spectrum this produces the

angle-resolved dispersion/ coupling map for the hexagonal lattice as shown in Figure 33. The dispersion bands are extracted from the experimental reflectometer data using gradient analysis combined with a peak detection algorithm.

In the angle-resolved zero-order reflectance map (Figure 33 a), broad fringes (which curve upwards towards shorter wavelength with increasing angle of incidence) are due to Fabry-Perot interference in the underlying buffer layer and are not related to the operation of device. Hence we filter these out to create Figure 33 b. The sharp narrow lines in Figure 33b (dispersion bands) represent the coupling condition for photonic crystal modes. The lower bands have linear behaviour and always show strongest coupling for photonic crystal modes. The fundamental band becomes nonlinear with respect to coupling angle around the Gamma point Γ (normal/vertical Incidence). The weaker bands with similar angular response indicate coupling to modes of the underlying SiO_2 buffer layer.

Example features are highlighted with red labels. Because we focus on normal incidence at 785nm wavelength, the hexagonal lattice PC was simulated for a range of lattice pitch and hole diameters to determine the precise design parameters, and process window for both TE and TM modes. Figure 33c shows the change in zero-order reflectance for each lattice parameter. The lower band corresponds to TE modes and the higher band TM modes. Simulations for the 12-fold lattice are omitted because it is not possible to simulate using the RCWA method. However due to the similarity of six-fold hexagonal and the 12-fold lattice, we can use results from the hexagonal lattice to guide the design for the 12 fold lattice. All the plots in *Figure 33* are obtained from RCWA simulation.

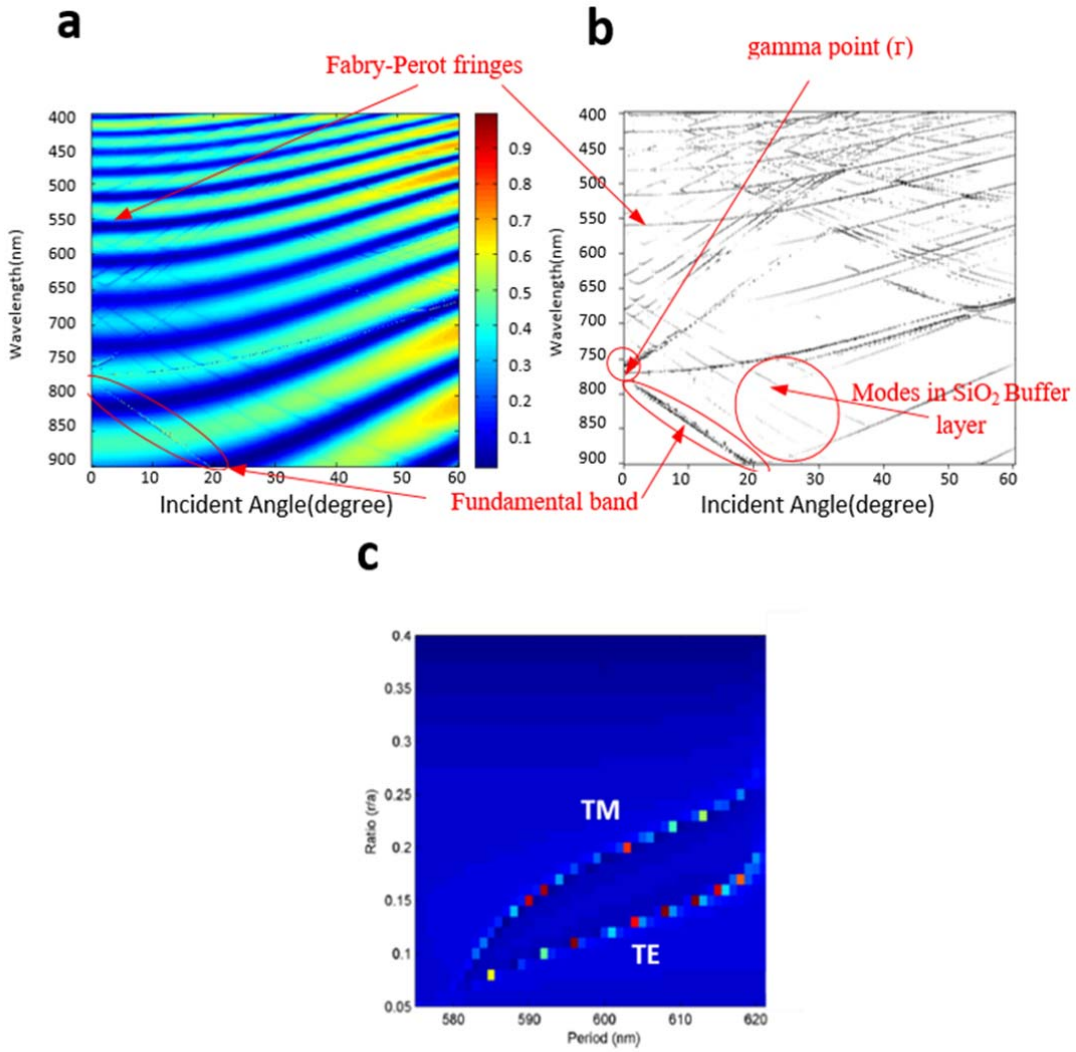

Figure 33. Angle-resolved zero-order reflectance map of a hexagonal lattice coupler showing the coupling angle is near 0 degree at 785 nm. a) raw simulation data, b) filtered simulation data with extracted bands. C) zero-order reflectance for each lattice type for TE and TM.

The real-space lattice structure for the hexagonal PC and PQC are shown in Figure 34 a and b. The diffraction patterns (reciprocal lattice) are illustrated in Figure 34 e–h. The diffraction patterns clearly demonstrate the expected 6-fold rotational and 12-fold rotational symmetry, with the strongest points (primary Bragg peaks) located in the inner circle (shown in green in Figure 34). The 1st Brillouin zone and Γ point are shown as insets in Figure 34 e and g.

Normal incidence requires that the k vector of the incident light source is perpendicular to the surface of the 2D photonic crystal slab. An off-normal coupling angle is used in our experiment because the fabrication tolerance of these photonic crystal and quasi-crystal, in terms of hole size and shape, are not perfect to the design specifications, and this slightly affects the coupling conditions and beam splitting ratio.

According to the design specifications, exactly vertical incidence should achieve coupling and multi-beam splitting, whereas due to small imperfections in fabrication for our demonstrator device, coupling is achieved at a very small offset angle. Figure 34 shows the vertical coupling and near normal incident coupling concept and how the beam splitting will be affected according to the theory. Figure 34 c and d shows the concept of in-coupled guided modes in photonic crystal/photonic quasi-crystal with normal incident light and near normal incident light (θ) respectively.

In Figure 34 the solid red arrows indicate in-coupled light and the dotted red lines indicate unwanted reflections in the 'normal incidence' coupling scenario. These back-reflections can be avoided with 'near normal incidence' coupling. The comparison between 'normal incidence' coupling and 'near normal incidence' coupling is shown in Figure 34 e and f for quasi-crystal lattice and Figure 34. g and h for hexagonal lattice photonic crystals. Figure 34 e–h shows a reciprocal lattice space representation of the lattice pattern (Fourier transform), and we follow the Ewald construction to predict coupling conditions as follows:

A vector is drawn with length k_x terminating at one of the reciprocal lattice points. k_x is equal to 0 for normal incidence angle and $k_0 \sin\theta$ for an incidence angle of θ respectively, as indicated on the x-z plane cross section above Figure 34. e–h. k_0 is the magnitude of the incident vector at the operating wavelength. The Ewald circle is superimposed as a green circle with a diameter matching the 'in-plane' mode propagation constant. This is centred at the reciprocal lattice 'origin point' k_0. For multi-beam coupling to occur, it is necessary for the Ewald circle to intersect a number of reciprocal lattice points (in k-space). Under perfect conditions (Figure 34 c), the propagating wave-vectors are phase matched to the lattice, and so the orange arrows in (Figure 34 e) indicates the allowed coupled mode propagation directions. The width of these arrows schematically indicates the strength of each scattered beam, in this perfect scenario the coupling strengths are equal.

If the Ewald construction interacts with higher order Bragg peaks, this may result in the in-plane modes leaking from the core layer. This is due to the light line (shown as a red circle in Figure 34 g) which relates to extent of waveguide confinement, being within the Ewald circle (green line). The radius of the red circle (light line) corresponds to the maximum allowable k-vectors (actually β) for mode confinement and hence light propagation for the SiON slab waveguide.

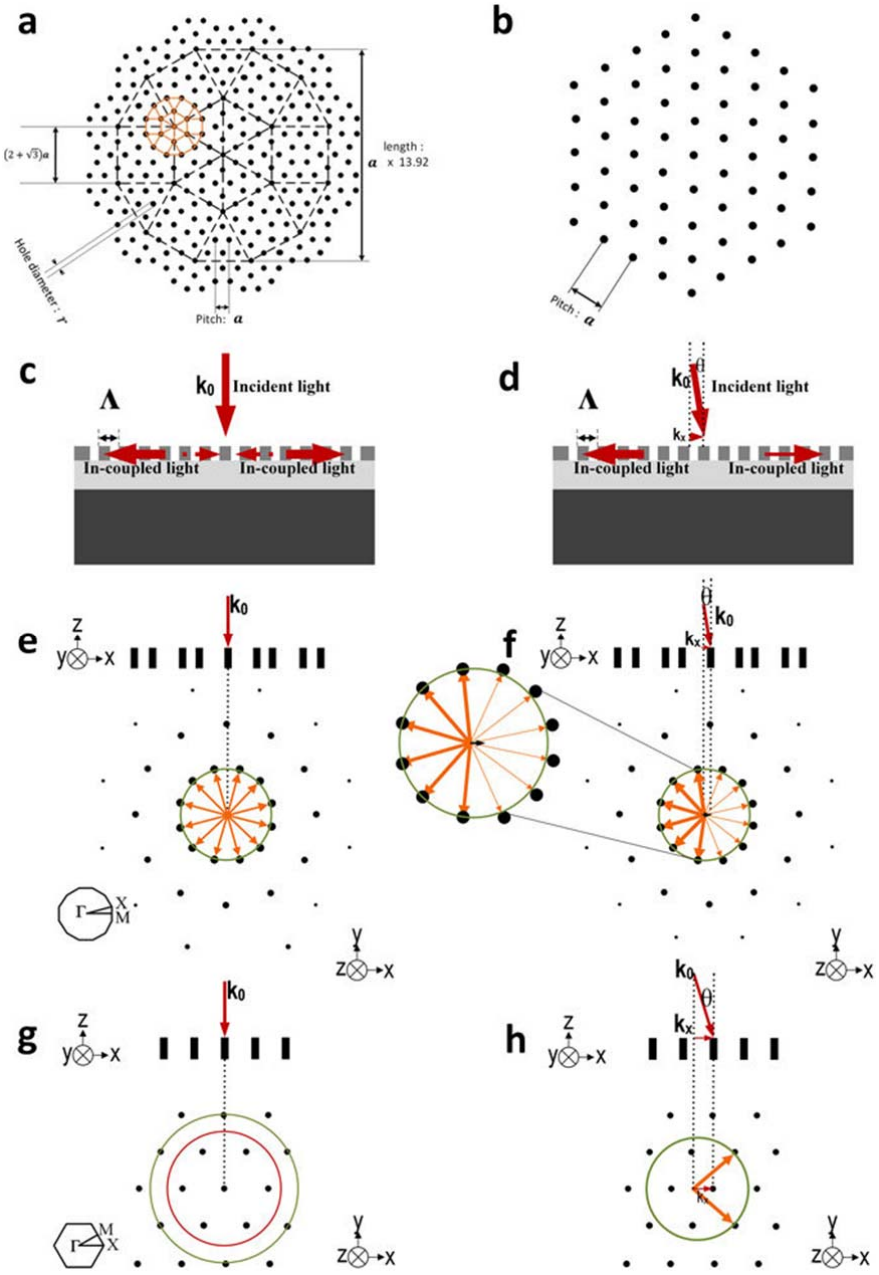

Figure 34. Comparison of hexagonal lattice and quasi-crystal lattice in free space and reciprocal space. (a) Real-space lattice of square-triangle tiling random-Stampfli quasi-crystal lattice structure. (b) Real-space lattice of the hexagonal lattice structure. (c) Schematic cross-section showing normal incidence coupling to the waveguide mode. (d) Schematic cross-section showing near-normal incidence coupling to the waveguide mode. (e) Ewald circle construction of a quasi-crystal lattice in reciprocal space with normal incidence coupling. (f) Ewald circle construction of a quasi-crystal lattice in reciprocal space with near-normal incidence coupling. (g) Ewald circle construction of a hexagonal lattice in reciprocal space showing the light-line in red. (h) Ewald circle construction of a hexagonal lattice in reciprocal space with a large offset-incidence angle. Green circles represent the Ewald circle construction. Yellow arrows indicate the allowed coupled mode propagation directions and the width of the arrows schematically indicate the strength of each scattered beam.

If the incidence angle θ is slightly near-normal (as shown in Figure 34 f), then the centre of the Ewald circle will shift position, and no longer corresponds to the 'origin reciprocal' lattice point and results in the case shown in Figure 34 f. An inset shows a magnified view in Figure 34 f, highlighting the slight shift in the centre position and so intersects different first order Bragg peaks (reciprocal lattice points). This results in a variation in the coupled beam strengths and the number of split beams. A large offset-incidence angle will result in reduced beam splitting. In Figure 34 h we show this effect in relation to a hexagonal lattice. In this case only 2 lattice points intersect with the Ewald circle and it results in 2 split beams. This is a full explanation of the physical processes at play in the demonstrator devices presented in chapter 4, which had only 2 split beams.

The hexagonal and quasicrystal couplers were characterized using both angle-resolved spectroscopic reflectometry (see Appendix B for description of the system) and a bespoke setup (*Figure 35* g) designed to permit observation of the beam splitting, the setup consists of a beam deflecting mirror (F), an X/Y stage (G) with a custom-made mount, a fixed-focus collimator (B) screwed into a rotation mount, an iris aperture (C), a 100 mm plano-convex lens (D), a 785 nm PM fibre pigtailed laser diode (A) with a typical output power of 7.5 mW, and a silicon CMOS camera to image the coupling (E). The 785 nm laser diode is the source of incident light and the fibre is terminated with the fixed-focus collimator in a rotation mount, which is used for selection of s/p polarization. S polarization is chosen in this case. The iris aperture is used to control the beam diameter and, by extension, the range of incident angles introduced by the plano-convex lens used to focus the beam on the surface. A larger beam diameter and angular range broadens the range of in-plane propagation angles for the coupled modes. Finally, the beam is reflected onto the stage-mounted sample by a rotating deflection mirror. The mirror and X/Y stage allow quick optimization of the input coupling conditions. The silicon CMOS cameras are used to capture the light coupling and splitting.

Figure 35 shows Angle-resolved spectroscopic reflectometry data for the hexagonal and quasicrystal couplers. The photonic crystal mode lines (bands) precisely show the actual coupling conditions. Extremely good agreement with the simulation data is observed. The coupling angle is about 0 degree at 785 nm incidence, same dispersion bands and Fabry-Perot interference fringes in both simulation and reflectometry experimental data. Normal incident coupling matched up quite well in hexagonal lattice, while there is about 20nm offset for the 12-fold quasicrystal coupler. The photonic crystal bands are indicated by the

dash black lines in Figure 35(a) and (c). The fundamental bands (first band from high wavelength), which are used to diffract the beam in this design.

Successful near-vertical coupling and beam splitting is visually shown in Figure 35 b and d for the hexagonal and quasicrystal lattice couplers on Si substrate device with light at 785nm. The hexagonal coupler clearly shows 6-way splitting while the quasicrystal shows 12-way splitting (labelled by red number in Figure 35(b) and (d). The coupling angle is preset to 4 degree in order to achieve coupling for the quasicrystal design. It is difficult to achieve split beams with equal intensity without perfect normal incidence angle. More information for Dispersion maps of different azimuth angles are shown in Appendix A.

The trench isolation in Figure 35 e is used to separate each beam physically, each of the isolation trenches were 12 μm wide lines. They were etched into the SiON thin film as well as the photonic crystal/photonic quasicrystal couplers with the same ebeam Mask. They will not introduce extra loss from the coupler mode, because they are not on the beam path.

Following good practical success with the silicon substrate devices, the hexagonal and 12-fold quasi-crystal couplers were fabricated on a borosilicate glass wafer. The incident coupling angle was 0° at 785nm and equal intensity beam splitting with 'perfect' normal incidence angle was achieved, proving that the design methodology works excellently. Filtered dispersion band diagrams and beam splitting images are shown in Figure 36. Figure 36 (a) and (d) show 785nm light coupling to a hexagonal and quasicrystal lattice coupler respectively. Figure 36 (b) and (e) show the zero- angle reflection data for hexagonal and quasicrystal lattice couplers respectively and it shows the photonic crystal dispersion bands with the fundamental band highlighted. Figure 36 (c) shows a scanning electron microscope (SEM) of a hexagonal lattice device and Figure 36 (f) shows a cross-section SEM image of the quasi-crystal structure showing the depth and shape of the holes.

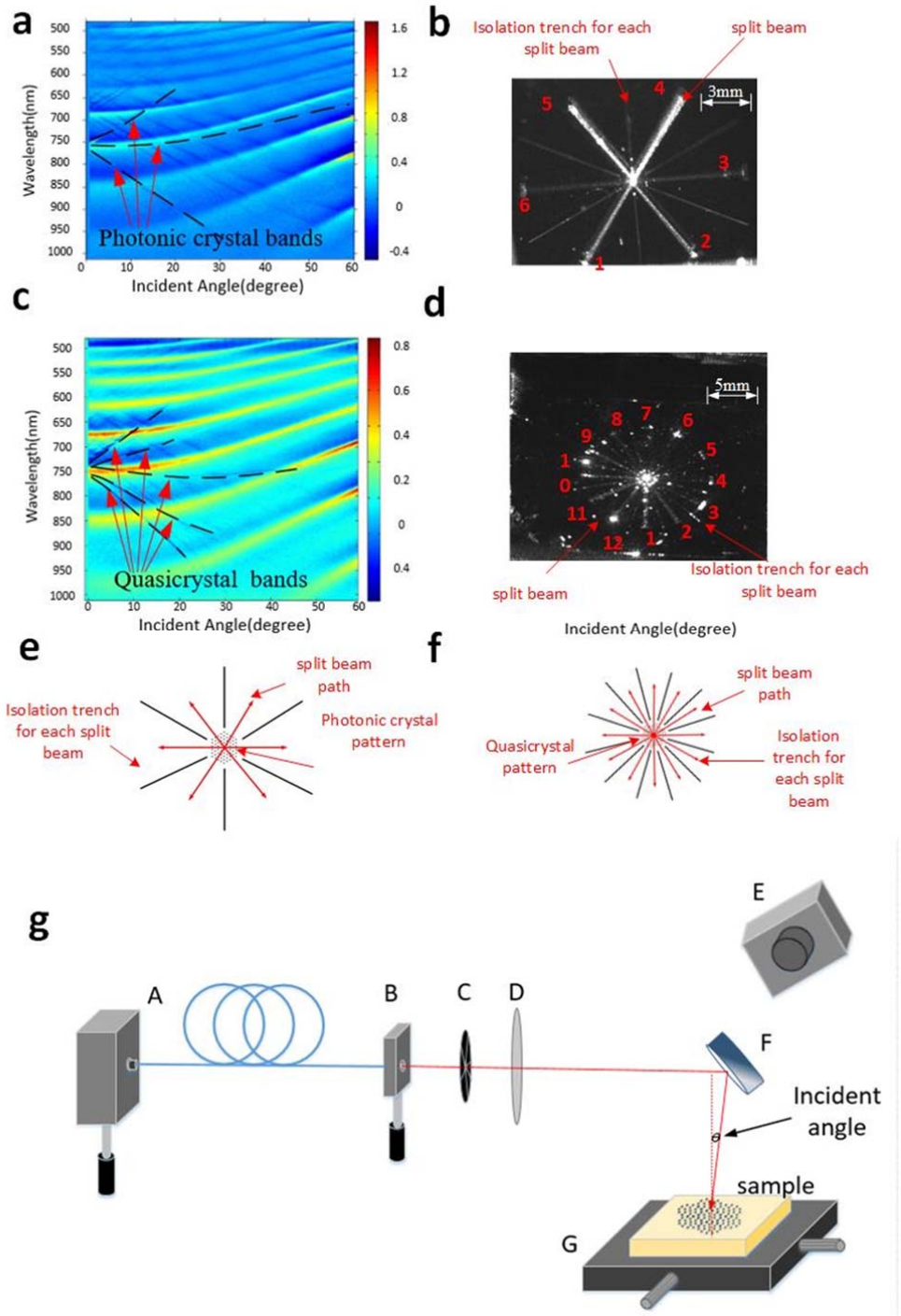

Figure 35. Performance measurement by Reflectometry and visible coupling demonstration. a,angle-resolved zero-order reflectance map of a hexagonal lattice coupler showing the couplingangle is near 0 degree at 785 nm (raw experiment data). b, image of light coupling and beam splitting on hexagonal coupler. c,. Angle-resolved zero-order reflectance map of quasicrystal lattice coupler showing the oupling angle is near 0 degree at 785 nm (raw experiment data) d, coupler image of light coupling and beam splitting on quasicrystal lattice coupler. e, layout of hexagonal . f, layout of quasicrystal lattice coupler. g, schematic of demonstration set up.

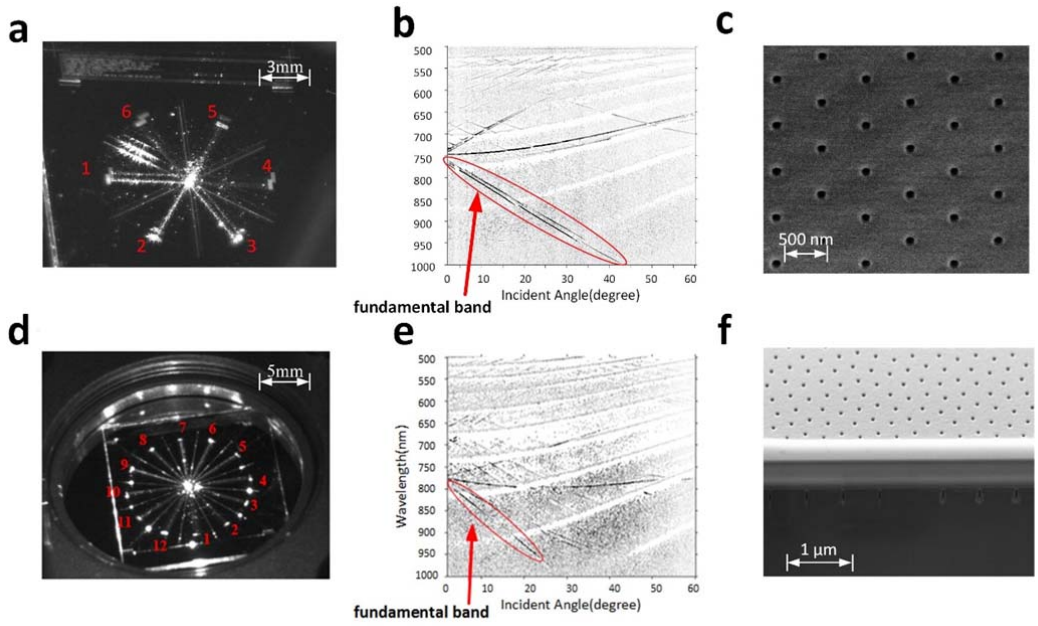

Figure 36. Light coupling on quasi-crystal structure with borosilicate glass substrate. (a) Image of 785 nm light coupling on a hexagonal lattice structure. (b) Angle-resolved zero order reflection measurement of a hexagonal lattice (filtered experimental data). (c) Top view SEM image of the hexagonal lattice structure. (d) Image of 785 nm light coupling on quasi-crystal structure. (e)Angle-resolved zero order reflection measurement on a quasi-crystal structure (filtered experimental data). (f) Cross section SEM image of the quasi-crystal structure.

5.2 Comparison of coupling efficiency in relation to lattice type.

The coupling efficiency of the fundamental mode of the PC couplers will decrease when the symmetry of the lattice is higher. The coupling efficiency of each photonic crystal coupler can be measured in practice by optical transmission measurements. To do this, a broad band super continuum laser is directed on to the coupler at 0° incidence and transmission spectra measured from the back of the sample using a fiber connected spectrometer. This was again done using the computer controlled reflectometry system. Resonant dips should appear around 785 nm where coupling occurs (power gets removed from transmitted beam due to coupling). Figure 37 shows raw (un-normalised) transmission spectrum for square, hexagonal and quasicrystal lattices. Apart from the spectral shape of the Laser and collection system, we can clearly see a sharp dip at 785nm. Looking at the extinction ratio of this dip, we see

that coupling to the square lattice is strongest followed by the hexagonal lattice coupler. As we expected the performance of the quasicrystal coupler is the poorest. The square lattice coupler gives the best coupling efficiency compared to the other two couplers. Almost 45% light at resonance wavelength (785 nm) was coupled and confined to the slab waveguide. The rest of the light transmits though the substrate and diffracts out of the coupler in higher orders. It is very challenging to measure the absolute coupling efficiency in the way commonly used for grating couplers [142] since we have multiple beams, and this was beyond the scope of this thesis.

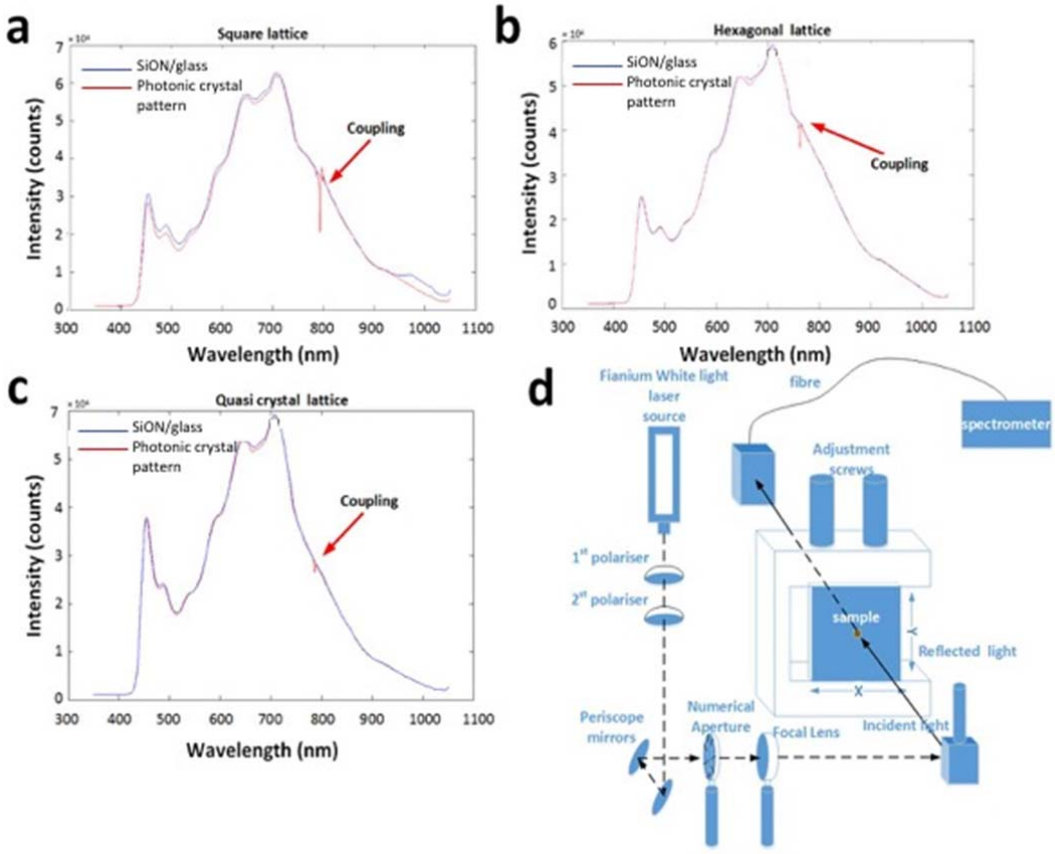

Figure 37. Coupling efficiency of each lattice type by transmission measurement. a) square lattice, b) hexagonal lattice, c) quasicrystal lattice. d) schematic of experiment set up.

Chapter 6: Sensor device based on Angle Resolved Out coupled Mode Analysis (AROMA)

As explained in Chapter 3-4, phase-matching conditions govern light interactions within planar waveguides incorporating gratings or photonic crystal structures. This was exploited to provide simultaneous multi-beam splitting and vertical coupling. Photonic crystals are reciprocal devices, meaning that all physical processes work in reverse. Hence it is equally possible to use a photonic crystal as an output coupler for a waveguide. In this case by exploiting 'leaky' modes of a photonic crystal, light incident to the side of a photonic crystal (of the correct design) can be scattered out of the waveguide. Dependent upon the wavelength and effective mode index for the Photonic crystal Bloch mode (determined by the geometry), the exit angle of the out-coupled light will change. Hence the photonic crystal out-coupler can fundamentally perform the function of an integrated spectrometer whereby out-coupling projection angle changes with wavelength. This is depicted in *Figure 38*.

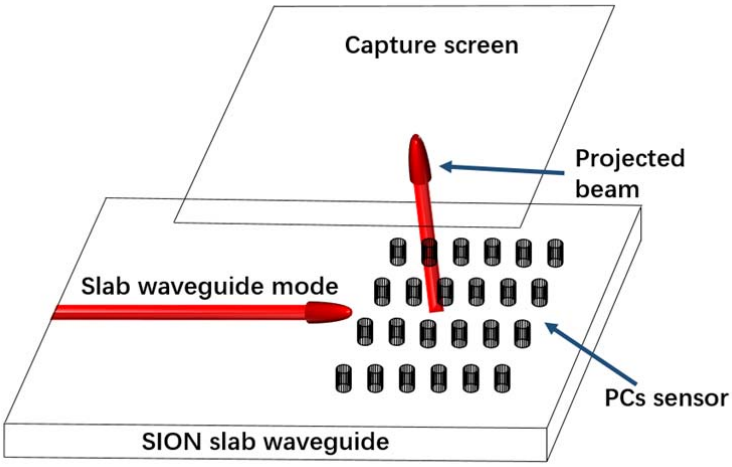

Figure 38. Photonic crystal sensor concept based on AROMA technology

Very small changes in effective index of the coupled Bloch mode inside the photonic crystal causes large shifts in resonance wavelength or projection angle. Since photonic crystal Bloch mode index is super sensitive to local environment inside the holes of the photonic crystal, environmental sensing schemes can be implemented by either monitoring wavelength for a fixed angle of incidence or by monitoring the angle of projection for a fixed wavelength.

Some work has previously been undertaken on 1-dimensional grating couplers investigating the effect of bio-chemical reactions at the surface [143]. This work investigates the changes in bulk

transmission spectra as a result of surface reactions on a Ta_2O_5 coated plastic substrates. In this case 1D gratings are fabricated on the surface of a transparent substrate and broadband light is incident exactly perpendicular to the back surface through the grating. Light transmitted through to the front is then collected by a spectrometer. This configuration investigates change in surface coupling angle for fixed wavelength as a result of molecules absorbed within a deep etched porous silicon grating. In this case monochromatic light is incident at an angle to the top surface of the grating and changes in specular reflection analysed.

Although these works appear superficially similar in mechanism of operation, its important to note that in both cases there is no lateral transfer of light from the grating to a surrounding waveguide. In fact there is no viable surrounding slab waveguide in either of these documents due to high absorption loss of porous silicon[144], and the geometry of the Ta_2O_5 device[143].

Detection of adsorbed molecules was demonstrated by Tiefenthaler and Lukosz[145], who investigated small changes in input coupling and projection angle for simple 1-dimensional grating couplers etched into the substrate / core interface of a TiO_2-SiO_2 slab waveguide (again these used higher order diffraction). In this case a focussed monochromatic laser beam couples to a single grating through the back of a transparent substrate, and diffracted light in the region of the same grating interacts strongly with the evanescent wave at the top surface where molecules are disposed. Readout mechanism is by measuring the angle of the out coupled beam which takes the form of an elliptical line. Brandenburg and Gombert adapted this system to use slab mode waveguiding [146]. In this case light couples to an input coupler grating through the back of a transparent substrate, and diffracted light in the region of another output coupler grating interacts strongly with the evanescent wave at the top surface where molecules are disposed [145].

These works all use conventional Bragg gratings with lattice pitch larger than the incident wavelength of light are used. Devices operate by method of Bragg-diffraction, the sensing mechanism utilizes higher than zero order diffraction orders, and sensitivity response is substantially linear.

Our devices are true photonic crystals as opposed to gratings meaning that they have sub wavelength (in the material) pitch, high refractive index contrast, and don not utilise conventional Bragg diffraction mechanism for vertical projection. Instead our devices have sub-wavelength periodicity in multiple dimensions (they are 2 dimensional lattices), and instead of utilising higher order Bragg diffraction (as is the case for simple gratings), they utilise photonic crystal super-prism effects which result from highly non-linear dispersion of guided Bloch modes associated with propagating waves inside the Photonic crystal. As a consequence super prism gives highly

non-linear change in projection angle for very small change in refractive index allowing huge increase in sensitivity to be achieved, whereas conventional diffraction mechanism is substantially linear in sensitivity.

The grating simply changes the surface scattering properties by process of diffraction, which manifests itself as an apparent change in surface absorption. In terms of the physics of operation these devices modify the scattering properties of non-guided high order 'leaky' waveguide modes which lie well above the mode confinement light line. Hence they can be accessed directly by surface reflection experiments, but not by truly confined waveguide modes of the photonic crystal or surrounding slab waveguide.

Overall, two-dimensional PCs provide greater design freedom and have the potential to achieve much higher sensitivity than their 1D grating cousins. To date, very little work has been undertaken on angular interrogation of 2D PCs slabs as an optical biosensing technique. Grego et al. used hexagonal-close-packed microspheres deposited on a silicon oxynitride slab waveguide to couple light from free space to guided modes. The intensity of the guided modes was monitored at the edge of the waveguide for a fixed angle of incidence as the surface was exposed to the analyte [147]. A 2D hexangular lattice PC integrated in a symmetric silicon waveguide was simulated by FDTD and shown to couple guided modes to free space domains[148].

In addition multiple channels are useful in various scenarios. In our target application, the channels allow multiple sensing elements, combined with a reference channel to provide environmental drift compensation.

The sensor is currently negatively detuned (Figure 39), i.e. the reciprocal lattice vector is greater than the propagation constant of the mode. There are no other in-plane or out-of-plane modes to couple to as the phase-matching condition is only satisfied for the 1st order diffraction in one direction (the 'backwards' direction). Solid red arrows indicate in-coupled light. Solid blue arrows indicate out-coupling from a mode incident from the left.

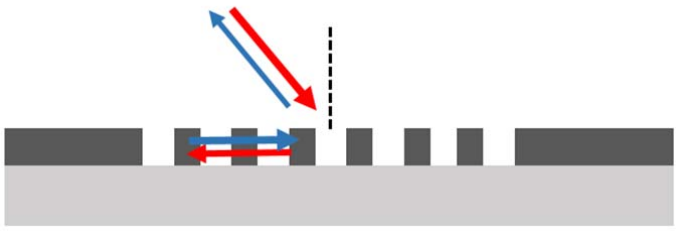

Figure 39. Negative detuned sensor configuration

6.1 AROMA based photonic crystal sensor on SiON waveguide

Fundamentally, the photonic crystal AROMA sensor behaves similar to an SPR sensor in that the effective index of a mode supported by the patterned area is modified by the deposition of a thin layer of molecules, in this case coating the interior surface of the holes. However unlike an SPR sensor the PC sensor does not require any gold metal coating. The photonic crystal sensor also provides multiple benefits over the simplistic grating sensor described by Lukosz et. al[149].

This technology provides a collimated unidirectional output beam whereas a conventional grating coupler converts the confined plane wave to a diverging projected elliptical wave which severely restricts the readout system. Even with sophisticated lenses placed over the gratings, light can only be imaged or focused to a similar size as the grating itself.

There are also significant differences in the physics of how the photonic crystal device works. The effective index of a propagating Bloch mode supported by the patterned photonic crystal area becomes significantly modified by ingress of deposited molecules into the holes, greatly changing coupling conditions between the photonic crystal and the surrounding slab waveguide. This change in Bloch mode index then causes 'confined' waveguide modes lying below the light line to become 'leaky' modes lying close to or above the light line, which then becomes projected vertically out of the guide at some angle.

By introducing periodicity in more than 1 direction, physical constrains apply to polar and azimuthal directions resulting in single or discrete directions [150]. Hence two-dimensional periodicity provides much greater freedom in tailoring the radiation characteristics of an output coupler.

In our multichannel sensor device, light is coupled to several fundamental modes in the SiON slab by a photonic crystal coupler, as discussed in the previous section. Light then coupled from the photonic crystal output coupler (sensor), which is positioned in the pathway of the guided mode. The out-coupled beam is then projected onto a screen (matte screen or camera). Any shift in the detected position indicates a change in the surroundings of the dielectric environment above the photonic crystal sensor.

6.1.1 3D FDTD modelling

6.1.1.1 Introduction of FDTD method

Sensor simulation was conducted by Finite-Difference Time-Domain method. It solves Maxwell's curl equation in non-magnetic material.

$$\nabla \times \vec{H} = \vec{J} + \frac{\partial \vec{D}}{\partial t} \quad 6.1$$

$$\nabla \times \vec{E} = -\frac{\partial \vec{B}}{\partial t} \quad 6.2$$

Two constitutive relations are linked $\vec{D}$ (displacement field) and $\vec{B}$ to $\vec{H}$ and $\vec{E}$ field respectively.

$$\vec{D}(t) = [\varepsilon_0 \varepsilon_r(t)] * \vec{E}(t) \quad 6.3$$

$$\vec{B}(t) = [\mu(t)] * \vec{H}(t) \quad 6.4$$

Where t is the time and μ is the permeability.

A circulating E field will give a change in H field at the centre of the circle, then the updated B field will introduce the H field in proportion to the permeability. The circulating H field gives a change in the D field in the centre of circulation. This D will introduce an E field in proportion to the permittivity. Then the new E field introduce another change in B field. Those equations are solved on a discrete special and temporal grid, and E field and H field are solved in slightly different location in the unit cell. We called it Yee cell [151].

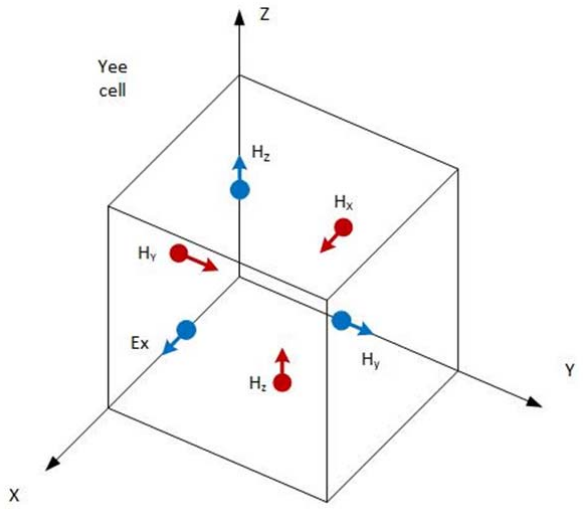

Figure 40 Yee cell with electric and magnetic field indicators

6.1.1.2 Photonic crystals FDTD model

The sensors (output couplers) must be designed for integration on a common SiON slab waveguide along with the photonic crystal input couplers. Therefore the same SiON slab wavguide (n = 1.7 at 785 nm, thickness 400 nm) was used as the starting point for sensor simulation. A square lattice was adopted for the photonic crystal lattice due to its low (4 fold) lattice symmetry and large Bloch mode dispersion. The actual wavelength dependent refractive index for the deposited SiON material was determined by spectroscopic ellipsometry and so full material dispersion is included for all simulations.

Figure 41 shows the cross section schematic for the FDTD model. This simulate a photonic crystal with a pitch of 450nm and hole diameter of 230nm etched into the 400nm thick waveguide core deposited on top of a silicon substrate with 2µm thick SiO_2(n= 1.46) buffer layer. The incident light source corresponds to the fundamental waveguide mode associated with the slab waveguide at 785nm. This ensures that the result is comparable to the real world conditions (coupled mode from waveguide to photonic crystal).

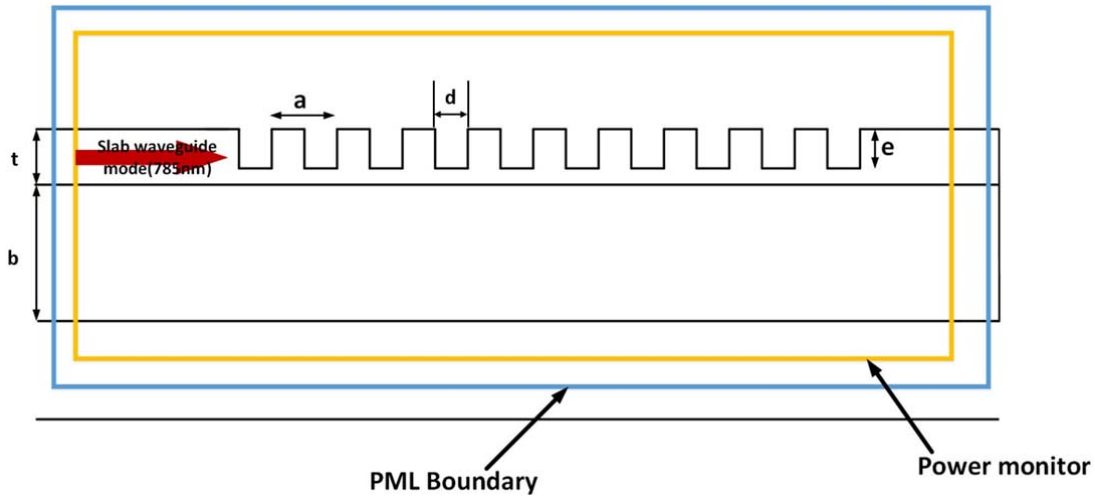

Figure 41. Schematic of the FDTD simulation domain for square lattice photonic crystal on SiON slab wave guide with core thickness t, buffer thickness b, etch depth e, hole diameter d and lattice constant a.

The grid density was adjusted to ensure every photonic crystal hole was sampled by at least 10 mesh points and the grid was aligned with the interfaces of the material. The red arrow indicates

the injected mode source. Power flows from left to the right boundary, and the farfield projection is monitored and displayed as a radial power plot.

An example result is shown in

Figure *42*. Far-field projection calculations for fundamental TE and TM slab modes gave vertical projection angles of -14.5 ° and -15.2 °respectively.

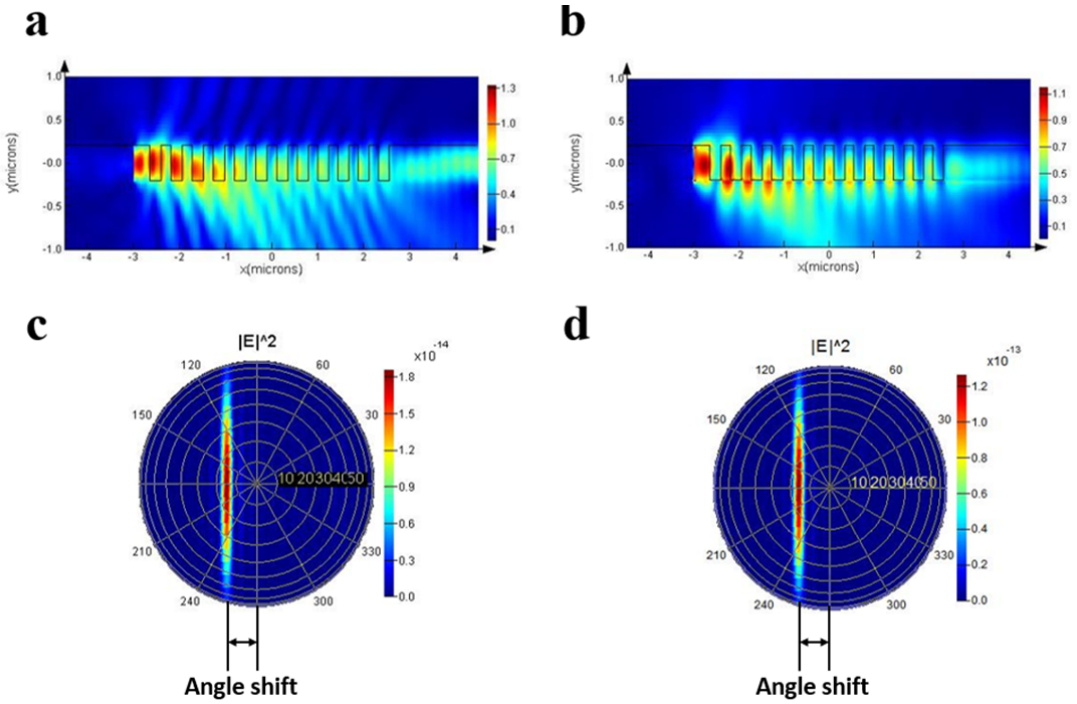

Figure 42. 3D FDTD simulation of E-field cross sections and corresponding farfield projections for PC sensor with 450nm lattice constant and 230 nm hole diameter (a) and (c)TE mode, (b) and (d) TM mode.

Figure 43 and Figure 44 show far field simulations for 785nm light, investigating the effect of hole size over the range 230nm to 350nm. We find that the angle of far field projection increases with hole size. However scattered intensity drops significantly with increased hole size, and above 300 nm the farfield profile is distorted so much from a sharp Gaussian peek, that it is no longer easy to distinguish the center of the projected beam, and so is unsuitable for simple readout system. Hence we can fine tune projection angle by adjusting the size of the holes.

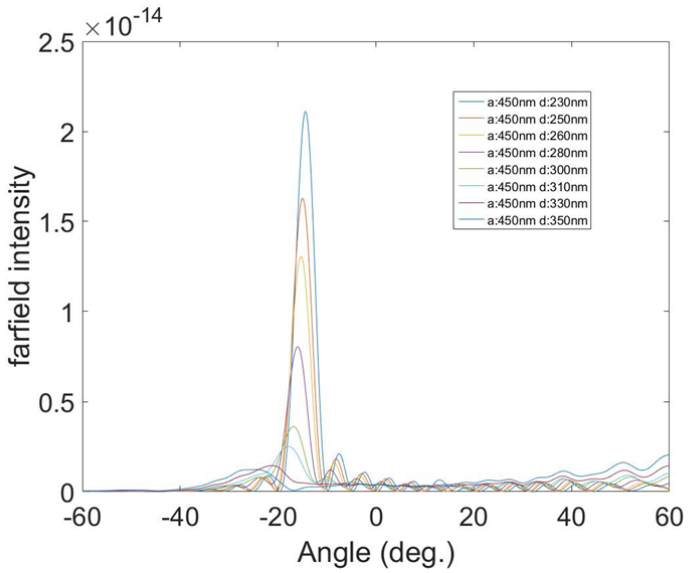

Figure 43. Hole size dependent FDTD farfield calculation for square lattice photonic crystal at 785 nm and TE polarization.

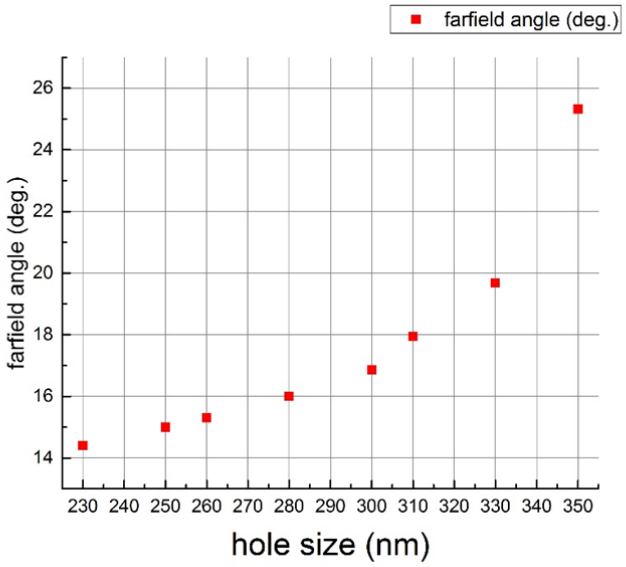

Figure 44. FDTD simulation results of far field projection angle with different hole size at 785nm with TE polarization.

Figure 45 shows an example cross section simulation of E-field distribution for an excessively large hole size of 330nm for both TE and TM polarizations. E-fields of both TE mode and TM mode are barely confined in the photonic crystal structures when propagating in the slab waveguide.

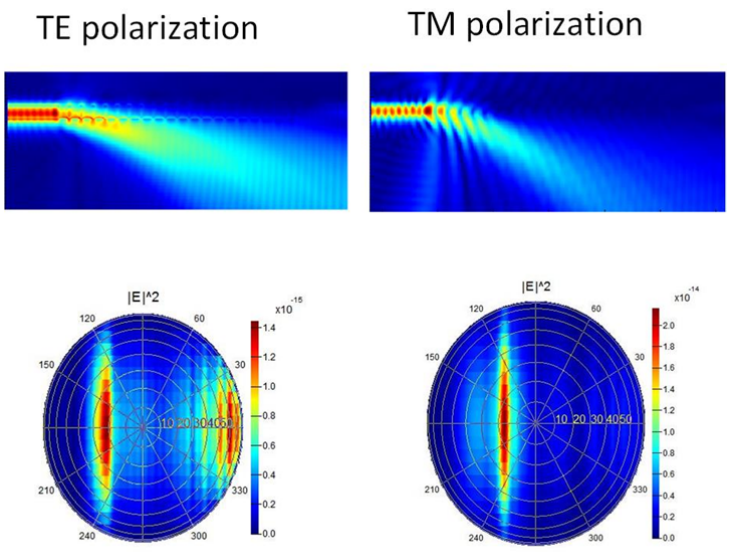

Figure 45. E-field cross section of fundamental mode propagating in PCs with hole diameter of 330nm and period of 450nm at 785 nm.

Wavelength dependent far field dispersion map provides more detailed information for sensor design. An example dispersion map for a sensor with 450 nm pitch and 230 nm holes size is shown in Figure 46. This was the operating condition for the generation one sensors, whose performance results are presented in chapters 7.

We also observed that there is a super-high intensity working point with a projection angle of 0 degree at 680nm. At this point two photonic crystal dispersion bands intersect with each other (this actually corresponds to the high symmetric Gamma point (Γ) point of the Brilloin zone). This optimal working point will result in maximum sensitivity response for the sensor. This will be discussed in detail in following chapters.

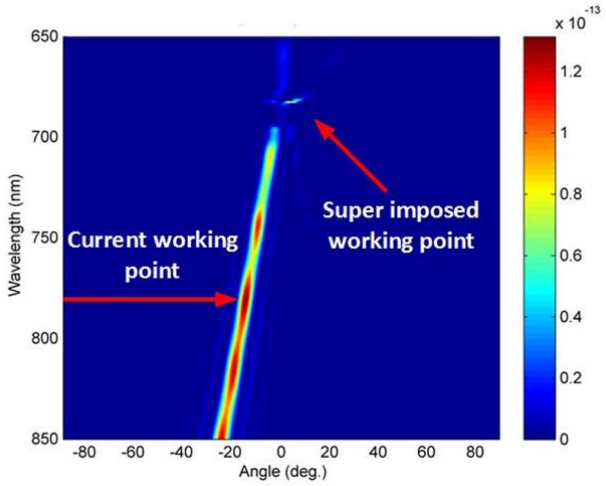

Figure 46 Far field projection with broad band source from PCs sensor (a: 450nm d:230nm).

6.1.2 3D RCWA modelling

3D Rigorous Coupled Wave Analysis (RCWA) simulation method was also used to investigate sensor performance and optimise design. RCWA simulates light incident at an angle to the slab waveguide from free space above the sensor giving information about in-coupling conditions. Since the sensor is a reciprocal device simulation data reveals out-coupling angles for the guided modes. RCWA simulations are cross-compared to the FDTD simulations. *Figure 47* shows this concept. Solid red arrows indicate the paths of light coupled by the photonic crystal structure from free space to the slab waveguide. Solid blue arrows indicate the path of light propagating from the left within the slab waveguide and coupled out to free space by the photonic crystal.

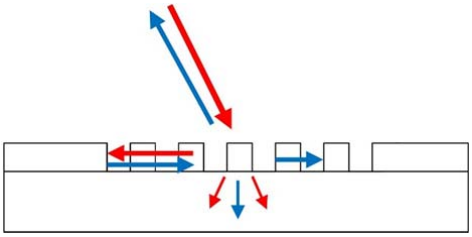

Figure 47. Coupling with a square lattice PCs sensor at a specific angle.

RCWA simulation data plotted as a full angular wavelength map is shown in Figure 48. As explained previously in chapters 3-4 this effectively plots the photonic crystal band structure for a single direction of propagation. For 785 nm wavelength we find a coupling angle of 14.6 ° arising from coupling to the fundamental dispersion band. The result shows agreement with FDTD calculation.

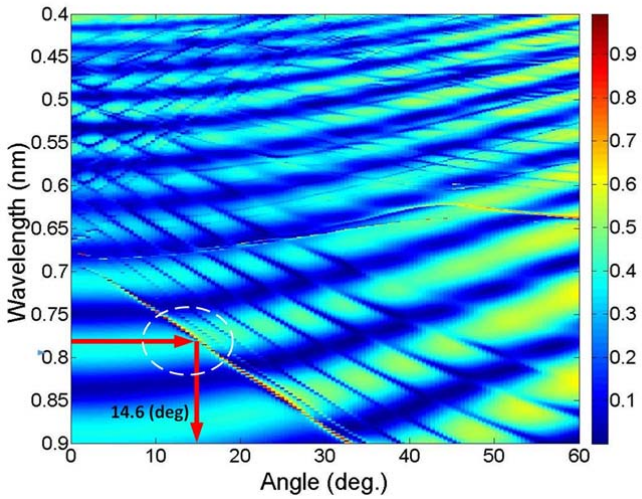

Figure 48. RCWA-calculated dispersion map for square lattice PCs sensor with period of 450 nm and holes size of 230 nm.

Using RCWA we now consider in more detail effects due to other geometric parameters such as etch depth e, buffer layer thickness, and again hole diameter on the coupling conditions (strength and angle).

Figure 49 shows RCWA simulation maps of coupling strength as function of angle of incidence and etch depth for 785nm incident light to a square photonic crystal coupler (a: 450nm, d:230nm). Colour scale relates to coupling strength. The sharp diagonal line corresponds to viable operating conditions. Clearly the coupling efficiency is higher when the etch depth is around 220nm, and becomes weaker until it reaches 400nm (the depth of the slab core t). The higher the coupling strength, the better the sensor performance.

This result suggest that molecular coatings on a shallow etched photonic crystal will degrade the out-coupling power. In addition the volume of the holes should be as big as possible in order to absorb more molecules in the sensing area (holes). Etch depth of 400nm is therefore preferred for the current design. It not only gives maximum coupling strength but also supports single mode at 785nm.

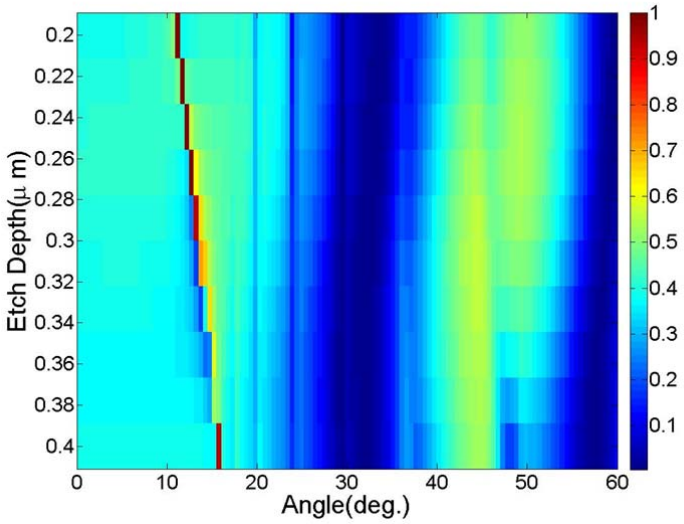

Figure 49. RCWA-calculated result of etch depth depended coupling condition calculation from square lattice photonic crystal (a:450nm, d:230 nm).

Ideally the sensor should couple light out in a single direction only as more than one projected spot will complicate the signal readout. *Figure 50* shows coupling conditions in relation to hole size. Coupling efficiency (indicated by colour scale) is highest for hole diameter between 225 nm to 300 nm. We note that a second coupling band appears when hole diameters is larger than 300 nm,

but with low coupling efficiency. As hole diameter increases both coupling bands become flat and coupling efficiency decreases.

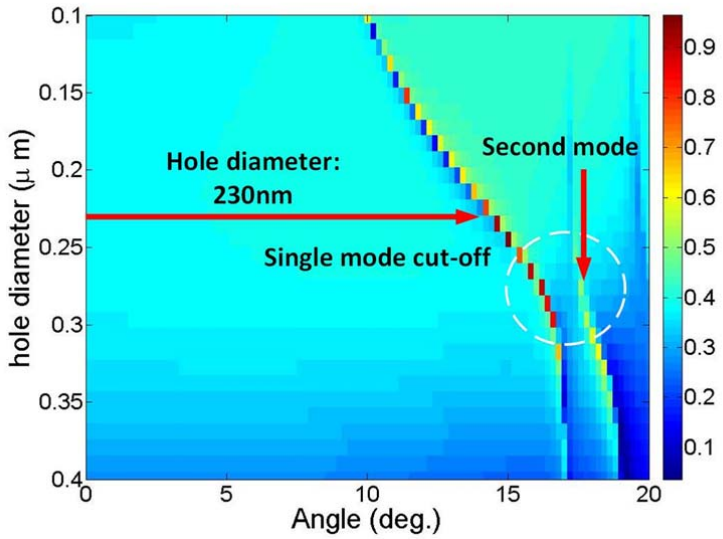

Figure 50.RCWA Simulation of effect of hole size on coupling conditions for square lattice photonic crystal (a:450nm, e:400 nm).

As previously shown in Figure 22, the SION waveguide core layer should be less than 600 nm thick in order to achieve single-mode at the operating wavelength of 785nm. Figure 51 shows calculated angle-resolved reflectance for the PCs sensor (a:450nm, d230nm) as a function of core thickness over the range 300nm to 1500nm. Multi-mode behaviour is observed above the single-mode cutoff line. A low gradient ($\Delta\boldsymbol{\theta}/\ \Delta t$) is observed for the first order dispersion band for core thickness larger than 1000nm making the device tolerant to thickness variation during fabrication process. Δt is the core thickness difference. However, the performance of the sensor will be poor as multimode / multi spot projection will occur.

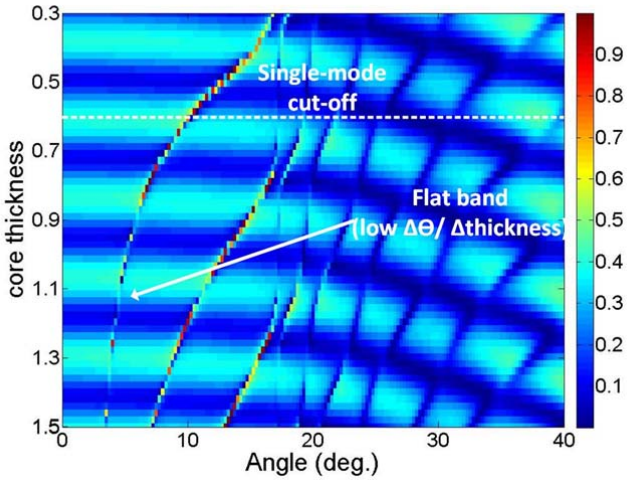

Figure 51. RCWA calculated zero-order angle-resolved reflectance for PCs (a: 450nm, d:230nm) at 785nm with variable core layer thickness.

The last parameter to optimise is the thickness of the SiO_2 Buffer layer. Figure 52 shows the angle-resolved specular (zero-order) reflectance of the PCs sensor (a: 450nm, d 230nm) for a range of SiO_2 buffer layer thickness. Fabry Perot fringes can be seen periodic with layer thickness. The important feature is the sharp continuous vertical line at 15 degrees. This shows that coupling angle is independent of buffer layer thickness, but coupling strength becomes weaker when the thickness goes below 1 µm due to increased coupling to the silicon substrate.

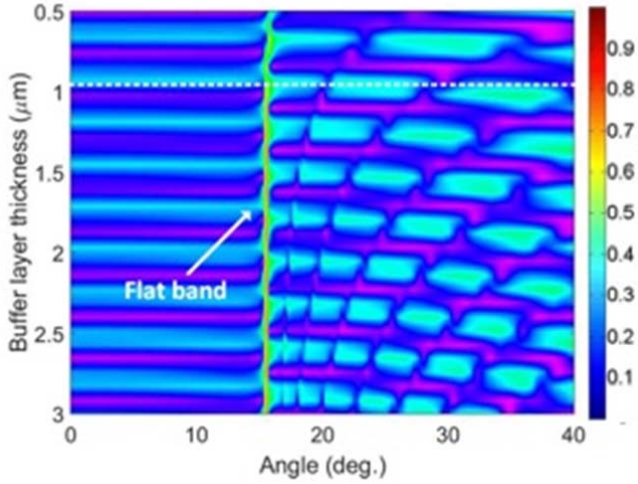

Figure 52. RCWA-calculated zero-order angle-resolved reflectance for PCs (a: 450nm, d:230nm) at 785nm with variable SiO_2 buffer layer thickness.

6.2 Sensor refractive index sensitivity performance

The sensitivity of the photonic crystal sensor is defined by how much projection angle changes per unit refractive index change (deg/RIU). The performance was physically simulated by filling holes with a different material. The sensitivity is expressed as:

$$S = \frac{\theta_{shift}}{\Delta n} \qquad 5.1$$

Where Δn is the refractive index difference in the PCs holes. As a simple first test to measure sensitivity performance, a 4% solution of PMMA diluted in toluene was applied to the surface. This changed the refractive index of the holes from 1 (air) to 1.487. Simulations were conducted by FDTD and RCWA methods. Figure 53 shows the RCWA calculated angle-resolved dispersion map for the PCs sensor (a: 450nm, d:230nm) before and after PMMA infiltration. After PMMA solution infiltration into the holes all dispersion bands shift slightly towards to longer wavelength and smaller coupling angles. Looking more closely we see that the first and second order bands show a significantly larger angular shift and coupling efficiency compared to high order bands, therefore we focus on the first two order bands.

Sensitivity can be derived from this dispersion map. The coupling angle at 785nm before and after PMMA infiltration is 14.6 ° and 11.87 °, respectively, giving a sensitivity of 5.64˚/RIU.

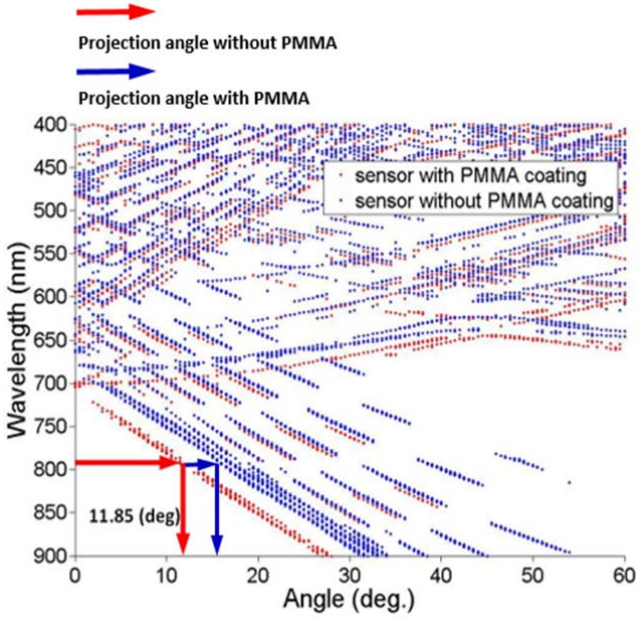

Figure 53. Bands extraction from RCWA calculation of PC sensor (a:450 nm, b:230 nm) . Blue cures represent the sensor baseline and red curves represent the sensor with PMMA.

Farfield projection angle was also calculated by FDTD method for comparison to the RCWA results as shown in Figure 54. This gives a sensitivity of 5.42 ◦/RIU, which is in good agreement with RCWA calculation and experiment result in chapter 7.

Sensitivity was simulated over range n=1 to 1.5 (step 0.017). Figure 55 shows the coupling angle shift as function of index change at 785 nm. We see that coupling angle moves linearly towards a smaller angle as index increases from 1 to 1.5. Out-coupling is strongest when the refractive index of the holes is low due to reduced mode confinement in the PC lattice as shown by FDTD the simulation inset to Figure 55.

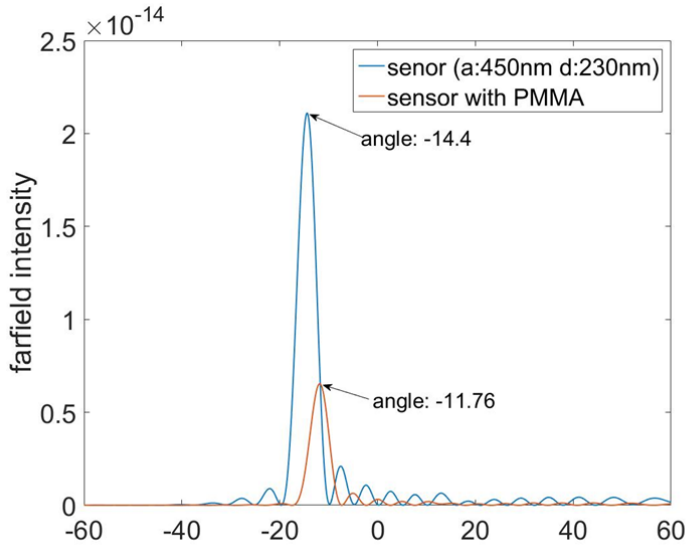

Figure 54. 3D FDTD far field calculation for sensor with period of 450nm and hole size of 230 nm. Blue curve shows the sensor baseline, red curve shows the projection angle after adding PMMA into sensor.

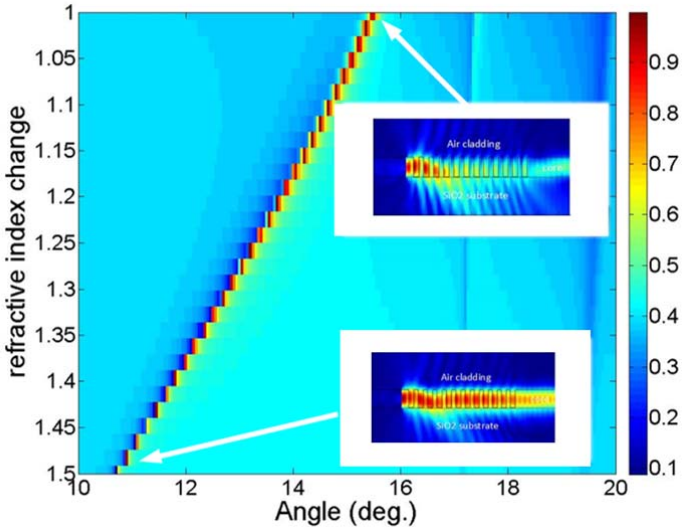

Figure 55. RCWA angle resolved specular reflection of PC sensor(a:450nm d:230nm) at 785 nm with different refractive index in the holes. The insets are the TE field cross section of PC with hole refractive index of 1 and 1.487 respectively.

6.3 Summary

In this chapter photonic crystal sensor based on RCWA and FDTD methods were described. The mechanism was explained in detail. FDTD method and RCWA method were used to investigate the projection angle shift by changing the refractive index in photonic crystal holes. Key parameters such as hole size, lattice constant, core thickness, buffer thickness and etch depth were analysed. Sensor performance was further explored by FDTD farfield calculations. It successfully demonstrated this projection sensing technology. The material of PMMA was used in order to introduce refractive index changes. The RCWA simulation result matched the result from FDTD far field calculation.

Chapter 7: Fabrication of monolithic sensor platform

By integrating a PC coupler and PC sensor on one platform we developed a promising label-free and multi-parameter biosensor based on the angle-resolved out-coupled mode analysis (AROMA) technology. Two-dimensional photonic crystals were applied to achieve monochromatic light (633nm/785nm) coupling, multi-channel formation and sensing functions simultaneously. Input coupler, slab waveguide and output coupler (sensor) consist of this integrated sensing platform.

The working principle of the coupler, and slab waveguide and photonic crystal design were explained. Sensors were first fabricated on Si substrate by using standard CMOS fabrication technology, whereby photonic crystals were etched into a silicon oxynitride (SION) thin film with refractive index 1.7 at 800nm. The initial tests on Si based devices show good agreement with 3D FDTD simulation and RCWA simulation. By using a handset readout to monitor the projected spot shift from the sensor functionalized by diluted PMMA, function test shows good agreement with FDTD and RCWA calculation. The schematic of sensing concept is shown in Figure 56.

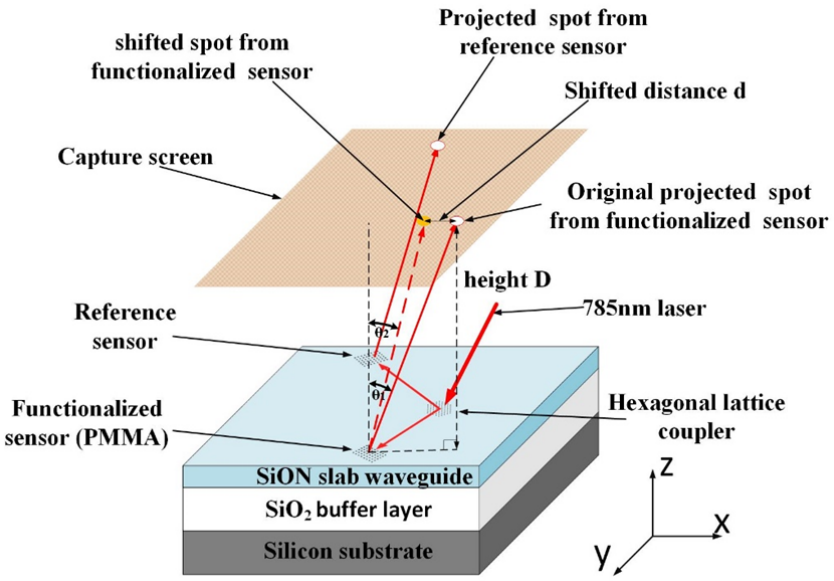

Figure 56 multi-parameter PC sensor concept based on AROMA technology

In order to make a fully functional sensor it is necessary to monolithically integrate the vertical coupler/ splitter described in chapter 3 with at least two PC sensors. The coupler lattice arrangement (square / hexagonal/ PQC) is chosen to create the required number of coupled beams for the number of sensor channels. The propagation direction in the slab waveguide of the coupled split beams depends on the lattice type, surface incidence angle and rotational direction. PC sensors must be positioned to intersect the path of each guided beam.

Generation one design (Figure 56**)** included a hexagonal lattice coupler and two square lattice sensors. One sensor acts as a reference for thermal drift cancellation and the other will be exposed to the target analyte for sensing purpose.

7.1 Layout design and fabrication process

7.1.1 Layout design and considerations

The chip layout was designed for 6 inch (150mm) wafers with a 20 mm edge exclusion zone. A sensor with period of 450nm and holes size of 230 nm was chosen for the generation one design as it provides strong coupling and good far field spot profile.

Chip layout for one coupler and two sensors is shown in Figure 57. Chip size is 30×15 mm, which is large enough for easy handling and small enough to create a reasonable number of chips on a 6 inch wafer. A few sets of chips with slightly different sensor hole size was created in order to adjust for fabrication process variation. In particular the PECVD SION film, had considerable uniformity variability.

For the hexagonal coupler, in-plane coupled beams are separated by 60˚, and two sensors were placed 11.5 mm radial distance from the coupler. Sensors were rotated in order to ensure that the guided beam is incident exactly along the $\Gamma - X$ direction, and perpendicular to the PC patch edge as shown in Figure 57. This prevents further beam splitting or diffraction at the sensor.

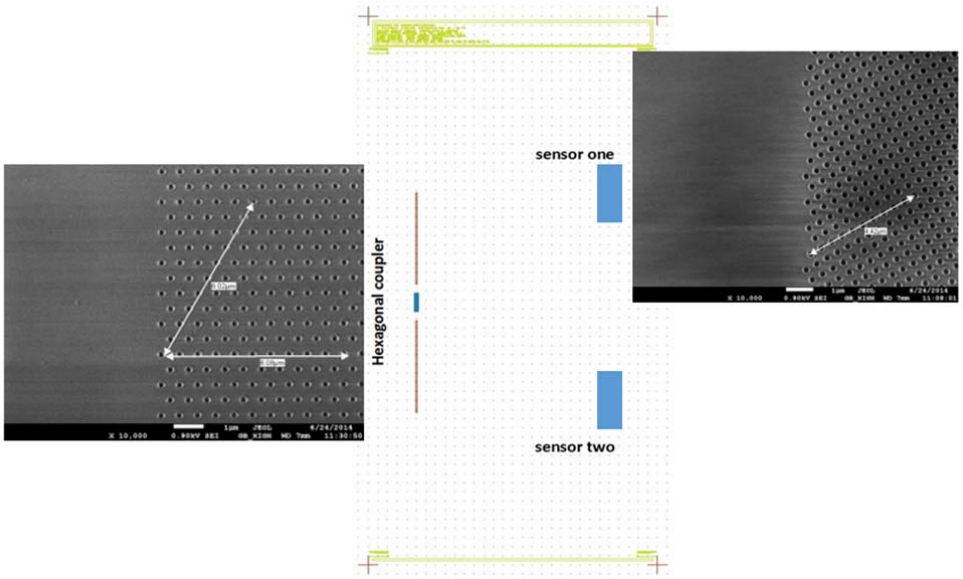

Figure 57. Mask layout of multi-path PC sensor. Insets are SEM image of hexagonal lattice coupler and square lattice sensor.

7.1.2 Fabrication process

Figure 58 shows the fabrication process flow for the PC sensor. 100mm single-side-polished (100) prime silicon wafers were cleaned by fuming nitric acid (FNA) followed by DI wafer rinse. A 2µm thick thermal oxide buffer layer was then grown by wet oxidation in a tube furnace at 1000˚C for 21 hrs.

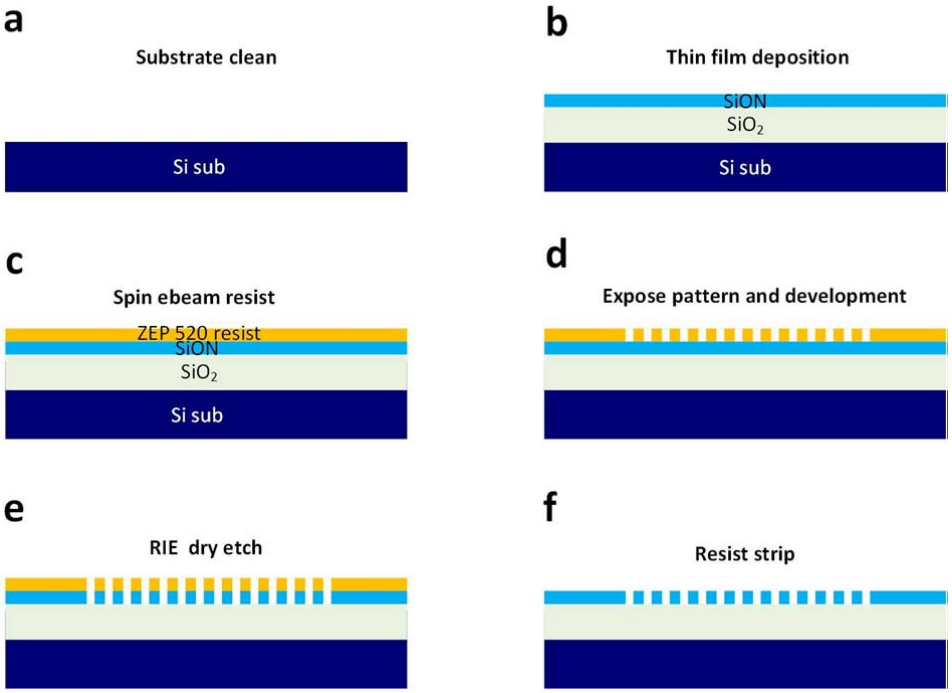

Figure 58. Fabrication process flow. a) substrate clean by FNA. b) SiO_2 grown in wet furnace and SiON thin film deposition by PECVD. c) Ebeam resist spin on wafer . d) pattern exposure and resist development. e) RIE dry etching of SiON layer through developed resist mask. f) strip resist by NMP or plasma asher.

Thickness variation of the SiO_2 layer across the 6 inch wafer is shown Figure 59, and was found to be about 10 nm on average (0.5%). The thickness was measured by CompleteEASE ellipsometry system.

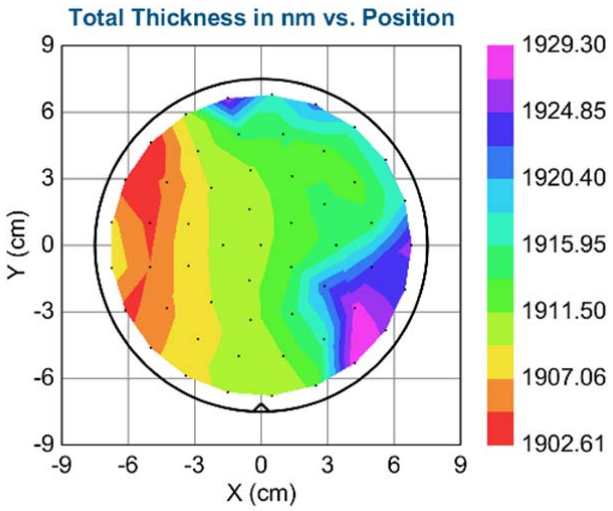

Figure 59. Thickness variation of SiO_2 layer grown by wet furnace tube (ellipsometry results)

A 400nm thick layer of silicon oxynitride (SiON, n = 1.7 at λ = 800nm) was subsequently deposited by plasma-enhanced chemical vapour deposition (PECVD, OPT PlasmaLab System 100) using the optimal parameters for low optical loss. In brief, these parameters were a gas mixture of 2% SiH_4 in N_2 plus additional NH_3 (20 sccm) and N_2O (210 sccm), with a total flow of 1230 sccm and chamber pressure of 750mT. The platen temperature was 350°C and the low-frequency (100kHz) 40W RF power gave a deposition rate of approximately 0.34nm/s. After deposition, wafers were annealed at 600 °C for 2 hours in an inert Ar atmosphere to further reduce the optical loss at λ = 633nm from 2 dB cm^{-1} to 0.2 dB cm^{-1} (measured by a metricon prism coupler system). As shown in Figure 60 the guided mode was clearly confined in the SION film. It also confirmed SiON thickness to be close to 400nm and mode effective index about 1.59 which is comparable with previous FDTD simulation. Uniformity is poor because of the deposition recipe. Only the centre area is in the target thickness range and can be used. Figure 60 b) shows the 633 nm laser successfully coupled into the SiON film and the guided mode is clear(red laser beam presents in the thin thilm). The incident 633 laser was coupled into the SiON film via a prism with a certain angle. If coupling is not successful there will be no guided beam in the film.

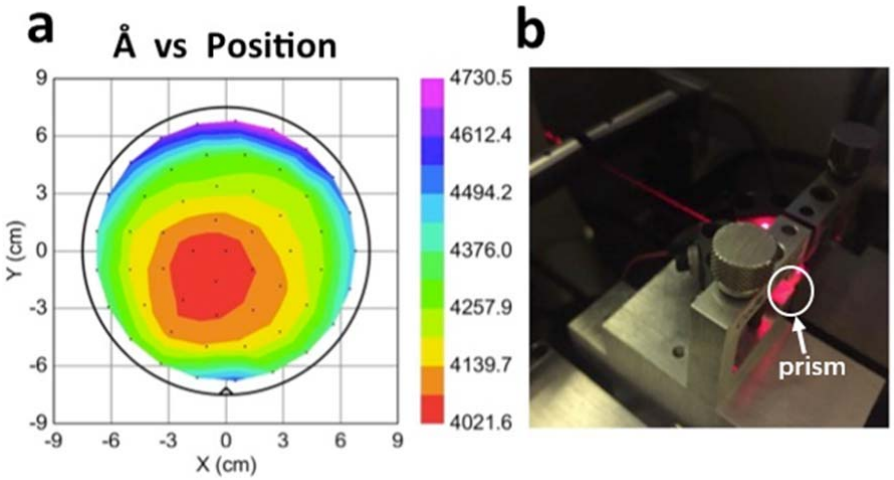

Figure 60. a) Ellipsometry thickness mapping of SiON layer b) Photograph showing successful coupling of a 633nm laser beam into a slab waveguide mode using a Metricon prism coupler system..

A 400nm thick film of ZEP520A resist was spun on the SiON/SiO_2-coated silicon substrate. Mask patterns were written in the resist by 100keV direct write e-beam lithography (JEOL JBX-9300FS) before being transferred to the SiON layer by RIE etching (OPT PlasmaLab 80+).

A cyclic etch process was used to minimize substrate heating and avoid resist degradation. This consisted of a 30 second etch with CHF_3/Ar (25/25sccm) and 200W RF (13.56MHz) power, followed by a 90s cooling step with pure N_2. The chamber pressure and temperature remained fixed at 30mT and 18 ˚C, respectively. Both steps were looped 32 times in order to etch holes down to the SiON/SiO_2 interface. The residual resist was stripped by an overnight soak in NMP and the wafers diced into individual chips shown in Figure 61. More detail information of fabrication process is in APPENDIX D.

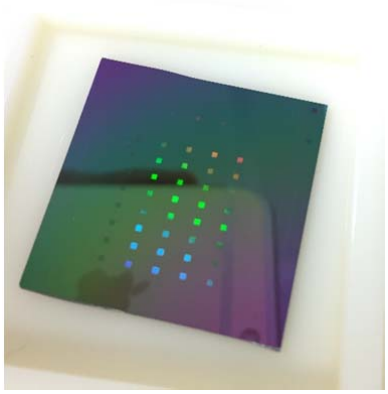

Figure 61. photograph of test chip after fabrication process

7.2 Function demonstration of integrated input coupling and output coupling

The coupling angle can be precisely measured by the reflectometry system, but a bespoke setup (Figure 62.) is required in order to rapidly test both input coupling and output coupling at the same time. This consists of a 785 nm PM-fiber pigtailed laser (A), a rotation mount (B), CMOS camera (C) and (I), iris aperture (D), 100mm plano-covex lens(E), beam deflecting mirror (F), bespoke chip mount and translation stage (G), and ball-joint mounted mirror. This setup allows a wide range of coupling angle by the deflection mirror and ball-joint mounted mirror (H). The 785 nm pigtail laser diode has a typical output power of 7.5mW at 47.5mA, the fiber of the laser diode is terminated with the fixed-focus collimator. Quick adjustment of coupling angle is permitted by the deflecting mirror and translation stage. The aperture is used to limit the angular cone of the beam from the collimator.

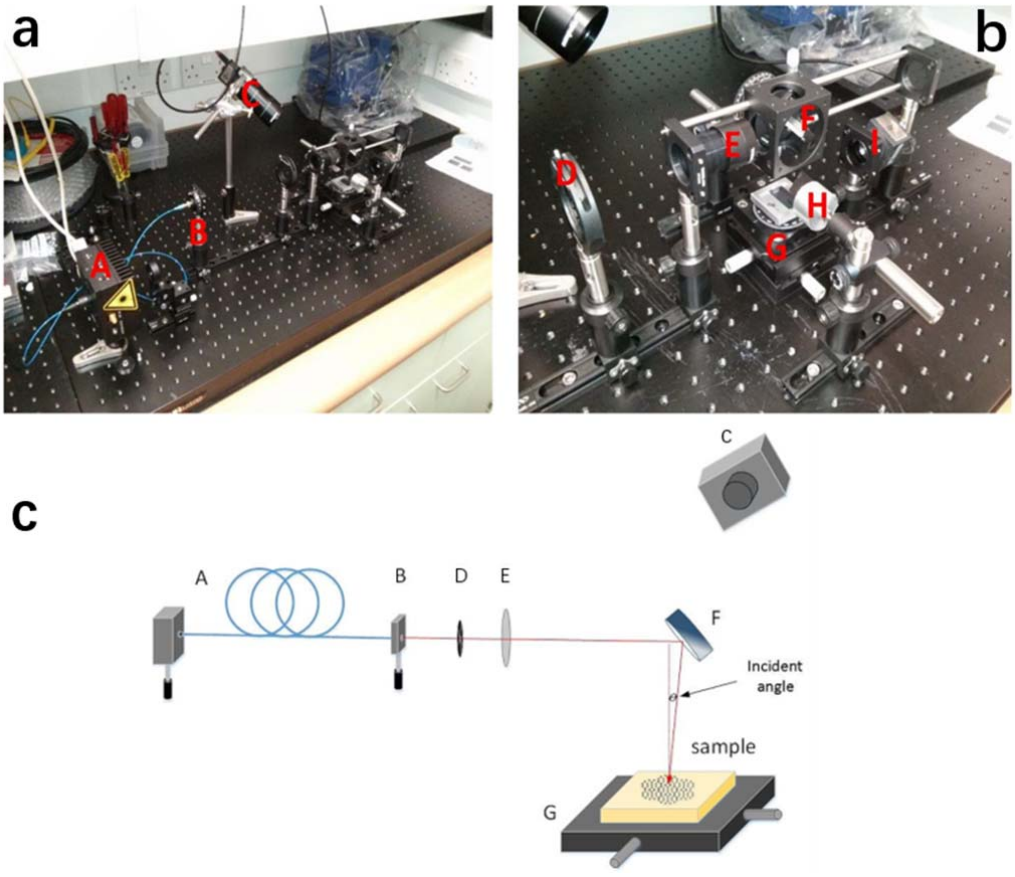

Figure 62. Image of rapid demonstrator setup, a) and b) real image of demonstration set up, c)schematic of the set up.

Figure 63 is a camera image of the generation one sensor device showing clear coupling of 785 nm light by the input coupler and splitting to two forward-propagating guided beams. The incoming light was coupled at a surface incidence angle of 4°. Sensor projection was shown by two spots projected onto a tissue screen placed about 2 cm above the chip.

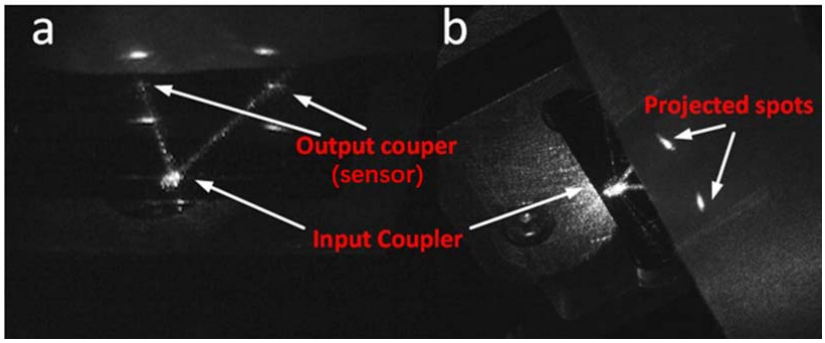

Figure 63. Basic functional testing on integrated hexagonal lattice input coupler and square lattice output coupler sample. a) side view, b) top view.

7.3 Summary for chapters 3 to 6

In chapters 3-6 design, optimisation, and fabrication of the vertical coupler / beam splitter and photonic crystal sensor were described and operation demonstrated.

Chapers 3 to 4:

SiON (n=1.7 at 800nm) was chosen for the slab waveguide core material grown on an SiO_2 layer ontop of a Si substrate. Guided mode profile and effective index were calculated by FDTD method.

Coupler design was derived using a reciprocal lattice space Ewald circle construction to optimise phase matching between incident light and photonic crystal Bragg peaks. A rigours RCWA model was then used to refine geometric parameters including holes diameter (d), polarization (p) and lattice constant (a) to optimise coupling angle and efficiency.

Chapter 5-6.

Sensor design was based on a square PC lattice, and was optimised using RCWA and FDTD methods. Experimental operation was demonstrated at 633 nm and 785 nm, in excellent agreement with theoretical calculations. A simple functional sensitivity test at 785 nm using dilute PMMA showed sensitivity of the generation one device to be 5.42 ◦/RIU.A fully monolithic sensor platform was fabricated and demonstrated to work.

Chapter 8: Sensor performance analysis and optimisation

To recap, the photonic crystal Angle Resolved Out coupled Mode Analysis (AROMA) sensor translates a small change in refractive index inside the holes of the photonic crystal to a large change in coupling wavelength for fixed incidence of angle, or a shift in projection angle for fixed wavelength. This removes the need for an external spectrometer since the PC plus CCD camera effectively constitutes a compact spectrometer. The Bloch mode guided by the PC interacts strongly with analytes placed inside the holes resulting in a small change in effective index of the guided Bloch mode. This change leads to an altered output-coupling angle causing the projected spot to shift on the CCD camera or a capture screen.

In Chapter 5 basic sensing performance was evaluated by FDTD simulation method for a single design by adding a large refractive index change 'analyte' (PMMA) to the holes. A series of small index change, was also investigated in order to evaluate the sensitivity.

In this chapter the intrinsic performance of the sensor is investigated in more detail. Two different methodologies are used to evaluate the sensitivity: a) angle resolved specular (zero order) reflection measurement, b) tracking the shifting distance of the projected spot respectively.

Several methods were investigated to enhance the sensitivity including: a) changing the operating point from small negative projection angle (negative detune) to vertical projection angle (Γ gamma point), b) making use of higher order photonic crystal dispersion bands (instead of 1^{st} band) , c) making use of a doubly degenerate 'super transition' dispersion point.

However, the most significant effect was achieved by changing the operation point. In this case it is possible to increase sensitivity above 6500 °/RIU for a small range of refractive index change.

8.1 Far field projection modelling by FDTD method

The effective index of guided modes relates to size and period of the etched holes in the PC sensor. When the holes size is increased, more analyte can infiltrate into the holes. Table 3 and Figure 64 shows how sensitivity changes as hole size increases for the case of 4% PMMA placed on the sensor area.

Table 3. Hole size dependent sensitivity according to 3D FDTD simulation.

Hole size	230nm	300nm	330nm	350nm
Sensitivity ◦/RIU	5.42	8.00	15.48	24.5

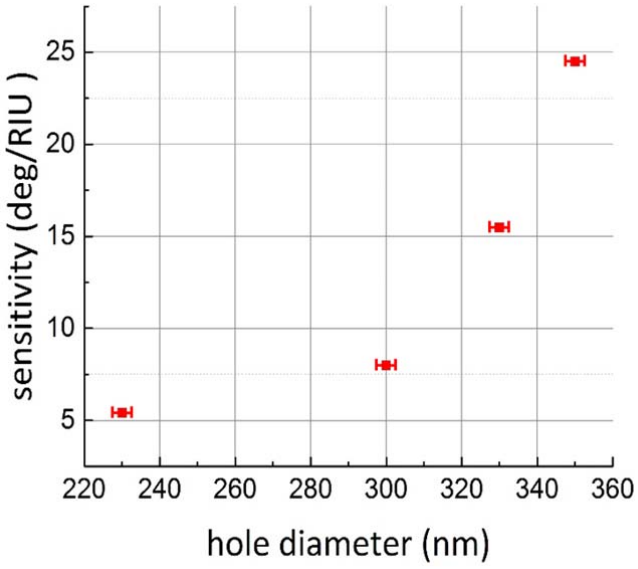

Figure 64. hole size vs sensitivity by FDTD simulation

The PC hole fill factor changes with hole size, resulting in tuning of effective index of the photonic crystal Bloch mode. According to the diffraction equation (we only consider the first order diffraction):

$$\sin\theta = \frac{\lambda|k-G|}{2\pi} \qquad 8.1$$

where θ is the polar projection angle from the PCs sensor, λ is the wavelength, k is the wave number of the PhCs mode and G is the reciprocal lattice of the PhCs structure. k can be estimated by:

$$k = \frac{2\pi}{\lambda}[n_{core} + f \times (n_{hole} - n_{core})] \qquad 8.2$$

Projection angle is governed by the differences between k and G. k is mainly affected by the fill factor f. The fill factor f of a square lattice is expressed as $(\frac{r}{a})^2$, where **r** is the radius of holes and a is the lattice constant of PCs. The fill factor changes exponentially with r resulting in decreasing k, hence projection angle will become more negative ($|\theta|$ become larger) before the analyte is added. Overall sensitivity increases with hole size.

8.2 Experimental sensitivity measurement by reflectometry

Sensitivity tests for sensors with several different hole size were conducted by adding 5 µl 4% diluted PMMA onto the surface of fabricated sensor devices. Clean sensors were first tested by spectroscopic reflectometry over an incidence angle ranging from 0° to 60° in order to accurately confirm their initial projection angle θ_1 for all wavelengths before the PMMA coating was applied. Projection angle after PMMA application θ_2 was then measured again by reflectometry. (note spectroscopic reflectometry actually maps coupling as function of incidence angle for a wide range of wavelengths. This corresponds to the projection angle since sensors are reciprocal devices).

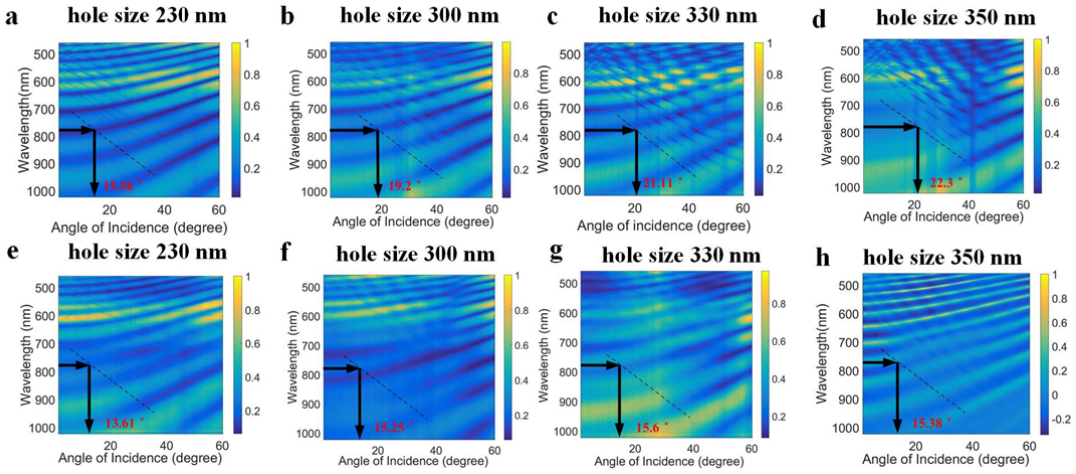

Figure 65. Angle resolved dispersion maps (reflectometry measurement) of sensors with different holes size. Original coupling angle : a (hole size 230nm), b(hole size 300nm) ,c(hole size 330nm) ,d(hole size 350nm). After PMMA coating: e(hole size 230nm), f(hole size 300nm), g(hole size 330nm) and h (hole size 350nm).

Angle resolved specular reflection maps before and after PMMA coating are shown in Figure 65. Output coupling angle is extracted from the point of intersection of a horizontal 785nm line with the fundamental dispersion band (black dashed line) as indicated by the arrows on each diagram. The resultant sensitivity is shown in table 4 and plotted in Figure 66. We find that 350nm hole size gives best sensitivity.

Table 4. calculation result from reflectometry measurement between and after coating with diluted PMMA.

Hole size	230 nm	300 nm	330 nm	350 nm
Before PMMA	15.36°	19.2 °	21.11 °	22.3°
After PMMA	13.61 °	15.25°	15.6°	15.38°
Angle shift	1.75 °	3.95 °	5.51 °	6.92 °
Sensitivity °/RIU	3.61	8.5	11.36	14.88

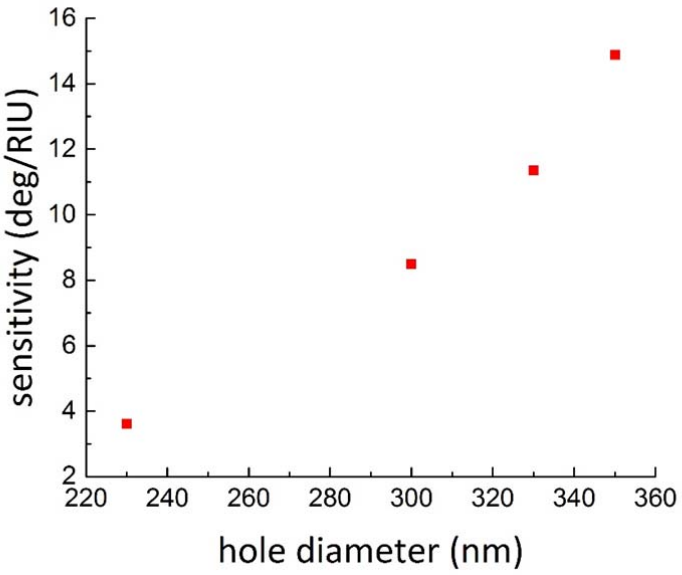

Figure 66. Calculated sensitivity from experimental data of reflectometry measurement.

8.3 Experimental sensitivity measurement by tracking projected spot above PCs sensor

The initial coupling angle for a set of sensors with a range of hole size were measured by reflectometry as explained in the previous section. These provide a key reference for the projected spot tracking readout mechanism, in order to calculate the sensitivity through spot shift. In this case an image is simply captured on a camera before and after application of PMMA solution. Figure 67 shows a schematic of the projected spot tracking system. The spots are projected on to a matte screen positioned 2 cm above the chip. After application of PMMA we see

projected spot movement of 1mm according to the grid mark on the matte screen in Figure 67 a) and b) (for clarity the original spot is highlighted in Figure 67 b) with green marker).

According to the geometry of the setup Figure 67 c), projected spot shift after application of PMMA, is given by equation 8.3 where θ_1 is the clean the original projection angle evaluated by reflectometer, and θ_2 shifted projection angle:

$$\theta_2 = \arctan\left((\tan(\theta_1) \times D) - d\right)/D) \qquad 8.3$$

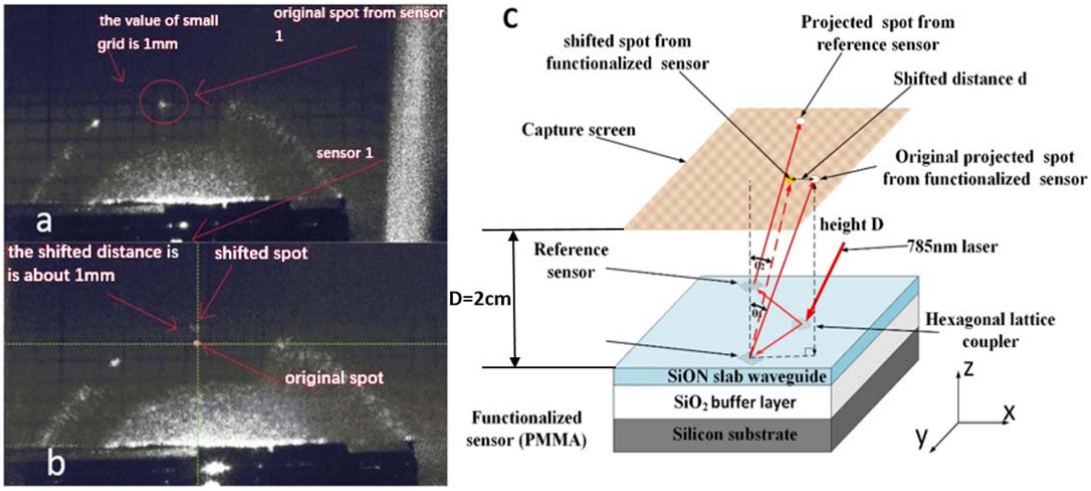

Figure 67. Camera based projected spot tracking system. a) original projected spot recorded by camera. b) shifted projected spot after PMMA resist coating. c) schematic of projected spot tracking mechanism.

Sensitivity is then given by

$$S = (\theta_1 - \theta_2)/\Delta n \qquad 8.4$$

Table 5 shows the calculated sensitivity measured by spot shift method. It shows very good agreement with the reflectometry result.

Table 5. Holes size dependent sensitivity from spot tracking readout system.

hole size	230 nm	300 nm	330 nm	350 nm
sensitivity°/RIU	5.51	8.00	13.19	14.9

8.4 Angular transition point with large holes

Enlarging holes size gradually improves the sensitivity of PCs sensor at the cost of wider spot size. When the hole size is large enough, there will be a transition occurring at a particular index range. In this section FDTD simulations were conducted for two sensors with 230nm and 400nm hole diameters at a wavelength of 785 nm. The hole index varies from 1 to 1.1 in 0.002 increments. The peak position of far field projection was extracted from each simulation data in order to determine the angular predicted change.

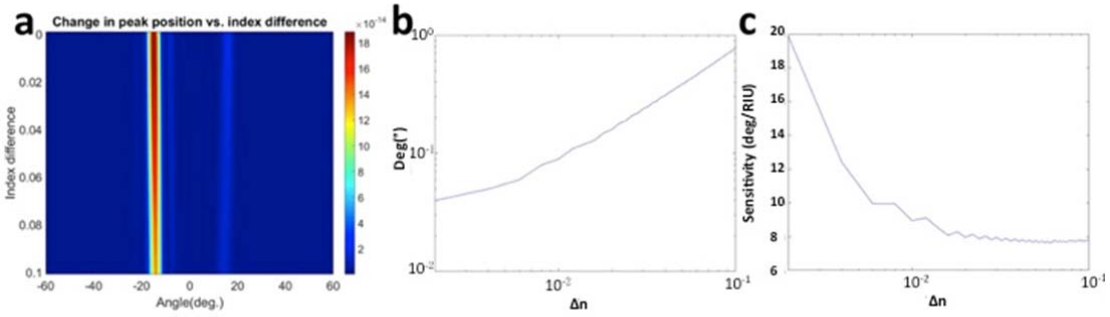

Figure 68. FDTD simulation of Sensitivity investigation for sensor with 450nm period and 230 nm holes diameter. a) far field projection with increments index value of 0.002. b) Angular shift vs refractive index change, c) sensitivity vs refractive index change.

Figure 68 shows the angular shift and sensitivity response of sensor with lattice constant of 450 nm and holes diameter of 230 nm. We can observe that a non-linear response with relative small index change (Δn <0.01). The maximum sensitivity is below 20 °/RIU. The sensitivity reached above 8°/RIU at Δn =0.1.

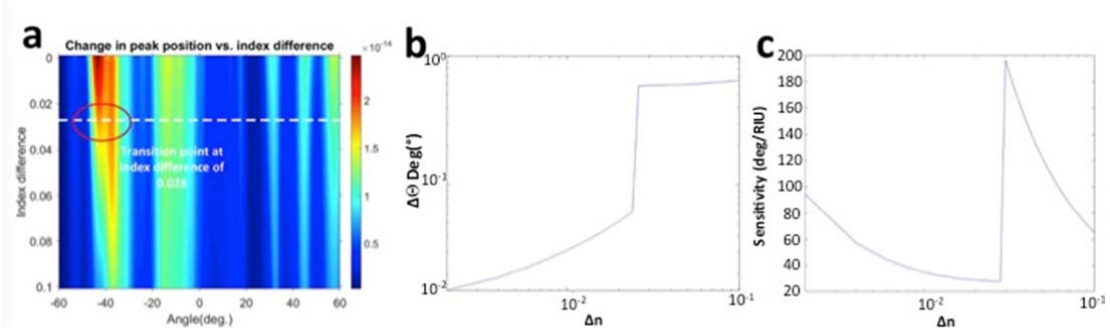

Figure 69. Sensitivity FDTD investigation for sensor with 450nm period and 400 nm holes diameter. a) far field projection with increments index value of 0.002. b) Angular shift vs refractive index change, c) sensitivity vs refractive index change.

The sensor with enlarged hole of 400nm shows an abnormally sharp rise in sensitivity close to 200˚/RIU (*Figure 69*). This transition point is highlighted in Figure 69 a). The discontinuity happens for refractive index change of 0.028. It turns out that under these conditions there are two out coupled spots and the peak switches from one to the other creating the discontinuity in the graph. Comparing back to the other sensor (a:450nm d:230nm) we find that the resonance is not narrow any more. The initial farfield peak (coupling angle with Δn = 0) increased to 42˚ corresponding to a sensitivity larger than 60˚/RIU for Δn = 0.1.

Farfield pattern for large holes was not further investigated due to the weak confinement, and difficulty in discerning the farfield peek (Figure 70). Enlarging holes is therefore not the best option to use in order to increase sensitivity.

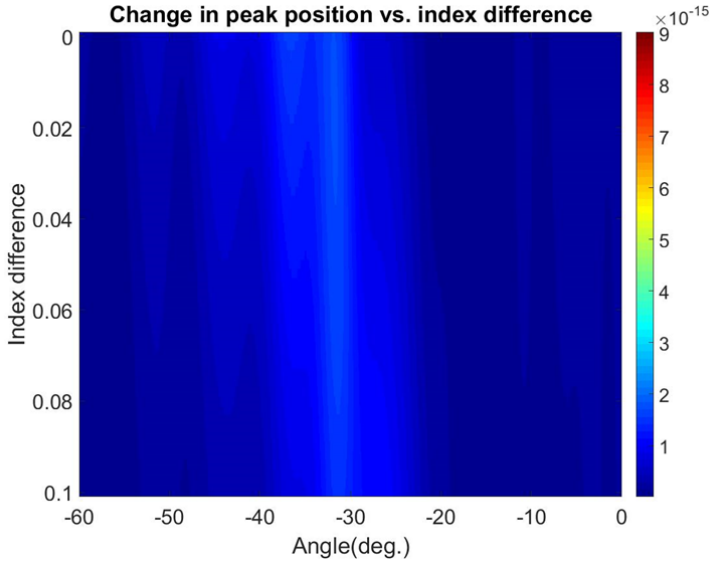

Figure 70. FDTD simulation of TE mode Far field projection with increments index value of 0.002 for holes diameter of 400 nm.

8.5 Shifting operation point to Γ

Sensitivity improvement by enlarging the holes size was demonstrated by both simulations and experiments and a viable range limit determined.

So far all demonstration sensors were 'negative detuned' , working by coupling to the linear 1st order Photonic Crystal dispersion band. An operating wavelength of 785 nm was chosen, and a strong resonance shown at this wavelength. Under these conditions projection angle varies linearly with wavelength (following the gradient of the photonic crystal dispersion band). However, the linear trend was terminated by an crossing with anther flat photonic crystals band,

as shown in Figure 71. This flat band is expected to be much more sensitive to the environmental change. This indicates a small in-plane guided mode changing leads to a relative larger output angular change. It is noticeable that this operating point corresponds to the lattice high symmetry point (Γ point) at a wavelength of 683nm. Ideally for our purpose this working point should shift from 683nm to 785 nm. This can be achieved simply by scaling the lattice constant and hole size following the be the photonic crystal scaling law.

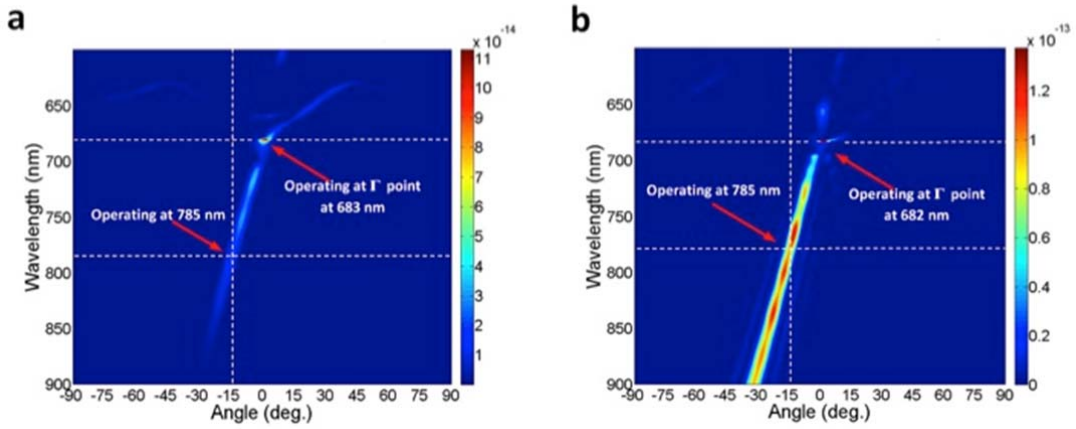

Figure 71. Far field projection of standard sensor (a: 450nm d:230nm) with different polarization. a) TE mode, b) TM mode.

The scaling factor from 683 nm to 785 nm is ~1.15. This results in a period of 517nm and hole diameter of 264 nm. Optimising the design around this starting point, vertical out-coupled light at 785 nm finally was achieved for a period of 523nm and hole diameter of 268 nm.

Figure 72 shows that the dispersion band curvature becomes extremely flat at 785 nm, and it operates with vertical projection at the Γ high symmetry point on the Brillouin zone. However, this high sensitivity is at the cost of a reduced refractive index sensing range and tight fabrication tolerance.

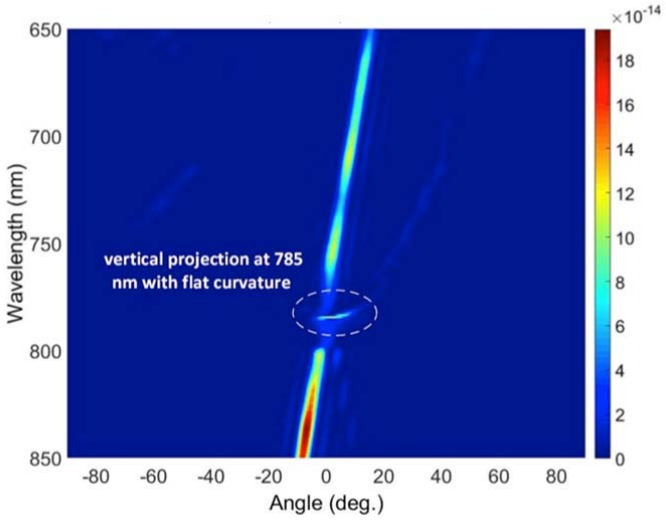

Figure 72. Far field projection of optimized sensor (a: 523 nm d: 264 nm) for 785 nm (TM)

Under these conditions we expect that an extremely small refractive index change (order of 10^{-4}) will result in a large detectable change in projection angle. To check this idea this sensor response was simulated for a large range of refractive index change by FDTD method (Figure 73).

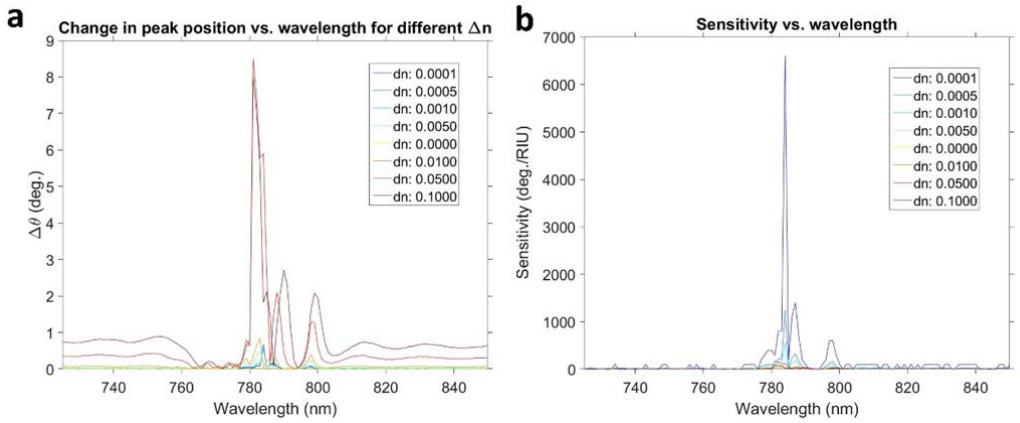

Figure 73. Angular deflection and sensitivity of square lattice sensor with a:523nm d:264nm. a) angular deflection vs wavelength and b) sensitivity vs wavelength.

Extreme high sensitivity was achieved at the Γ point for wavelength around 785nm, an angular deflection angle of 0.65 $^\circ$ was observed for $\Delta n=1\times10^{-4}$ from Figure 73 a). The calculated sensitivity ($\Delta\theta/\Delta n$) is shown in Figure 73 b. A sensitivity of 6500°/RIU was achieved for $\Delta n=1\times10^{-4}$. However, the highest sensitivity was achieved at the cost of extremely tight wavelength tolerance and structural parameters.

8.6 Summary

In this chapter PCs sensor performance was investigated by FDTD method. The angular shifts of far field projection for different PC hole sizes were calculated. The result shows that the sensitivity is increased when enlarging the hole size. However, this improvement is at the cost of weaker signal and poor beam confinement. Experimentally the sensor performance was investigated by reflectometry system and bespoke projection spot tracking setup.

Table 6. Advantages and disadvantages of PCs sensor:

Pros	Cons
• Simple coupler design for Monochromatic laser source • PCs coupler and sensors are fabricated with single Mask design. • Simple and cheap readout system (spectrometer free) • Novel sensing mechanism comparing with cavity resonance sensing and waveguide/fibre/prism based surface plasm resonance sensing. • Sensor performance is less affected by the fabrication variation or imperfection. The longer wavelength, the larger feature size is used. This relaxes the fabrication tolerance particular the etching process. • Relative measurement, one reference spot and several sensing spots. The absolute position of individual spot is not a issue. • Low power (4 mW) is enough saturate CMOS camera • Capability of multi-parameter sensing	• The most sensitive design (Γ point operation) requires perfect fabrication and very narrow laser linewidth. • The longer projection distance, the higher detection limit can be achieved. However, this reduces the compactness. • Sensor with silicon substrate is not possible to detect liquid target. It will distort the profile of project spot because of the non-flat surface.

The results are comparable with simulation. Furthermore, extreme high sensitivity was simulated and achieved by changing the sensor working condition into Γ point. A summary of the pros and cons of PC sensor is shown in table 6.

Chapter 9: Detecting monolayer molecules with photonic crystal structure based on guided resonance analysis

High sensitivity and selectivity to a molecularly thin layer is a key requirement for the bio-sensing applications. Molecular interaction normally occurs sequentially, layer by layer. For example, the detection of specific nucleic acid sequences, a typical double strand DNA binding process, includes formation of a cross-linker layer, binding of thiol-modified probe DNA and finally attaching the complementary DNA. It is crucial to monitor the binding process for each binding step. Different optical sensor configurations have been developed to sense this biomolecule binding process such as Mach-Zehnder interferometers (MZI), grating waveguide structures, optical ring resonators and photonic crystals[20][56][152][153]. Most of these approaches interrogate via the evanescent field from the waveguide mode. The attachment of molecular probes onto the surface of the waveguide changes the optical mode via the evanescent field. The main limitation of this approach is that the interaction between the probe molecules and waveguide is very limited i.e. only on the waveguide surface. This exponentially decayed field extends into surrounding environment by only ten to hundred nanometres and as such most of the energy of the waveguide mode does not interact with the molecular probes[144][154]. In addition some methods like SPR require heavy metals (gold), which increases the cost[155].

In this chapter a series of thin ZnO coatings are experimentally deposited onto this 2-dimensional photonic crystal sensor [156] in order to simulate a thin molecular layer. Atomic Layer Deposition (ALD) was employed as it provides sub nm precision conformal layer deposition, allowing calibration of the sensor response with very thin layers. These sub nanometre layers show a detectible spectral response, in agreement with RCWA calculations. To further validate this result, another experiment was conducted by forming a self-assembled monolayer (p-tolyltrichlorosilane) on the sensor surface. The shifted spectrum was in agreement with computer simulation. We also found that the sensor performance was enhanced by using the flat photonic crystal band observed from angle resolved dispersion map of photonic crystal structures.

The final part of this chapter employs the photonic crystal sensor to detect a deoxyribonucleic acid (DNA) hybridization process. The sequence of DNA strands is used for identifying BRCA mutation (Breast Cancer).

9.1 Sensor calibration

The geometry of the SiON slab waveguide without and with two-dimensional photonic crystals is shown in Figure 74 a) and b). The sensor consists of a SiON core layer, SiO_2 buffer layer and Si substrate. A two dimensional photonic crystal with square lattice structure was etched into the SiON core layer. The incident light beam will be deflected into different order diffracted beams when it interacts with periodic structures. These photonic crystal holes are integrated in a high refractive index slab waveguide layer, this core layer will support a discrete guided mode. Once the wave vector from the diffracted mode matches the guided mode, there will be a coupling. This will result in guided mode resonance and display intensity dips in the spectra of the zero-order reflection. Figure 74 (c) shows the reflection spectrum of the SiON slab waveguide and *Figure 74* (d) shows the reflection spectrum of photonic crystal SiON slab waveguide, there are clearly sharp intensity differences in the spectra and this corresponds to the guided mode resonance. *Figure 74* (e) looks in more detail at one of these resonances and shows the wavelength shift before and after thin layer material coating.

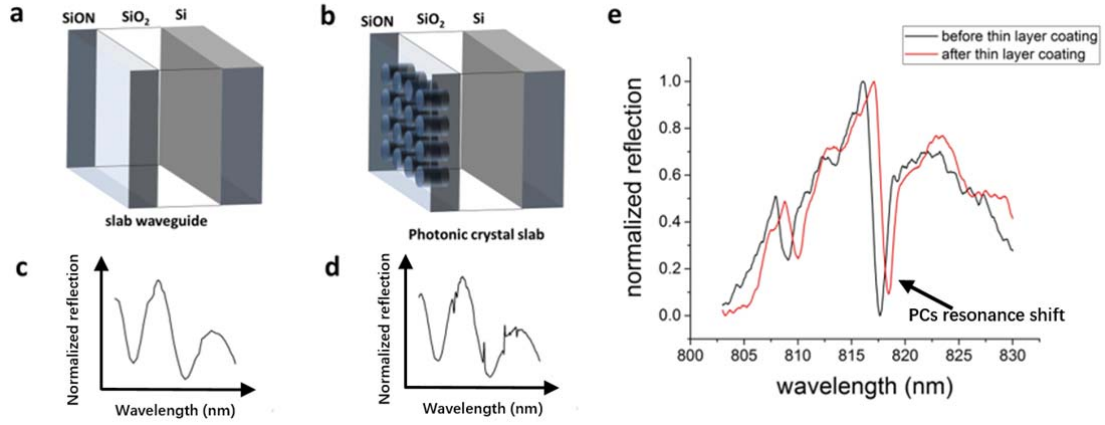

Figure 74. (a) SiON slab waveguide, (b) SiON slab waveguide with photonic crystal, (c) reflection spectrum from SiON slab waveguide, (d) reflection spectrum from photonic crystal slab waveguide,(e) resonance shift by attaching thin layer molecule.

This resonance is very sensitive to refractive index change of the surroundings and surface changes. When the photonic crystal area is coated with thin layer molecules, the coupled mode effective index will be altered. This coating process at the same time will increase the interaction area between molecules and guided light. Changes in the discrete guided mode in the waveguide will shift the resonant frequency and result in a shift in the observed wavelength of this coupling. Hence, coupling angular shift and wavelength shift of the resonance features of the photonic

crystal structure can be used to monitor the environment changes. Analysis of the angle resolved zero-order reflectance is required in order to investigate the guided resonance for use in sensing. The first two photonic crystal bands (from longer wavelength to shorter wavelength) are chosen for further investigation.

9.1.1 ZnO calibration curve

In order to evaluate the ability to detect a monolayer of material, ZnO was deposited on the sensor area by a FlexRay plasma Atomic Layer Deposition (ALD) tool. ZnO was chosen as it was available and it was a well understood and developed process on the ALD tool. The thickness of deposition was precise down to single nanometre and a conformal coating can be achieved. A series of depositions were conducted on a photonic crystal sensor (period: 528nm, holes size: 230nm, this parameter results in Γ point coupling) with 1 nm increments. After each deposition the reflectometry system was used to collect the signal of zero order reflectance. Incident laser was directed to the sensor with near normal angle (near 0˚). Figure 75 a) shows the dispersion map of photonic crystal sensor measured from this reflectometry system and linear response is clearly visible. Reflectance spectra of the first and second band with 0.5˚ incident angle is shown in Figure 75 c) and d) respectively. The fundamental band (first band) and second band were chosen to compare their sensitivity to surrounding changes. The wavelength shift of these features in both bands are plotted in Figure 75 b).

This result was also verified by modelling via rigorous coupled wave analysis. The RCWA 3D model was subtly different from the model of chapter 5. The surface, bottom and side walls, of the holes are coated with a very thin layer instead of changing the bulk refractive index within the holes. The result is shown in Figure 76 and uses the parameters from the ZnO deposition experiment.

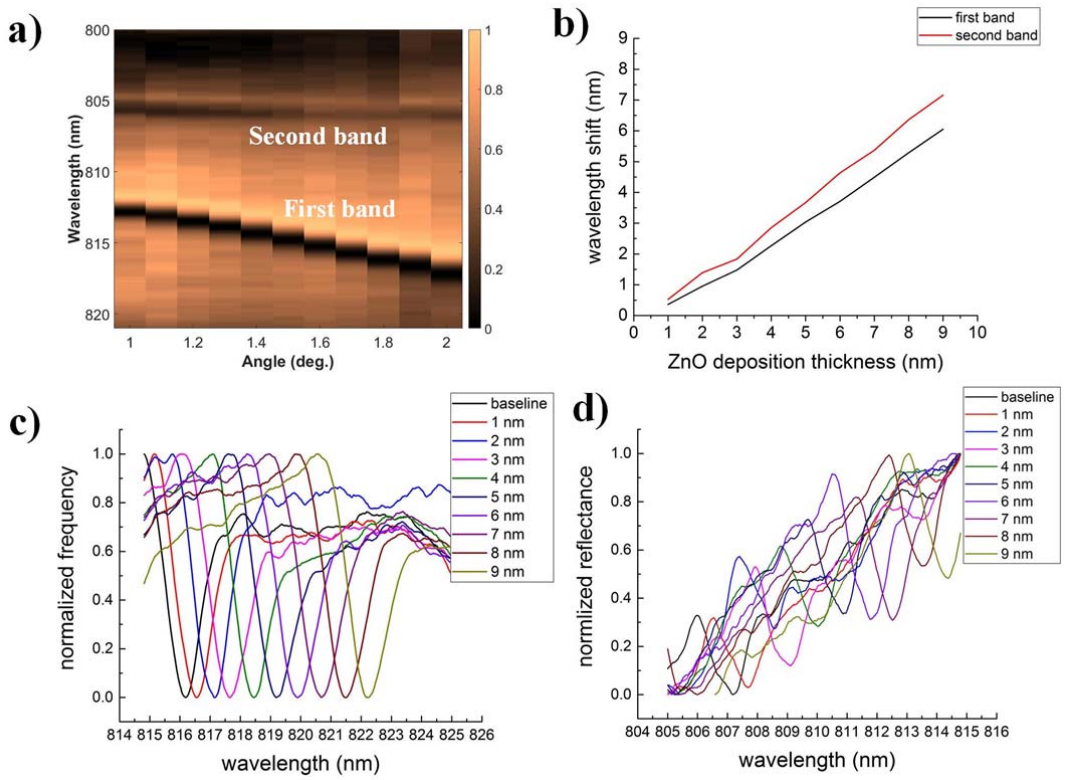

Figure 75. Resonance shift according to different ZnO thickness. a) zero order angle-resolved reflectance. b) Experimental data of guided resonant wavelength shift versus deposited ZnO thickness c) first band response d) second band response.

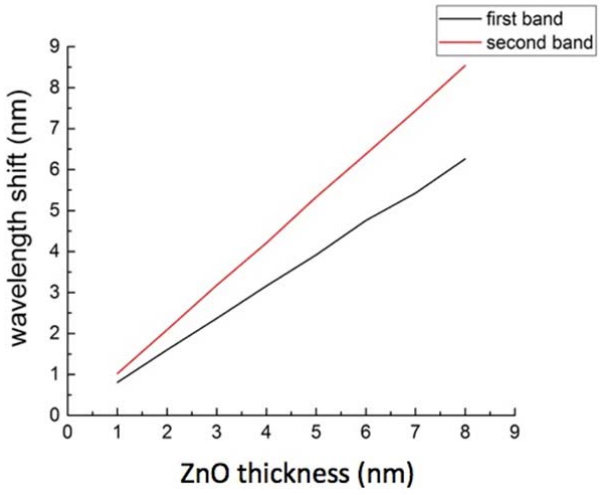

Figure 76. Numerical calculation by Rigorous Coupled Wave Analysis of PCs sensor with varying ZnO layer thickness.

In both the experimental and simulation data the resonances from the first two bands show a wavelength shift towards lower frequencies when the thickness of ZnO is increased. The spectral response shows a linear wavelength shift trend for the photonic crystal bands. In addition the resonance from the second photonic crystal band performs a greater shift compared with the first band resonance. Therefore, this resonance is more sensitive to surroundings. This is because the second band's group velocity is tending towards zero ($\frac{d\omega}{dk}$), i.e. the band is flat as observed from the angle resolved dispersion map in Figure 75 (a). This results a large change in the k-vector for a small change in frequency. The k-vector of the in-plane coupled mode dictates the wavelength of the guided mode resonance and therefore a large change corresponds to a large wavelength shift. We also notice that the wavelength shift of first deposition is smaller than the subsequent depositions. We believe this first layer was thinner (<1nm) due to seeding of the SiON surface and has been noted on previous investigations with ALD. If we neglect the deposition of the first ZnO layer the experimentally derived sensitivity (wavelength shift per nm of ZnO) is 0.71nm/nm and 0.81nm/nm for the first and second band respectively. In comparison, the numerical simulations show a sensitivity of 0.79nm/nm and 1.1nm/nm. The sensitivity of the experimental and modelled data slightly differs and this is likely to have arisen from the assumed refractive index of deposited ZnO layer, which was taken from the literature. However, it is interesting to note that the disagreement is much greater for the second band which may indicate a difference between the group velocity of the model and the real system.

The measurement error was also investigated for this experiment. Between each successive ZnO deposition the sample needs to be removed from the deposition chamber and mounted in the reflectometer system for measurement. In order to check the measurement uncertainty or repeatability the sample was measured 10 times, after each measurement the device was removed from system and remounted before the measurement was repeated. Figure 77 shows these repeated measurements and provides a standard error of ~50pm. This error suggests that with this system and measurement scheme we are able to resolve a ZnO thickness change of ~60pm.

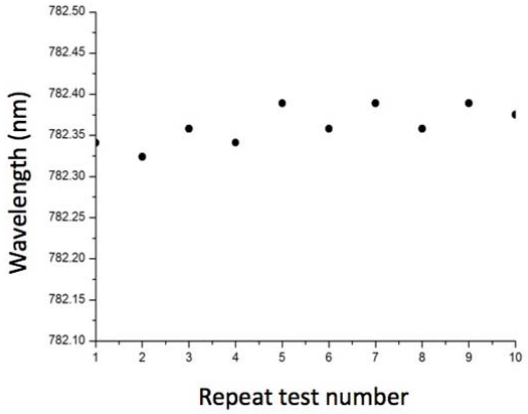

Figure 77. Measurement error of reflectometry measurement

9.1.2 Detection of self-assembled monolayer molecule coating (preparation of p-tolyltrichlorosilane was done by ZiLong Wang)

In addition to the ZnO calibration experiment, another sensor with a period of 540nm and hole size 230nm was used to observe the response of a self-assembled monolayer (SAM) of p-tolyltrichlorosilane (TTCS). This experiment was conducted to test the sensor in a real, albeit well understood chemical sensing environment. The sensor chip was first chemically cleaned with acetone, IPA and a large quantity of deionised (DI) water, and then dried by a nitrogen gun. The cleaned sample was immediately put into the plasma asher with a plasma power of 100 W and O_2 flow of 600 µL/min for 2 mins. This process hydroxylated the sample surface by generating –OH groups and the resulting surface was hydrophilic [157].

The use of the N_2 filled glove box is necessary to control water exposure, as p-tolyltrichlorosilane (TTCS) reacts violently with water, and the amount of water in the immersion solution has a significant role in the monolayer assembly process[158]. 125 µL of 97% TTCS solvent (from Sigma Aldrich) was added twice by pipette into 12.5 mL of anhydrous 99.8% toluene (from Sigma-Aldrich), resulting in a concentration of 2% in a range that agreed with the literature [159]. The sample was immersed in the solution at room temperature over-weekend. The variation in concentration as well as immersion time have been found not to affect the resultant TTCS SAM [159][160]. After the immersion, the sample was rinsed with toluene, then removed from the N_2 filled glove box and rinsed with acetone and IPA to remove any loosely attached residue.

Contact angle measurements were used to determine whether a TTCS SAM had been formed on the sample surface. Through measuring the contact angle of a droplet of water on the target surface, the hydrophobicity of the surface can be determined. After the hydroxylation step, the

surface should be ultra-hydrophilic, which means that the contact angle is close to zero. After the formation of a densely packed SAM, the sample surface should be very hydrophobic, indicated by a contact angle much higher than that of the sample surface without any treatment. The contact angle increases with the increase of immersion time as gradually more and more SAM molecules adsorb onto the surface. The increase of the contact angle will reach saturation when the reaction equilibrium is reached and the maximum contact angle is achieved.

For the contact angle measurement a 4.5 µL DI water droplet was pipetted on the surface of the sample. An average contact angle of 47.5 ˚ (5 sample points) was recorded after the chemical clean process and is shown in Figure 78 c). After the formation of the TTCS monolayer a contact angle of 92.6 ˚ was measured, thereby confirming the presence of the monolayer coating, also shown in *Figure 78* c).

Figure 78 shows a comparison of the reflectance spectra before and after the monolayer formation. The result in Figure 78 a) and b) show a wavelength shift of 519 pm and 284pm in the second band and first band resonance respectively. Again, the second band exhibits greater sensitivity, in agreement with the ZnO ALD experimental result and modelling.

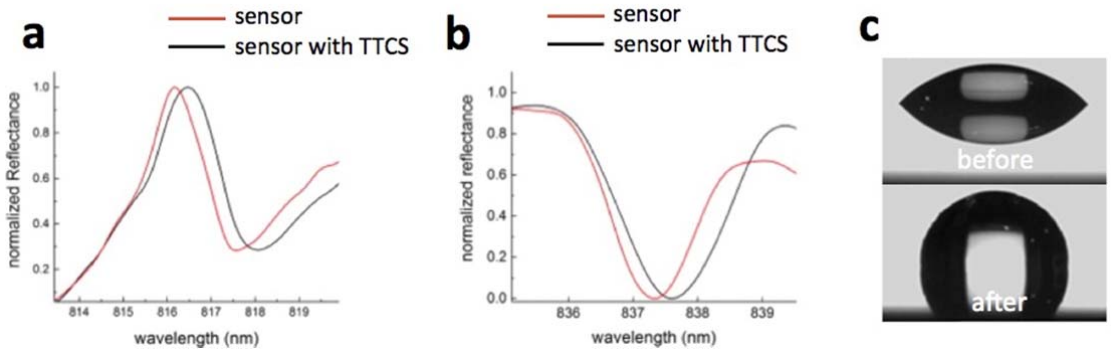

Figure 78. Contact angle measurement and spectra shift from TTCS process. a) second band response b) first band response and c) contact angle measurement.

9.2 Monitoring the interaction of double strands Deoxyribonucleic acid (DNA) hybridization process

Over the past 20 years DNA array-based biosensors have been developed for genetic mutational analysis [161][162][163]. The transducer or sensor needs to be functionalised with a biological recognition layer in order to selectively hybridize target molecules. Two types of biosensors, which are based on the recognition process, have been developed in the past two decades. One

relies on the surface attachment of the antibody, oligonucleotide, in this way the target can be selectively bound with the recognition layer. The second process is based on an immobilizing enzyme upon the sensor surface in order to form the recognition layer. Nucleic acid recognition processes are widely applied in identifying genetic diseases, DNA damage and DNA interactions[164][165].

Here we applied oligo-DNA hybridization to test the performance of PCs sensor. This process is based on the immobilization of single stranded DNA probe onto surface and the complementary DNA is sequentially hybridized with it. The immobilization single stranded DNA probe plays a key role in the hybridization process.

A common way to introduce the recognition DNA probe on the transducer is by using thiolate DNA on a gold surface, this is done via covalent linkage between the functional alkanethiol layer and the gold surface. The following section details a method of covalently attaching a thiolated DNA oligonucleotide onto the SiON surface. This procedure includes silanization of the SiON surface, introducing a heterobifunctional crosslinker, the attaching of thiol-labelled DNA and the hybridization of the complimentary DNA shown in Figure 79.

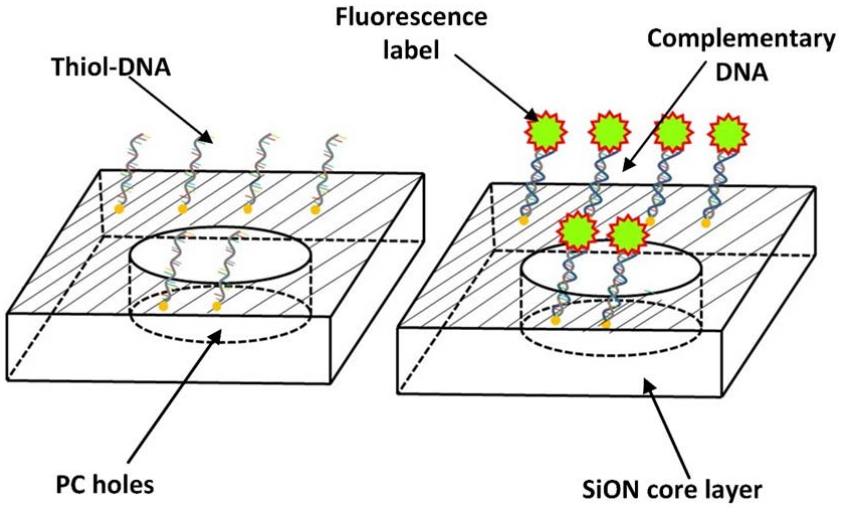

Figure 79. DNA hybridization process on PC sensor

9.2.1 Surface chemistry modification for a oligo-DNA probe and complementary DNA hybridization process

The PC sample was cleaned for 10 minutes by sequential sonication in both acetone and IPA and then finally dried under nitrogen. Prior to silanization, the sensor was subjected to an oxygen plasma clean. This will also introduce polar function silanol group (SiOH) resulting in a more

hydrophilic surface. This hydroxyl group is displaced resulting in $-\mathrm{Si}-\mathrm{O}-\mathrm{Si}-$ bound to the SiON surface, the components are shown in Figure 80.

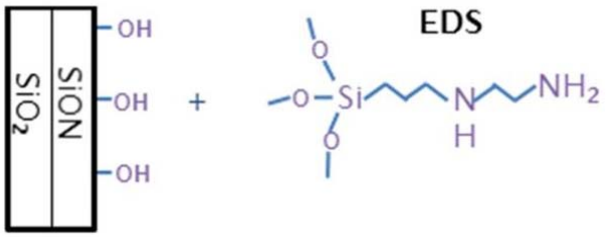

Figure 80. Introduce Silanol group (SiOH) on SiON surface and functionalized with EDS

To achieve this functionalisation the PC sample was immersed in acidic methanol solution (%5 water, 1% N-(2-aminoethy)-3-aminopropyl-trimethoxysilane(EDS)), the solution is adjusted to PH 5.2 by dropping acetic acid under agitation for 40 mins at room temperature. After this process the sensor was rinsed repeatedly (3 times) with methanol and DI water, dried under nitrogen and then cured at 110℃ in oven to complete the chemisorption process[166].

In order to link the DNA to this silanized surface, the sensor surface was modified with heterobifunctional crosslinker, N-(γ-maleimidobutryloxy) succinimide ester (GMBS). 0.0015g of GMBS was dissolved in 1ml of Dimethyl sulfoxide (DMSO) and diluted in 4ml methanol prepared as 1mM solution. The PC sample was left in GMBS solution for 2 hours on a rocker, then rinsed with methanol several times and dried under N_2. At this point the maleimide portion is ready to react with thiol labelled DNA as shown in Figure 81. Before introducing thiol-labelled DNA, the zero-reflection was measured and provides a reference prior to the DNA probe.

Figure 81. Modification of Silanized substrate with heterobifunctional crosslinker GMBS

In the next step 20 µM of thiolated DNA oligonucleotide (TATGACAGCAGTCTTTATG) solution (DNA was deaerated in 10 mM HEPES, 5 mM EDTA buffer with PH 6.6) was then dropped on to the cross linker treated sensor, covered with glass slide and left overnight at room temperature. It

was then rinsed in HEPES and EDTA buffer and dried under nitrogen. Zero-order reflection is again recorded to measure the thiol labelled DNA attachment. This binding process is shown in Figure 82.

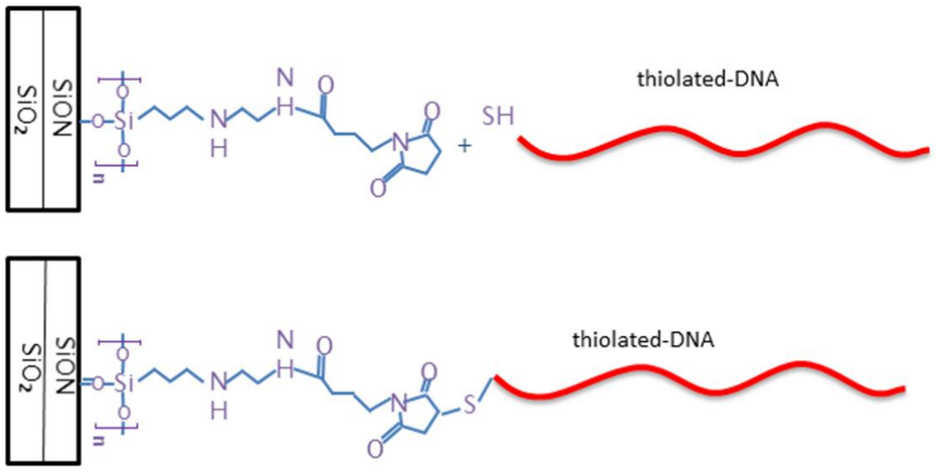

Figure 82. Thiol-DNA oligonucleotide probe is conjugated to the modified surface

In the next step the PC sensor was rinsed in 1 mM Hercaptoethanol solution several times then immerged in PBS solution (PH 7.4) for 1 min. Then it is covered by florescent labelled DNA (ATACTGTCGTCAGAAATAC) solution (the hybridization of the complementary DNA with florescent end was kept in 10 mM HEPES, 5 mM EDTA buffer with PH 6.6), and left for one hour. This binding is shown in Figure 83.

Figure 83 Hybridization of florescent labelled complimentary DNA

Finally, the sample was cleaned with phosphate buffer in order to remove any residue. Details of buffer preparation and DNA hybridization process are described in APPENDIX D.

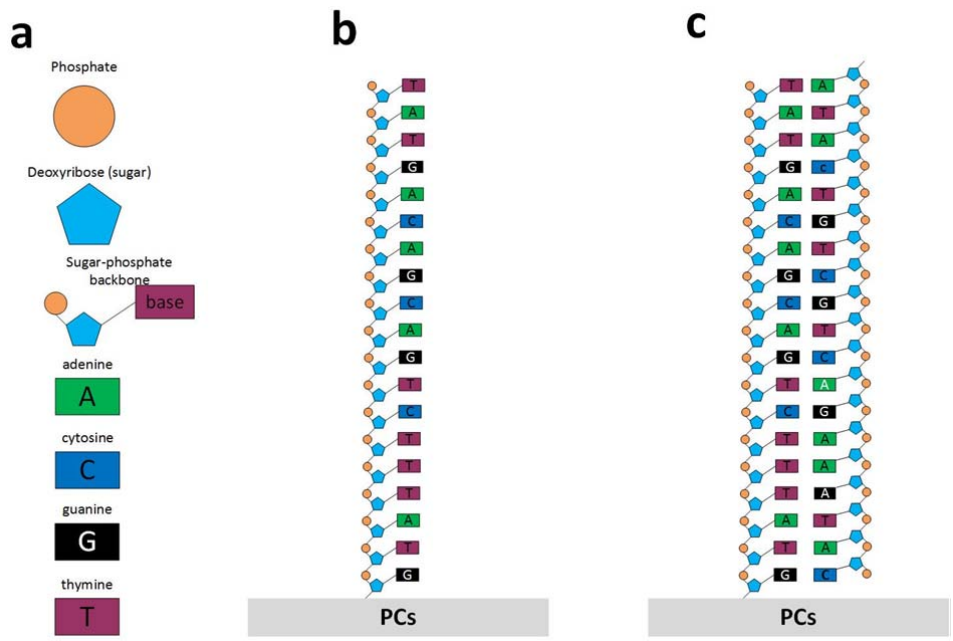

Figure 84. Schematic DNA oligonucleotide and hybridization step. a) Elements in DNA. b) Attachment of thiol DNA (19 bases probe DNA). c) Hybridization of the complimentary DNA.

To check for successful hybridization the PC sample was checked with a Zeiss Axiovert 200 microscope to image the attachment of the fluorescein labelled DNA. Figure 85 shows the comparison of fluorescent images before and after hybridization process. A uniform fluorescence was observed (Figure 85 b), thus the attachment of DNA to the PC surface was achieved.

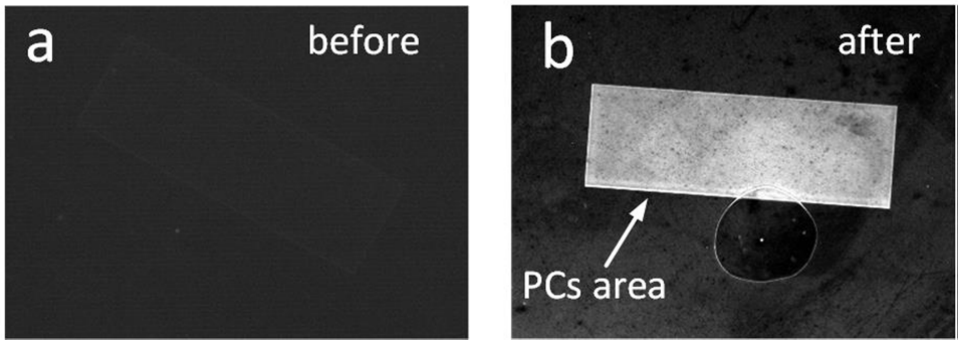

Figure 85. Fluorescent image of PCs a) before b) after hybridization

The zero-order reflection spectrum was recorded at the stages of crosslinker attachment, thiol-DNA binding and fluorescein complimentary DNA hybridization. The first three photonic crystal bands were measured for each stage and are shown in Figure 86. From the data it can be seen that the addition of the crosslinker layer introduced a ~0.5nm wavelength shift, the thiol-labelled DNA resulted in a ~1nm shift in resonance and the Fluorescein-DNA showed ~0.6 nm shift (average for three bands). It was noticed that the sample surface became 'unclean' during the

DNA attaching steps. As a result this changed the reflection intensity compared with first step (introduction of the crosslinker layer). However, only the resonant wavelength is considered here.

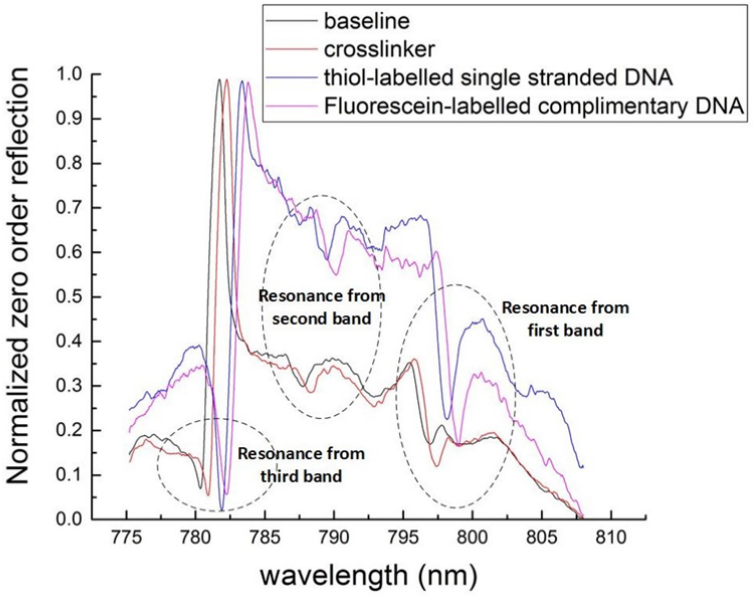

Figure 86. Spectrum of PC device at each binding point

The second band resonance shows the largest shift of 2.42 nm after the hybridization process. Displaying a similar trend as the ZnO and TTCS monolayer experiments. In comparison the first and third band resonances shifted by 2.03nm and 1.88nm respectively. A plot of each band resonant wavelength shift for each binding point is shown in Figure 87.

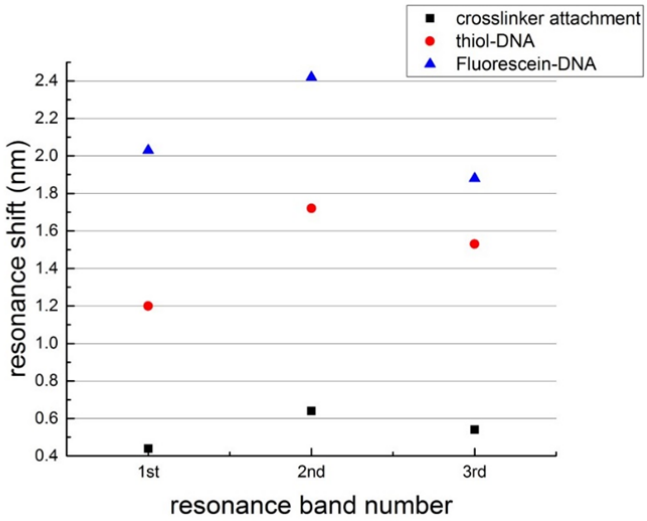

Figure 87. Resonance shift of the first three bands at each binding point

9.2.2 Summary

In this section a complete DNA hybridization process was successfully performed and showed that a double strand deoxyribonucleic acid hybridization process is detectable with a PC sensor via spectroscopic interrogation. Zero order diffraction with incident angle of near 0 ˚ was used to explore the PC's spectral shift introduced by the multilayer tethered molecules. These molecular layers include a crosslinker layer, thiol-DNA layer and a FL-DNA layer. Fluorescent imaging showed that the hybridization process was successful. The spectra of three PC bands were detected and compared at each step though the DNA hybridization process. The main issue of this experiment is that the chip must be dried before the measurement is conducted. In the next chapter the borosilicate glass chip is introduced in order to overcome this limitation when sensing in an aqueous or liquid environment.

Chapter 10: Sensing molecular interaction in aqueous environment

The previous chapters have shown that a photonic crystal sensor interrogated via angle resolved out coupled mode analysis (AROMA) provides a novel route to sense small refractive index changes. The angular deflection of the in-plane coupled mode is also sensitive to the refractive index change within the PC holes. A sensitivity of 6500˚/RIU was theoretically shown in Chapter 7 by changing the operating point to Γ.

In chapter 8 we showed that it was possible to detect extremely thin layers of deposited materials, i.e. monolayer molecules, onto the PC working area. The standard sensor, with the silicon substrate, was found to be unsuitable for detection in a liquid environment; this is due to the distortion of the projected spot introduced by the curve of the liquid droplet interface. In the biological world, the capability for detection in an aqueous environment is a prerequisite[167][168][169][170]. Almost all the molecular interactions such as ligand-protein, DNA-DNA, DNA and biotin-streptavidin are conducted in aqueous solutions. As we described in Chapter 8 the fluoresce labelled single strand DNA and thiol labelled DNA were stored in a HEPES buffer, the binding event occurs in this buffer on the sensor area in wet conditions.

In this chapter second generation sensor a borosilicate glass based sensor is introduced to provide the ability to detect within a liquid analyte is granted by projection through the substrate. Multiplexing detection was also achieved by integrating square, hexagonal and quasicrystal lattice couplers with square lattice sensors.

Operational demonstration of this glass device was conducted by detecting different concentration glucose solutions in order to explore the sensor's bulk sensitivity. Furthermore, interactions among cationic lysine, poly lysine and poly lysine with biocompatible cationic-anchored polyethylene glycol (PEG) was investigated in order to explore the surface response to molecular interaction dynamics.

10.1 Capture of the projected spot with a borosilicate glass device

In this device scheme, a PC couples the light into a planar optical mode which propagates towards the PC sensor. This guided mode is radiated, via the PC sensor, into free space, both top and bottom sides of the sample. Here is propose to use the angular deflection of the downside projection mode through the glass substrate, instead of using the front side projection as used in the prior chapters. Figure 88 shows a schematic of this operation concept.

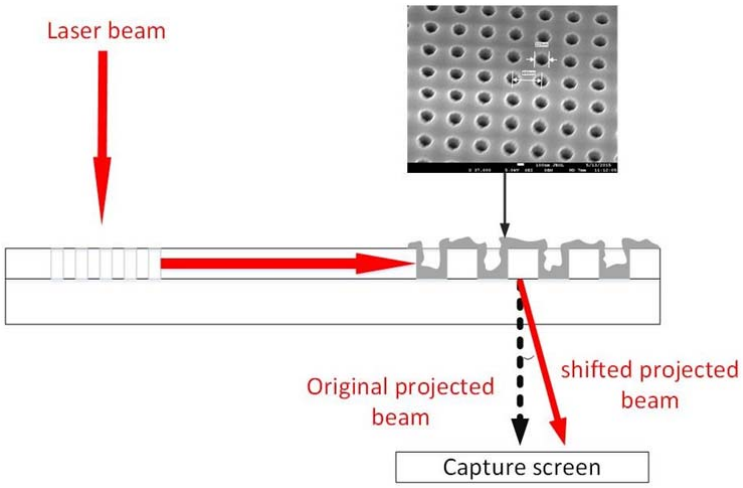

Figure 88. Schematic of the borosilicate device showing the projection through the substrate, permitting liquid detection.

All of the glass devices were fabricated on double-side polished 150mm borosilicate glass wafers (500µm thick), with a refractive index of 1.4713 at 589nm. Two of the fabrication steps are different from silicon based devices, they are the proximity error correction of the E-beam process and the removal of the 600 ˚C annealing step. Due to the low melting point the glass wafers were found to soften and bend during the annealing process. The waveguide loss was found to rise to 2 dB/cm without annealing, which was measured using a Metricon prism coupling system. However the loss is low enough to produce functional performance (Figure *89*).

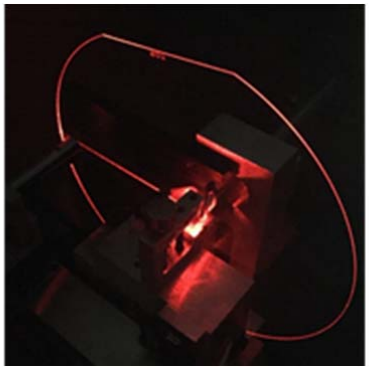

Figure 89. Image of the light guiding quality of the SiON film on a borosilicate substrate at 633nm. The image shows the Metricon prism coupling system with a red streak of guided light.

Three different chips with a square lattice coupler, hexagonal lattice coupler and quasicrystal coupler are successfully demonstrated in Figure 90. All the split beams are guided in the core layer to different sensors.

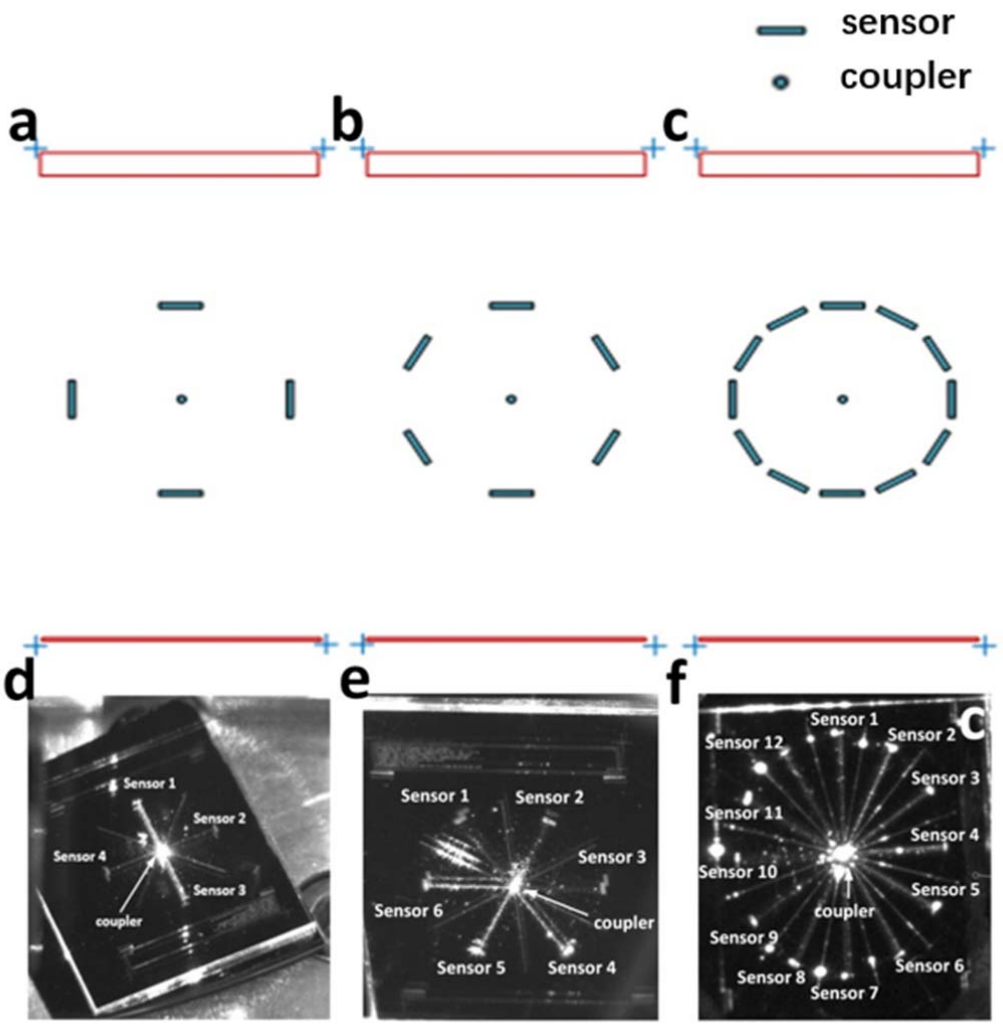

Figure 90. Demonstration of borosilicate glass chips working at 785nm. a) GDS layout of a square lattice coupler with four sensors. b) GDS layout of a triangle lattice coupler with six sensors. c) GDS layout of a quasicrystal lattice coupler with 12 sensors. d) Experimental coupling and splitting on a square lattice coupler incorporating 4 square lattice PC sensors. e) Experimental coupling and splitting on a hexagonal lattice coupler incorporate 6 square PC sensors. f) Experimental coupling and splitting on a quasicrystal lattice coupler incorporate 12 square PC sensors.

To achieve the highest sensitivity design on a glass sample, the guided mode should be projected vertically in the presence of the native solution i.e. DI water. In order to produce this condition a lattice pitch of 500nm and hole diameter of 230nm was determined via modelling. The simulation

was conducted with the water infiltrating the holes and covering the surface of the PC as shown in Figure 91, thereby mimicking the real environment. The monitor is placed at the bottom of the PC area.

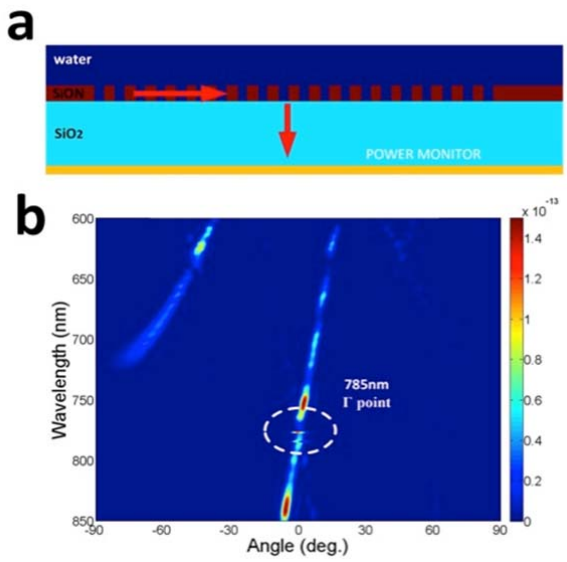

Figure 91. FDTD modelling of the farfield projection from the sensor (a:500nm, d:230 nm) in the presence of DI water. a) FDTD 3D model (cross section). b) far field dispersion map.

The actual Γ sensor was fabricated as previously discussed with hole diameter of 230 nm and lattice pitch of 500 nm, the measured angle resolved reflection dispersion map is shown in Figure 92. The vertical coupling was clearly achieved at 785 nm.

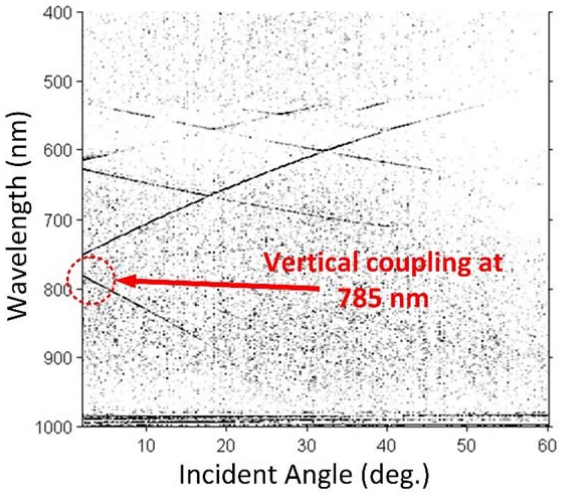

Figure 92. Angle resolved dispersion map from vertical coupling sensor in buffer condition (a: 500 nm, d: 230 nm)

10.2 Measurement setup for the demonstration of detection in an aqueous environment

In order to easily test the sample in liquid conditions a new setup was constructed (Figure 93). The input laser (A) is a 785nm laser diode with an output power of 6.5 mW and coupled via a PM-fibre pigtail. The fiber is connected to a collimator (B) whose orientation determines the polarisation of the probe light. After focusing by a 100mm plano-convex lens (C) the beam is directed to the sample with tuneable angle by a beam deflecting mirror (D), the range of angles is up to 60 °. This mirror provides quick adjustment of the optimal input coupling condition. A bespoke sample holder (E) provides precise translation of the sample position and crucially allows the back projected beams go through. To provide liquid submersion the sample must also be held horizontally without any tilt on the sample holder. The holder mount (G) ensures the setup is robust. The spots from the sensor of borosilicate glass chip was projected on to the matte screen (F), this projection distance is ~12cm. This projection is imaged onto a 10 megapixel CMOS camera which records a real time image (J). The camera is mounted on a 2-axis translation stage, which allows selection and position adjustment of the projected spots. An additional digital imaging system (H) assists in the alignment of the input light to the PC coupling region.

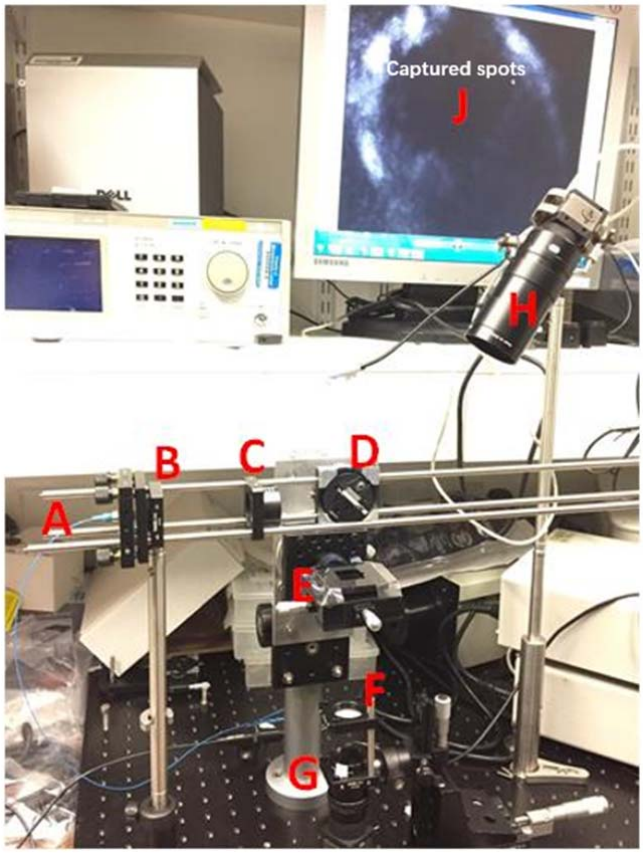

Figure 93. Experimental setup for liquid detection

10.3 Sensing different concentrations of glucose dissolved in DI water solution

Different glucose concentration solutions were applied in order to demonstrate the function of RI sensing and investigate the performance of bulk sensitivity. High quality D-glucose powder (mw:180.16) was bought from Thermo Fisher scientific. Six different glucose concentrations in DI water solutions were prepared (31.6mM, 100mM, 166.6mM, 250mM, 333 mM, 500mM). A PDMS manifold (manifold A) was made in order to control the volume of the droplet on the sensor. The concept of this process is shown in *Figure 94* a and an image of the glass substrate PC device is shown in Figure 94 b. Controlling the droplet volume is critical in this experiment, therefore a PDMS manifold is required in order to control the volume of the liquid. Figure 94 c shows an image of the PC chip and manifold A, and highlights a 1mm wide channel which is aligned to area above the propagating path between the PC coupler and PC sensor areas. This channel avoids the PDMS from affecting the propagating mode in the slab waveguide . A 5µL droplet is sufficient to fill the hollow column (2mm in diameter) above the sensor area. In this manifold there is also an open area in the centre of PDMS manifold for the incidence beam.

Another PDMS manifold (manifold B) without a waveguide open channel was built and used for surface conditioning and cleaning. It does not matter whether the coupler area is open or not. Just prior to the experiment, the sample with PDMS manifold B was treated with an oxygen plasma in the RIE 80+ plasma etching tool. This process results in a more hydrophilic surface and ensures the sensor surface is clean. Crucially this step isolates the liquid to only the sensor area preventing it from penetrating into the open channel area when manifold (A) was used during the measurement.

Figure 95 shows an example of the projected spot from the device under the conditions of absence and presence of the liquid analyte. The initial position of the spot located at the top left corner in Figure 95 a). In the presence of a glucose solution the spot moves to right bottom of the image Figure 95 b).

The refractive index of each concentration glucose solution was extracted from the literature[171]. The glucose solutions refractive indexes ranged from 6.64×10^{-4} to 1.05×10^{-2} greater than the refractive index of pure DI water. A plot of these literature values against concentration is shown in Figure 96.

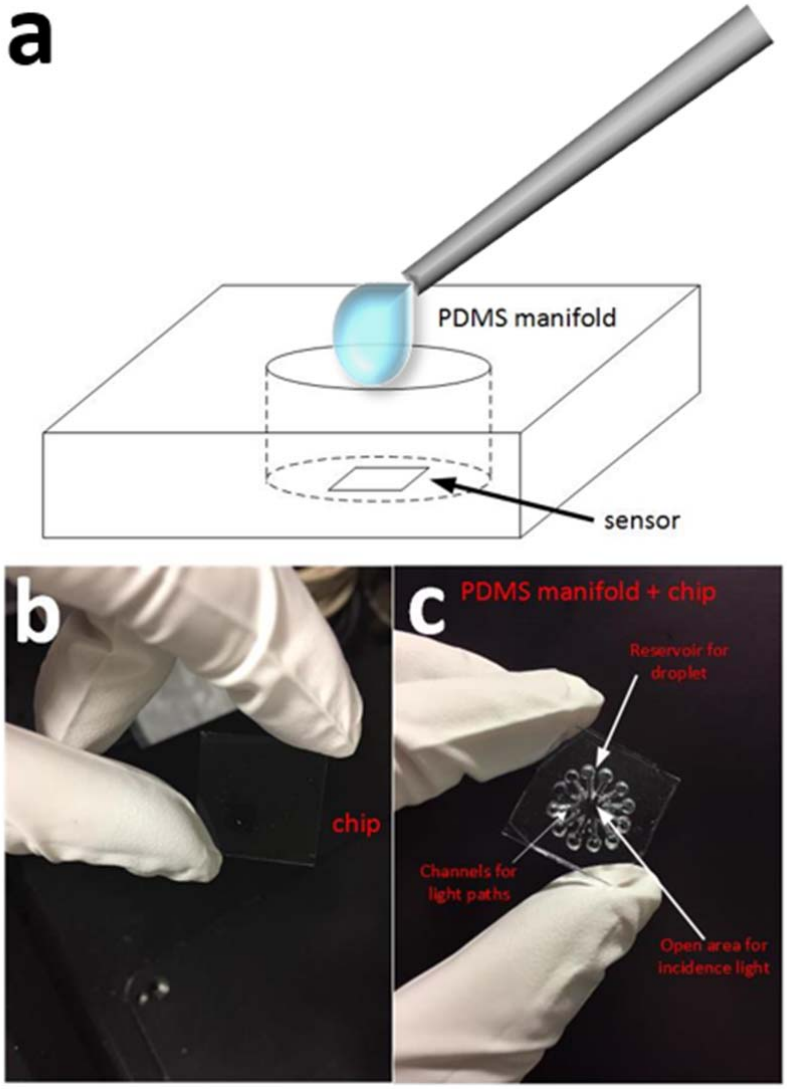

Figure 94. PDMS manifold design to control the volume of liquid. a) Schematic of PDMS manifold. b) Borosilicate sample with 12 sensors. c) PDMS manifold incorporated with the sensor.

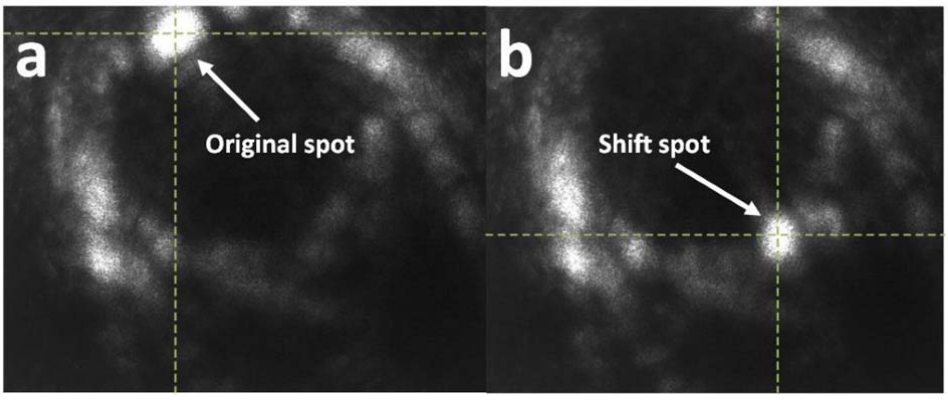

Figure 95. Spots shift by introducing glucose solution on to the sensor. a) original spot position. b) shifted spot position.

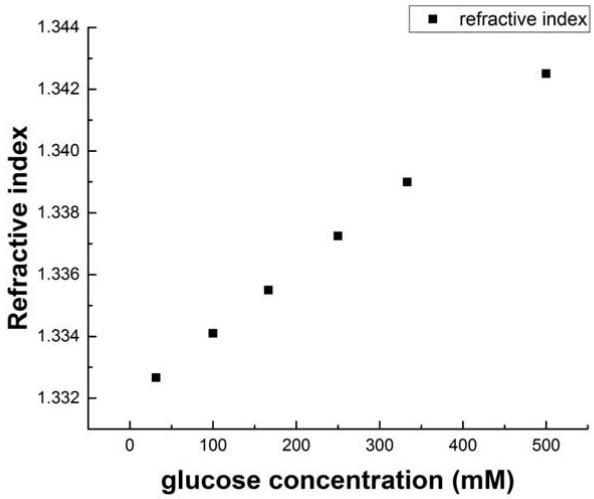

Figure 96. Glucose concentration vs refractive index, data taken from [171].

Different concentration glucose solutions were tested sequentially from low concentration to high concentration, with a baseline test conducted between each measurement (DI water wash and baseline measurement). The sensor baseline test ensured that the previous glucose solution was washed away. Figure 97 shows the refractive index response of the sensor (measured in pixels) when exposed to the different concentration glucose solutions. A linear response was observed with increasing the concentration of the glucose solutions. Each concentration was measured three times during the entire experiment. The plot is based on the calculated standard derivation and mean value from three experiments.

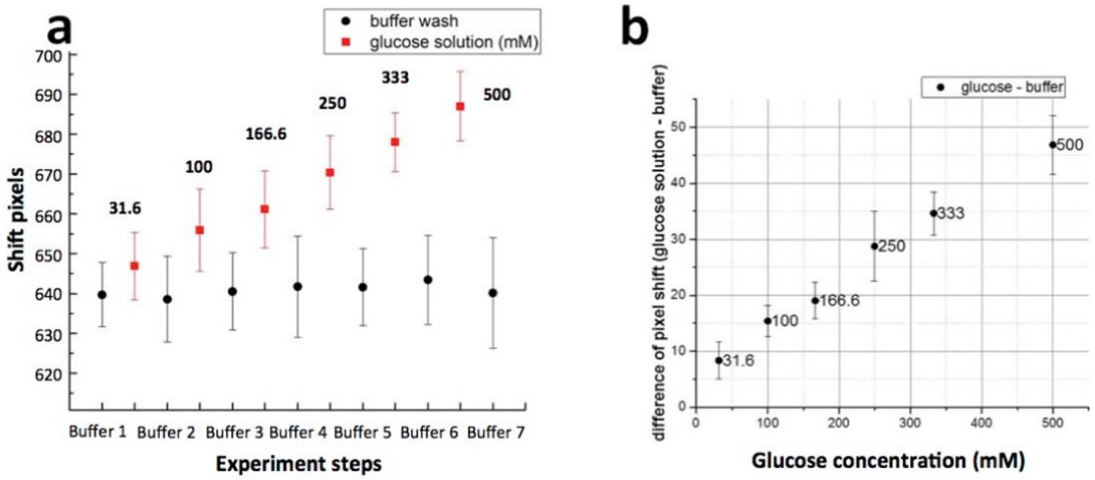

Figure 97. Glucose measurement result. a) Shifted pixel vs each glucose solution. b) shift distance between measurement of glucose solutions and DI water.

The variation is so large is because that the process of washing and inserting the analyte disturbs the alignment. A microfluidic feed system might yield more reproducible results.

The results from this section show that this PC sensor is sufficiently good to distinguish between glucose solutions with mM differences in concentration. However, this experiment does not provide any information about the suitability for measuring surface binding events. The next section looks at the response of this device to the interaction between the surface and molecules.

10.4 Monitoring the Binding event on SiON surface with charged molecules

L-Lysine and poly L-lysine (PLL) as cationic species are widely used to link functional molecules like polyethelene glycol (PEG), which can act as an isolation layer for preventing the adsorption proteins such as fibrinogen[167]. PLL-PEG is also used for the preparation of polymeric drug conjugates[172]. Because of the positive charge in L-Lysine or poly L-lysine it is suitable for robust binding with a silica surface. After introducing more hydroxyl (-OH) groups, via an oxygen plasma, the SiON surface is more negatively charged (more Si-O-H silanol groups). The L-Lysine/poly L-lysine bond exceptionally well with this SiON surface. Once a monolayer of LL/PLL molecules are formed on the surface, they will repel other LL/PLL molecules due to charge. Additionally the higher molecular weight homopolymers will replace one with a lower molecular weight[167].

The types of cationic molecules used in this experiment were L-Lysine with 146 MW, ploy-Lysine with 30K MW and Poly-Lysine with 300K MW. Each of the molecules will introduce a monolayer molecular coating with different thickness, and so each will show different angular output coupler response. Each of the lysine solutions are dissolved in 1×PBS buffer solution to achieve a concentration of 100μg/ml.

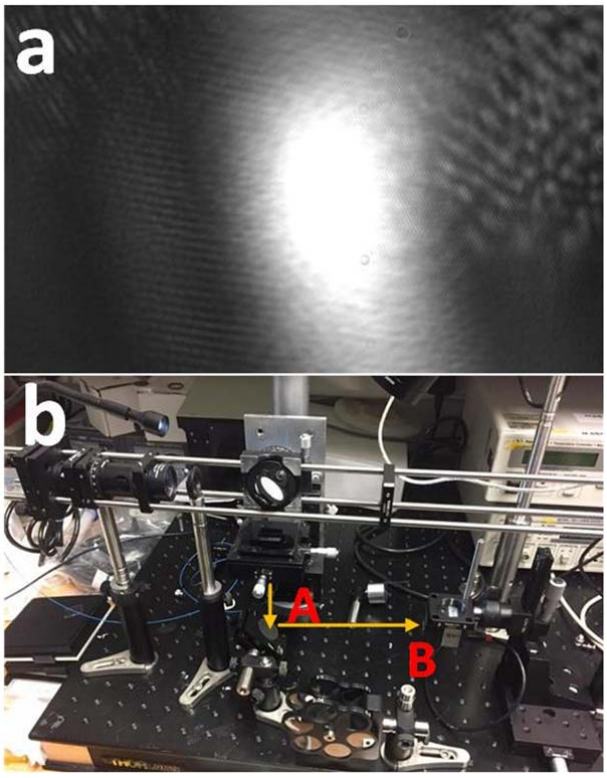

Figure 98. Improved setup for PLL binding experiment. a) the projected spot captured directly by the camera. b) The improved measurement setup showing the changes in the beam path.

An improved measurement setup, shown is Figure 98, was built in order to improve the readout. The matte screen was removed in order to decrease the noise caused by scattering on the roughness of the screen surface. The projected beam was deflected by a silver mirror (A) directly onto the camera screen (B). This allowed the projection distance to be increased from 12 cm to 30 cm (the modified light path is shown as yellow arrow in Figure 98).

After the sample was prepared with an oxygen plasma and inserted into the measurement setup the 1×PBS buffer is introduced to the sensor. This is then followed by the addition of the l-lysine solution. PBS buffer is then re-introduced to rinse the sensor surface after it has been saturated by the l-lysine molecule.

The 30K poly-lysine was introduced to challenge the base l-lysine attached on the surface of SiON. The PBS buffer wash was introduced again after the l-lysine is completed replaced by the 30K poly-lysine molecules.

Same procedure was conducted for the biggest molecule (>300,000 MW) poly-lysine solution. Eventually all the molecules (30,000-50,000 MW) will be replaced. Snap shots of the live images are shown in Figure 99.

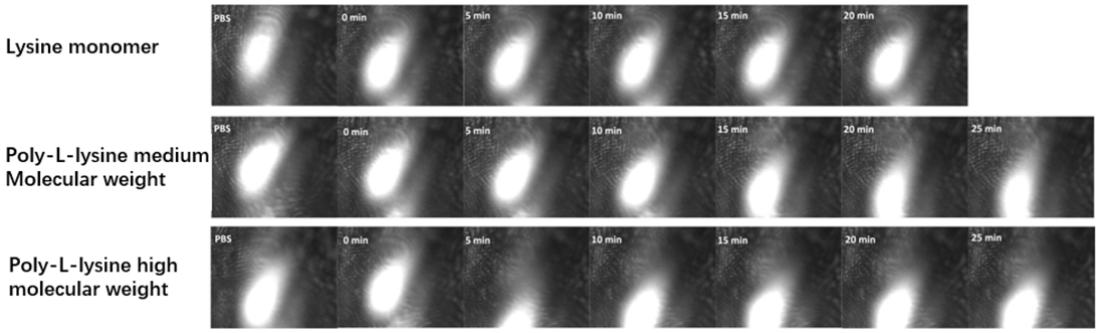

Figure 99. Experiment results of l-lysine and p-l-lysine challenge on the sensor surface

The spot shifted a large amount when the PBS buffer solution was present, the position of the camera was adjusted in order to target the shifted spot before the first contact with the lysine PBS solution. This is due to the large refractive index change between the solution and air conditions.

Interaction with the smallest molecule (l-lysine) shows a very small response in the spot displacement. At the beginning of this process the spot gradually shifted upwards for a short time, which is due to attracting molecules onto the surface by the charge. The sensor was continually washed with PBS buffer before the medium size molecule (30K-70K poly-l-lysine) was injected. A larger shift was recorded compared with l-lysine molecules. This process saturated after 10 mins implying all the l-lysine molecules were replaced by the PLL molecules by that time.

The situation with the 300K MW poly-l-lysine molecules was more complex, there was a big downwards shift in the first 5 minutes, then the spot shifted upwards a short distance and then saturated. It was postulated that this response might be due to the larger molecules forming clusters in the holes and distorting the sensor response. To investigate this a SEM image was taken of the PC sensor after the 300K MW poly-l-lysine step and showed the presence of clusters on the sidewall of the holes, shown in Figure 100.

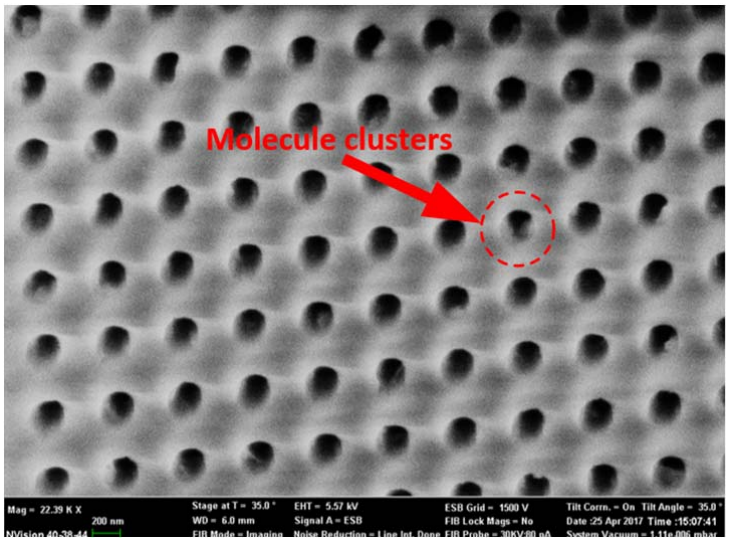

Figure 100. Top SEM image of molecule clusters in the holes of the PC sensor

The concentration used in the experiment (100 µg/ml) is a very high, this number of molecules can easily cover the sensing area and it will suppress the surface response. Additionally it is very hard to distinguish between the contribution of molecule induced pixel shift as the bulk solution and molecules attaching on the sensor surface will both affect the sensor performance. It is necessary to test the sensor with much lower molecule concentration to show the response of molecule binding on the sensor surface. To see the effect of concentration three different solutions of PLL (MW 30,000-70,000) were prepared (0.01 µg/ml, 0.1 µg/ml and 1 µg/ml).

For the first experiment the 0.01 µg/ml solution was pipetted and filled in the sensor area, the sensor surface will be partially covered by these molecules. A wash step followed before another PLL solution with 0.1 µg/ml filled the PDMS well. The surface of the sensor will be continually occupied by PLL molecules until it reaches the absorption point i.e. the entire surface is covered by PLL molecules. The same procedure was carried out for the higher concentration 1 µg/ml PLL solution.

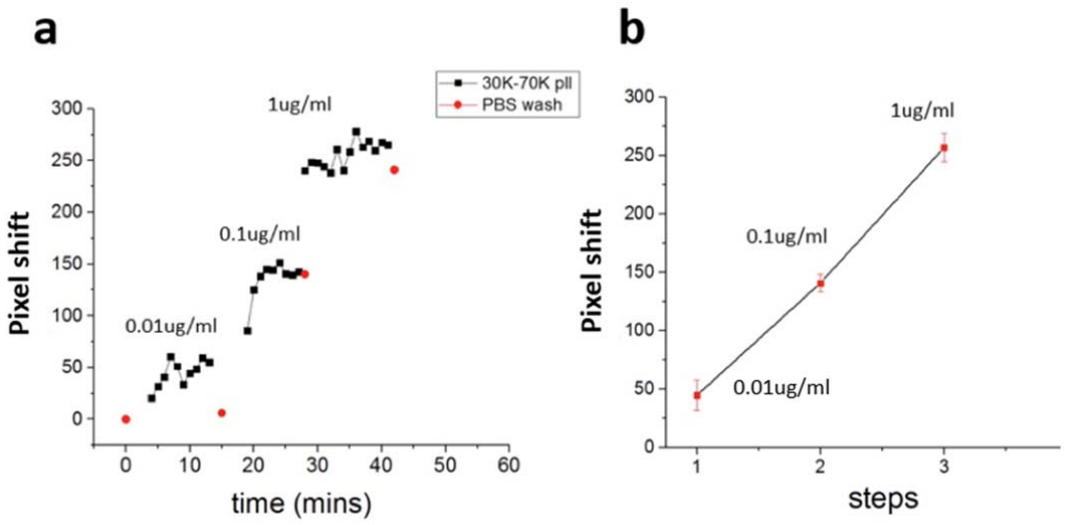

Figure 101. PLL binding saturation test. a) sensor responses according to different concentration PLL (0.01 µg/ml, 0.1 µg/ml and 1 µg/ml) and b) sensor response standard deviation plot.

Figure 101 a) shows the sensor response when PLL solutions with different concentrations are sequentially applied. *Figure 101* b) shows the terminal pixel shift values of each step, the error bars are from the standard deviation. This data clearly shows that molecules are continually assembling on the sensor surface before the 1ug/ml solution was applied. For the 0.01 µg/ml experiment the projected spot moved backwards to very near to the initial position (red dot) after the PBS buffer washing step, which means the bulk solution made most of the contribution to the spot shift. The addition of the 0.1 µg/ml PLL solution caused the spot to rapidly moved upwards for the first five minutes, however it did not shift back after the buffer wash. Here the surface absorption begins to dominate the spot shift. A similar result occurs for the 1 µg/ml solution and the spot remains stable at a pixel shift of 250. These results show that the surface becomes saturated with concentrations between 0.1 µg/ml and 1 µg/ml.

The kinetics of this molecular assembling process was investigated further. A new sensor chip was used, which was cleaned as before, and a single solution was applied and monitored. The concentration of 1µg/ml was chosen because lower concentrations only result in partial surface binding. The signal (spot shift in pixel) should increase rapidly during first few minutes (typical in 6 mins [167]) then reach the saturation point when the surface is saturated by the molecules. This experiment showed that monolayer molecules were assembled and covered the surface within 7 minutes. Comparing the final value with the initial spot position the response was much higher after the wash process, as shown in *Figure 102*. The shift is a little lower than that of the previous experiment, which is because the different sensor chip had a lower sensitivity. Even though they

are from the same wafer with same design, duplicating the sensor with exactly same fabricated structure is not possible. A small fabrication variation will change the performance, altering the Γ sensor design.

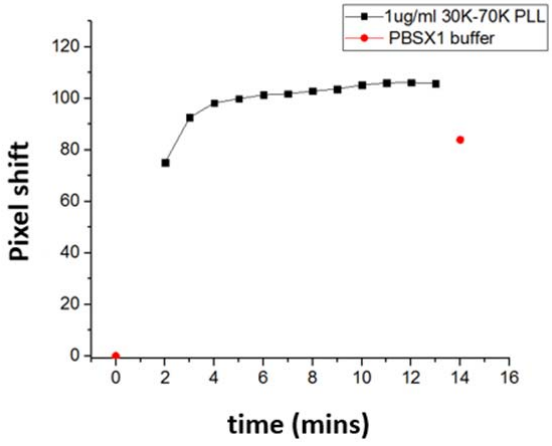

Figure 102. Captured spot shift under the condition of 1µg/ml PLL solution.

10.5 Monitoring a complex molecular replacement process

The copolymer PLL-g-PEG (polyetheylene glycol (PEG) side chain and ploy-l-lysine backbone) is commonly used as a protein-resistant charged molecule on negative samples like silica[173]. Here the PLL-g-PEG was applied to passivate the SiON sensor surface in order to completely prevent the adsorption of BSA (bovine serums albumin). A displacement of PLL-g-PEG was demonstrated by introducing PLL molecules with larger molecular weight. Further BSA was attracted to the homopolymer PLL due to absence of PLL-PEG.

An example of PLL challenge is shown in Figure 103. It shows a shifted spot trace with multiple steps including: initial adsorption of PLL(20K)-g-PEG (in 1×PBS) to establish the protein repelling layer; first challenge by BSA solution (100ug/ml, 1×PBS buffer, pH 7.4); subsequently PLL-g-PEG challenge by PLL (30K-70K) solution (in the same buffer); and the second BSA challenge performing the adsorption on the PLL covered sensor surface.

By exposing to PLL-g-PEG (MW 20K PLL base) the spot shifted in a negative direction and saturated after 6 mins. The spot position remained after introducing BSA (BSA is isolated by the PEG) and no shift occurred because of the PEG molecules. Then higher molecular weight PLL (30K-70K MW) is introduced in order to challenge the PLL-g-PEG on the sensor surface. This leads to the PLL-g-PEG surface being replaced by PLL (30K-70K MW) until the saturation point. The loss of

PLL-g-PEG is noticeable during the PLL/PLL-g-PEG exchange process, showing a large positive shift. The negative charged BSA is again introduce after the PLL challenge. A large adsorption is clear after the BSA is exposed to the sensor surface.

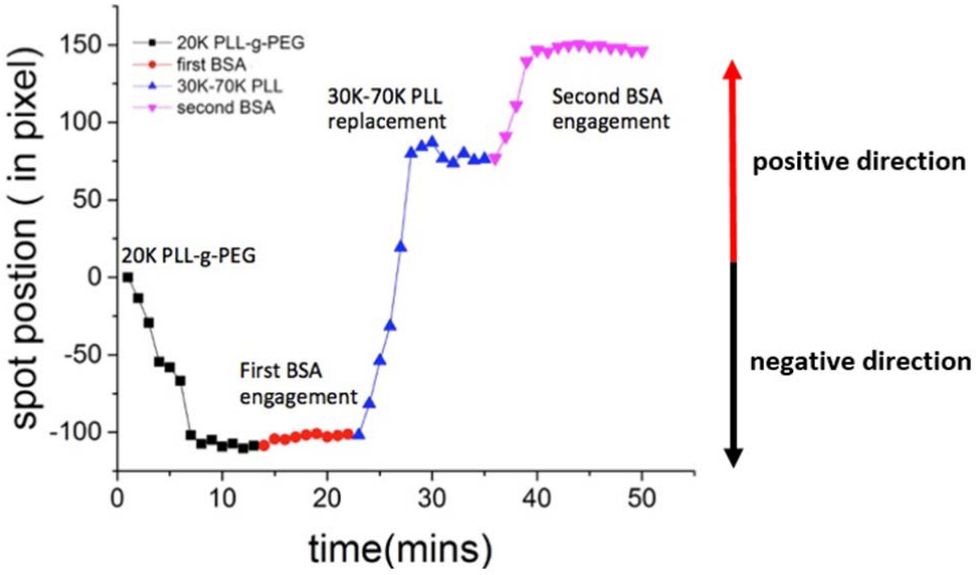

Figure 103. PLL challenge of PLL-g-PEG and BSA adsorption. The original PLL-g-PEG was challenged by homopolymer 30K–70K PLL (100µg/ml). The sensor was exposed to 100µg/ml BSA before and after this PLL challenge.

In conclusion, this PCs sensor platform shows the ability to detect sub μgmL^{-1} PLL solution with a current detection limit down to 0.1 μgmL^{-1}. This is competitive with the optical fiber grating coupler sensor with a detection limit of 0.5 μgmL^{-1} protein solution shown in table 2. However, it falls behind the SPR sensor which has a $ngmL^{-1}$ detection limit level in table 2.

10.6 Summary

In this chapter I have shown the successful transfer of photonic crystal/quasicrystal couplers and sensors from silicon substrates to borosilicate glass substrates. This transparent sensor is able to sense the refractive index change of surroundings in liquid conditions. In order to investigate the refractive index sensing performance a new measurement setup was designed and built. A PDMS manifold was applied to control the volume, the surface of the liquid and, with additional surface treatment, the possibility of beam distortion was avoided.

Glucose solutions with several different concentrations were prepared and used to represent different refractive index analyte in order to investigate the bulk sensitivity of this sensor. Pixel shift as the sensor response was recorded for each concentration glucose solution. It shows a linear response with respect to refractive index change.

Surface response was investigated via the charged molecules poly-l-lysine, poly-l-lysine with graft poly ethylene glycol and bovine serum albumin. Surface coverage, PLL challenge and the dynamics of interactions were explored with PC sensors.

Chapter 11: Conclusion and future work

11.1 Conclusion

This thesis started by introducing the photonic crystals and was the starting point for understanding the interaction between the photonic crystal propagating mode and surrounding environmental conditions. Review of the literature on the various schemes for electromechanical and optical biosensors highlights that several key features are required for a viable commercial biosensor. A simple fabrication method, employing a common material (i.e. cheap), with multiplexing capability and spectrometer free are all the key factors in order to minimize the cost and potential ability to mass produce. Consequently, it is necessary to design a multi-parameter sensing platform with a single light source.

In this thesis a practical single photonic crystal/quasi-crystal device was developed, which serves the dual purpose of coupling incident light with large beam size to a planar slab waveguide and splitting the coupled light power to multiple guided beams simultaneously. The experimental studies show very good agreement with theoretical predictions. A number of light channels are excited with the single monochromatic light source (633nm/785nm laser). The number of split beams depends on the symmetry of the photonic crystal lattice. Phase matching can be achieved between the coupled light and photonic crystal lattice resulting in multiple beams by altering the lattice constant and hole diameters. Square lattice coupler provides 4 splitting beams and hexagonal lattice coupler shows 6 splitting beams. It is also proved that the number of coupled channels can be extended beyond the natural limit of six by using a quasicrystal lattice structure which provides 12 beams. The theoretical design process is explained in detail. Demonstrator devices were designed to couple and split 'normally incident' 785nm light and were fabricated within a CMOS compatible fabrication process on a SiON slab waveguide. The implementation of the photonic crystal coupler simplifies the monolithic integration of the traditional design and fabrication of grating coupler and power splitter. High optical power throughput is provided due to the highly multi-modal nature of the generated in-plane beams. This configuration also eliminates loss incurred by the rib/ridge waveguide fabrication process. This combination of outstanding properties is a great benefit for multi parameter sensing.

Square lattice photonic crystals are integrated into different light couplers as sensors in order to achieve the goal of multi-sensing. The sensing mechanism is based on out-coupled mode analysis (AROMA) technology. The performance was theoretically investigated by RCWA and FDTD methods and demonstrated good agreement. The sensitivity increases with larger holes size and furthermore much higher sensitivity (above 6500 °/RIU) can be achieved by changing the out

coupling angle from negative detune to vertical angle coupling (Γ) at an arbitrary wavelength. This can be achieved by changing the lattice period and holes size. However, the narrow resonance window indicates the fabrication tolerance is low and a tuneable laser is required to investigate this phenomenon.

Practically the function test was successfully demonstrated on the Silicon based sensor chips with the diluted PMMA. Response of output coupling angle from sensor with different holes size shows an agreement with modelling.

The sensor was calibrated by sensing single nanometer thick layer coatings of ZnO deposited via atomic layer deposition. It showed a linear shift from the zero order reflection spectra and shows the potential to detect the presence of monolayer biomolecule coatings. In addition a self-assemble monolayer molecule TTCS was successfully assembled on the sensor, it was verified by the contact angle measurement. Hundreds of picometre level photonic crystal resonance shift from different photonic crystal bands were observed from the zero order reflection measured by reflectometry.

Deoxyribonucleic acid (DNA) hybridization was conducted on SiON/SiO_2/Si photonic crystal sensor. A double strands DNA hybridization process was achieved on the sensor surface sequentially including surface chemistry modification of crosslinker (GMBS), thiol labelled single strand DNA probe, fluorescence labelled complementary DNA. Successful hybridization process was verified with the florescent images. Each layer of molecular deposition was analysed by the response of the sensor reflection spectra. For each step the shift of photonic crystal resonance from reflection spectra was observed. Detectable resonance shifts were observed from the cross-linker layer, thiol labelled DNA layer and the complementary DNA layer.

In order to detect refractive index change from surrounding environment in aqueous conditions, coupler and sensors were successfully transferred on to borosilicate glass wafers. Experimentally a monochromatic laser beam coupled into different photonic crystal structures on the glass substrate, four beams, six beams and twelve beams were coupled into the slab waveguide on the glass substrate. These coupled in-plane beams successfully coupled out into the free space through the transparent substrate from the photonic crystal sensors. The projected beams were recorded by the cameras, which is placed underneath of the sample with a matte screen on the top. Glucose solutions with different concentrations (different refractive index) were measured by tracking the spot shift through the camera. A linear response was observed.

Sensor surface response was first tested with l-lysine and p-l-lysine (different molecular weight) and dramatic spot shifts were observed directly with the camera. The dynamics of small molecular

weight l-lysine being replaced by larger p-l-lysine was successfully detected. Furthermore 1μg/ml surface saturation point was found for p-l-lysine with molecular weight of 30K-70K.

In the end the dynamics of a series of molecules interactions (copolymer PLL(20K)-g-PEG, PLL (30K-70K) and BSA) were successfully demonstrated. Results showed the PEG successfully block the potential interaction between PLL (MW: 20K) and BSA. After replacing 20K PLL-g-PEG with larger PLL (MW 30K-70K) molecules, the BSA begin to interact with PLL.

These results show that photonic crystal sensors provided a new, spectrometer free method to detect the dynamics of molecular level interactions.

11.2 Future work

Although the function of this multiplexed photonic crystal sensor was successfully demonstrated on both silicon substrate and glass substrate devices. Improvements from different aspects are still need to be carried on in order to achieve the optima performance of these devices, which has been theoretically shown.

11.2.1 Intrinsic performance improvement

So far the optima of the high sensitivity condition (>6500 °/RIU) has not been experimentally demonstrated. This is because of the very narrow operating wavelength window and need for extremely precise fabrication. A perfect sidewall profile (highest aspect ratio) and precise etching depth (400 nm) are required to achieve this goal. In addition a tuneable wavelength laser system is also required in order to compensate for the narrow working wavelength window.

11.2.2 Readout improvement

Apart from the intrinsic sensor performance, improvements to the readout system can be explored to lower the detection limit. The final readout mechanism, used in chapter 9, has an advantage that a longer projection distance introduces a larger spatial shift in the spot position. However, the divergence of the beam limits the projection distance with the limit currently at about 30cm.

By introducing a short focus lens and placing the sensor at the focal point, one can collimate the beam in order to increase projection distance. However, this consideration is not ideal for mass production due to the difficultly of aligning the system over a long distance. The incorporation of a cylinder mirror will further amplify the deflection angle[174], although this again requires precise alignment.

11.2.3 Way of mass production and fast prototyping

Nano imprint with polymer material is a way to low cost fabrication and fast prototyping. A SION based sensor stamp has been fabricated in order to check the stamp quality with UV-curable polymer material (ormocore[175]). PCs pattern transfer is processed via an intermediate layer, the concept is shown in *Figure 104*.

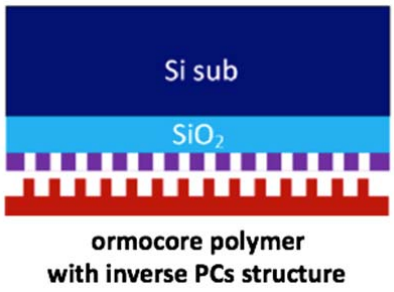

Figure 104. Inverse pattern transfer on intermediate polymer layer

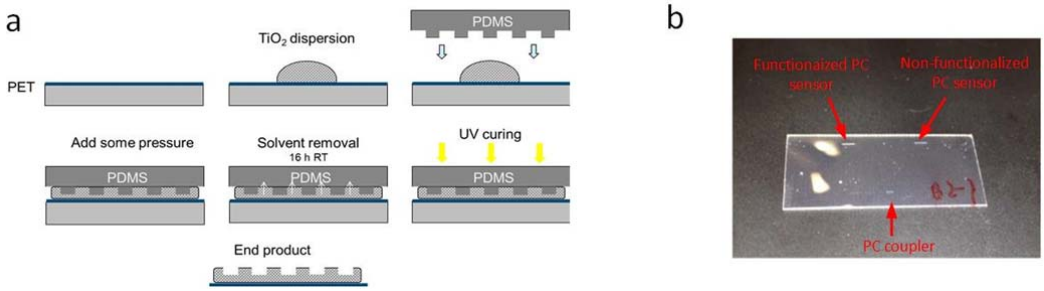

Figure 105. (a) imprint process for the manufacturing of TiO_2 nanocomposite PC sensors. (b) plastic chip (TiO_2 composite on PET carrier).

The intermediate layer with inverse PCs structure can be used to produce replicate PCs sensor. The intermediate layer can also use PDMS material. Full nano imprint process is depicted in Figure 105 for the replication of the SiON master in the polymer TiO_2 nanocomposite (50-60 wt% TiO_2 in an acrylate polymer matrix developed by TNO). First a mixture is made from TiO_2 nanoparticles in toluene. Then, a sufficient amount of acrylic monomers are added to ensure the correct weight percentage of nanoparticles are in the cured polymer. The selection of the TiO_2 composite polymer as the high-index polymer (refractive index of 1.71 at 785nm) means that hole-type stamps are the preferred choice. This is because the imprint process requires the solvent to

diffuse into the soft mould to achieve successful replication and therefore requires an intermediate HPDMS stamp[176]. The PCs structure was replicated in the imprinting mould of a thin layer of HPDMS on PDMS. Then the flexible mould was placed on a polymer-TiO_2 dispersion in monomer and the solvent was penetrating into the mould. After drying, the polymer layer was UV cured and removed form PET substrate. This fabrication is done by the partner but the fabrication process need to be optimized.

Appendix A

1. Automated broadband reflectometry system setup for measurement of photonic crystal dispersion.

An automatic measurement system based on reflectometry method was built up, which is comparable with the RCWA simulation. This set up can experimentally obtain the angle resolved dispersion map from PCs coupler. The schematic of the setup is shown in *Figure 106*.

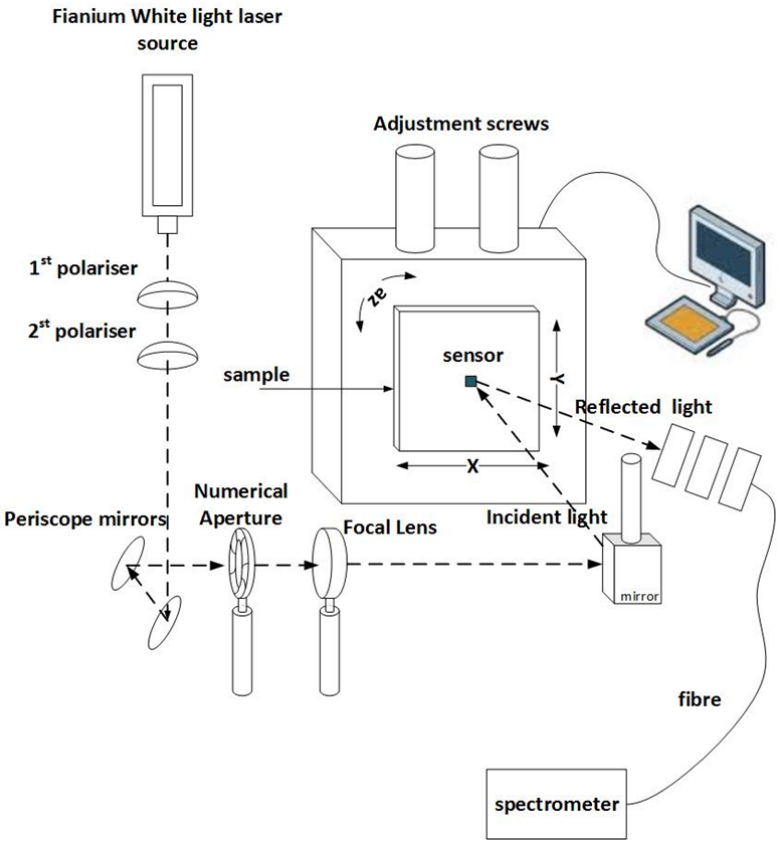

Figure 106. Schematic of reflectometry setup

This setup consists of a broadband laser source, computer controlled motorized stage, a polarizer, mirror, a pair of periscope mirror, an aperture and a fiber connected spectrometer. The broadband laser source is directed by the periscope and mirror, then focused onto the sample. The sample was mounted on the stage. The stage can be rotated from 0 to 180 °, which is able to cover the incident angle from 0 to 60 °.

Fianium white light laser is applied as the laser source, it has a broadband spectrum and stable high power density. This laser source is unpolarised and the broadband spectral bandwidth ranges from 450nm to 1800nm. The two polarizers are used for controlling the power intensity.

Before the un-focused white light shining on the sample, the beam is stray which uses achromatic doublet focus lens to confine. Finally the beam spot size is limited to round half mm diameter by an achromatic double lens. The lens can give a constant focus position with small beam distortion and a large range of wavelength.

The sample is placed on the stage, which can be controlled and moves along three directions (X,Y,Z) precisely. There are two motorized rotary stages to precisely control the incident angle and azimuth rotation. Since the target of measurement is nano-scale patterns and the patch of the pattern are about half mm by half mm, the stage should be aligned properly in order to get absolutely flat surface with respect to the incident beam and not shifting when changing the incident angle. With the help of those motorized stages the beam spot can be focused in the center of stage and even the stage is rotating. Figure 107 shows the alignment procedure. By tuning the X,Y,Z position of the sample holder, beam spot must goes through the aperture when the stage is rotated with different angle position.

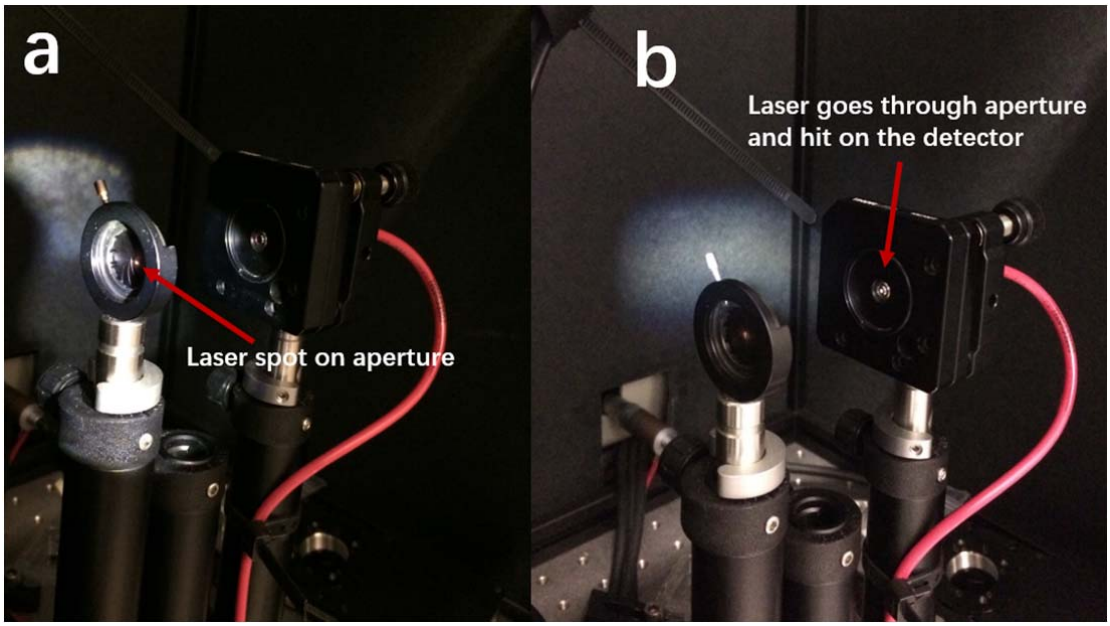

Figure 107. Reflectometry alignment procedure

An example of measurement result is shown in Figure 108. First three photonic crystal bands are highlighted and they are comparable with the simulation. The fundamental band will be used for the design of the input coupler and output sensor.

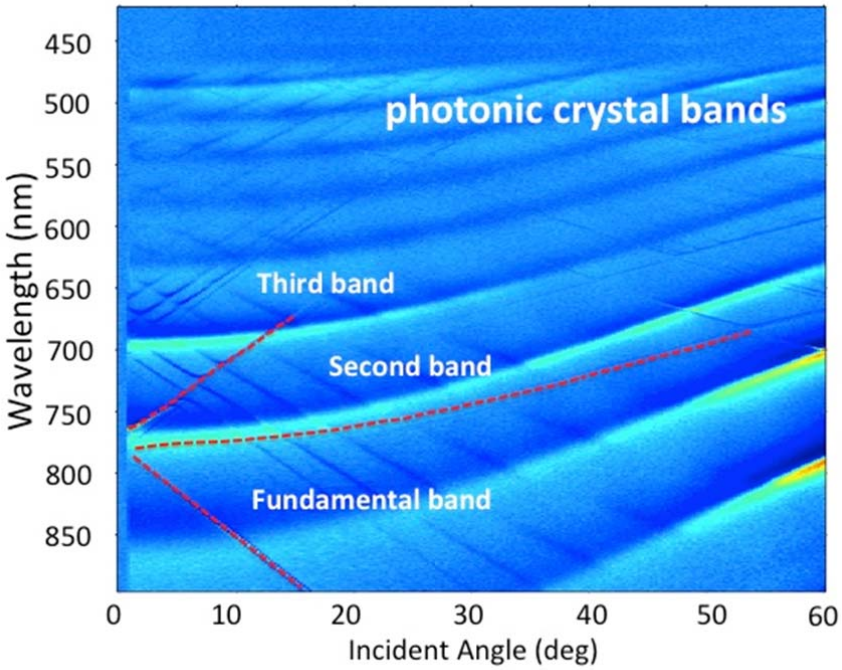

Figure 108. Angle-resolved zero-order reflectance measurement data of a hexagonal PCs coupler (a=570 nm and d=114nm) with white light source (s polarization).

2. Reflectometry data of quasicrystal structure on SiON/SiO_2/Si (TE polarization) with different azimuth rotation.

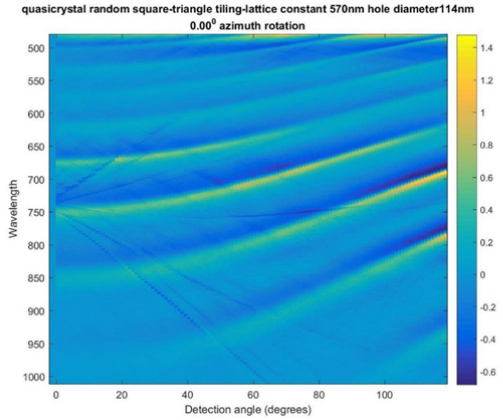

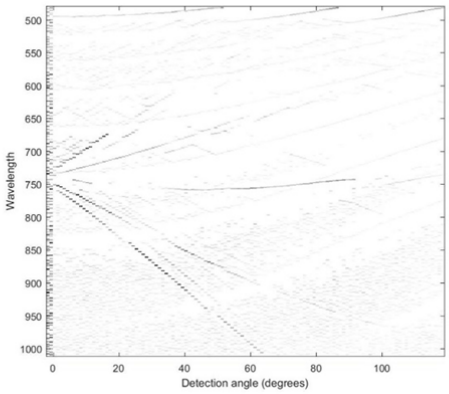

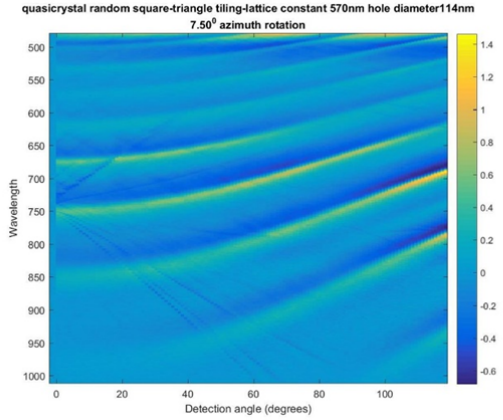

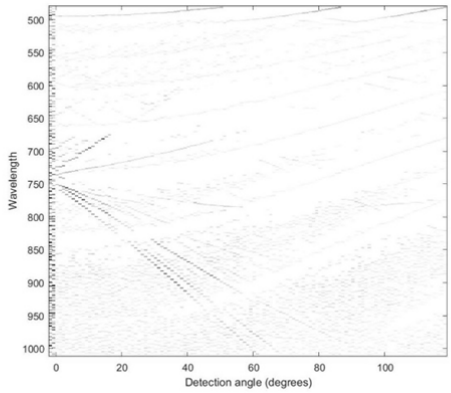

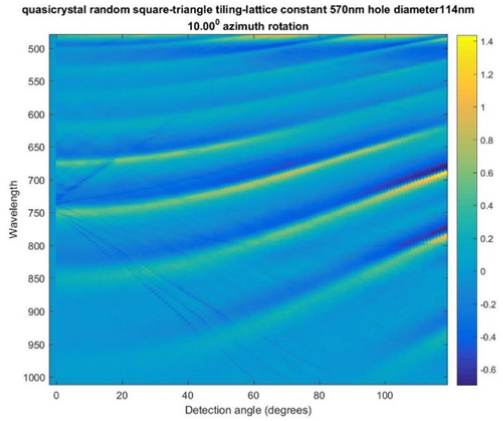

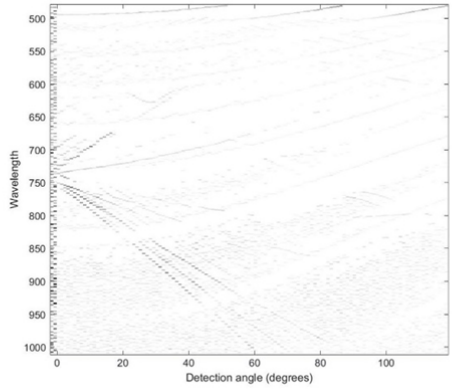

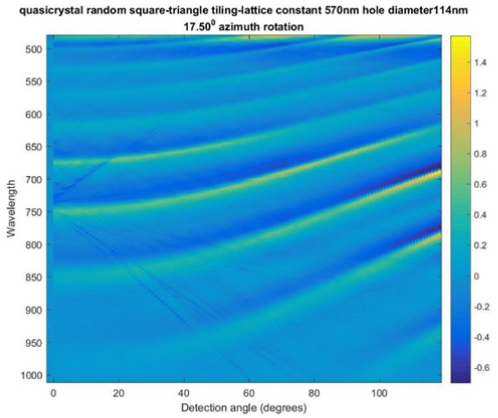
quasicrystal random square-triangle tiling-lattice constant 570nm hole diameter114nm
17.50⁰ azimuth rotation
Wavelength
Detection angle (degrees)

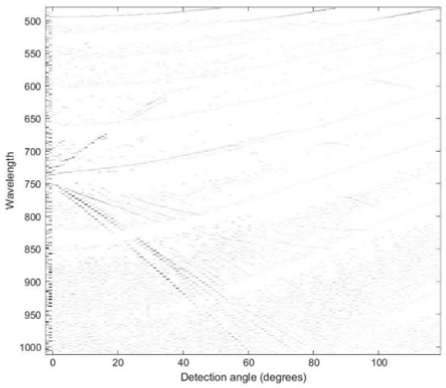
Wavelength
Detection angle (degrees)

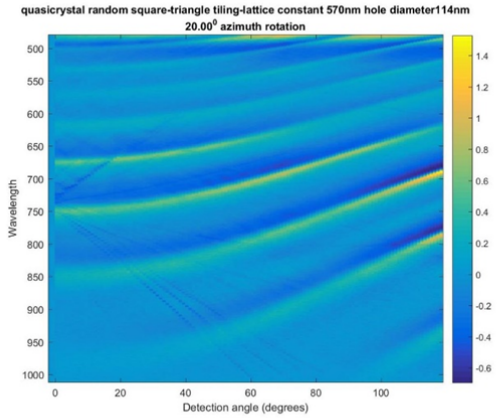
quasicrystal random square-triangle tiling-lattice constant 570nm hole diameter114nm
20.00⁰ azimuth rotation
Wavelength
Detection angle (degrees)

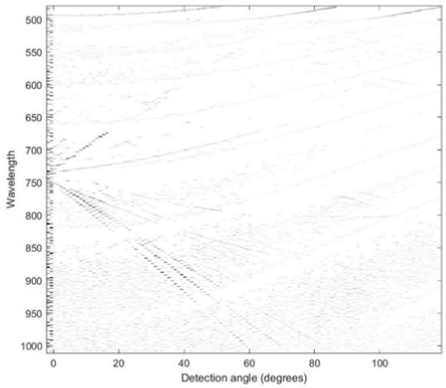
Wavelength
Detection angle (degrees)

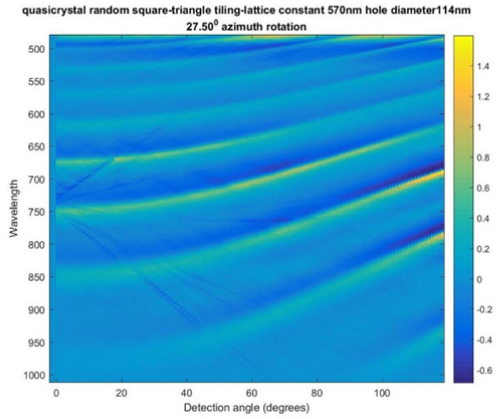
quasicrystal random square-triangle tiling-lattice constant 570nm hole diameter114nm
27.50⁰ azimuth rotation
Wavelength
Detection angle (degrees)

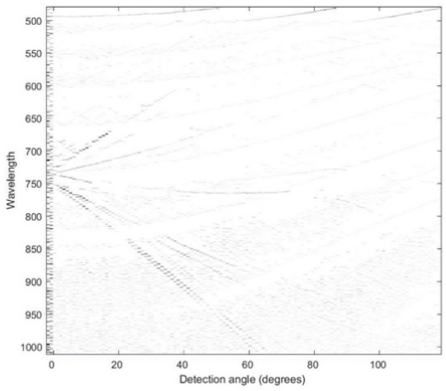
Wavelength
Detection angle (degrees)

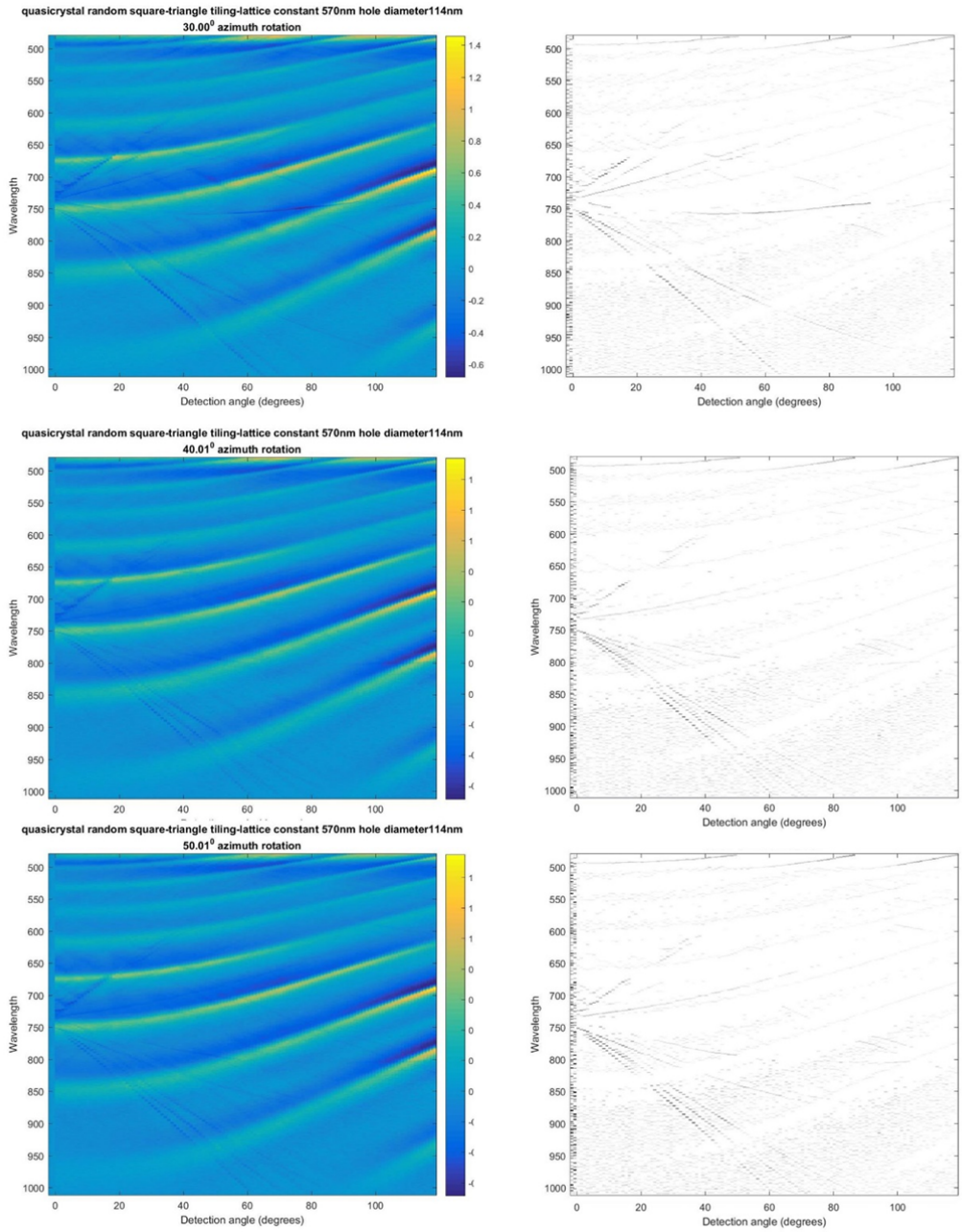
quasicrystal random square-triangle tiling-lattice constant 570nm hole diameter114nm
30.00⁰ azimuth rotation
Wavelength
Detection angle (degrees)
quasicrystal random square-triangle tiling-lattice constant 570nm hole diameter114nm
40.01⁰ azimuth rotation
Wavelength
Detection angle (degrees)
quasicrystal random square-triangle tiling-lattice constant 570nm hole diameter114nm
50.01⁰ azimuth rotation
Wavelength
Detection angle (degrees)

Appendix B

1. Bloch mode modelling

It is useful to investigate the bloch mode profile of PC sensor structure. By using FDTD farfield calculation the parameter of photonic crystal sensor for r point operation. There is another way to obtain the photonic crystal resonance information and extract the bloch mode. It is important to the electric field profile of the bloch mode, which is useful to see the field penetration depth into the holes. Firstly the photonic crystal 3D structure is constructed, the periodic boundaries are set shown in

Figure 109 a). By using these structures the band diagram can be calculated according to different k vector. The direction from Γ to X is considered because the propagating light is along this direction. Vertical projection means operating in Γ point, the mode with wavelength of 785nm appear in the Γ point from Figure *109* b). A monitor is set with this wavelength in order to extract the field profile information. The results are shown in Figure *109* c) and d). The field is enhanced in the bottom corner of the holes. The penetrated field depth is about 70 nm in these holes.

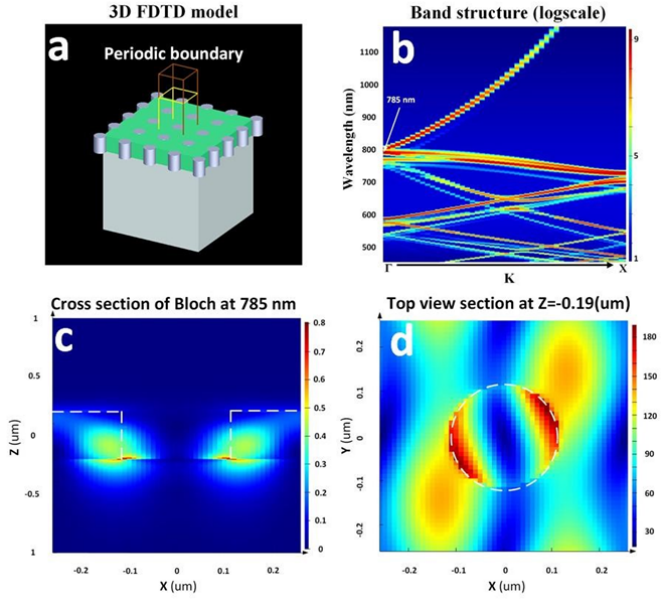

Figure 109 Modelling of Bloch mode profile. a) 3D PC structure (a: 530 nm, d230 nm), b) Band diagram of PC structure from Γ to X, c) cross section view of Bloch mode profile at 785nm and d) top view of Bloch mode profile at bottom of the photonic crystal holes.

Appendix C

1. Deoxyribonucleic acid hybridization experiment flow:

Step 1: surface chemical modification and SiON surface silanizaition

Required solvent:

Methanol, glacial acetic acid, N-(2-aminoethy)-3-aminopropyly-trimethoxysilane (EDS).

1. Rinsing sample in purified acetone
2. Plasma clean and introduce –OH group
3. Methanol (8.5ml) was mixed with DI water (1ml) and the glacial acetic acid drops by glass pipette and adjust the PH to 5.2, it is measured by PH paper.
4. Drop EDS (0.1ml) in the methanol with glacial acetic solution by syringe, and make the volume percent be 1% for EDS in solution. The syringe needs to be washed by methanol in order to avoid silanization in the syringe.
5. The sample was put in a glass container and the EDS solution is added on the sensor surface with a glass pipette. Then the container is loaded on the agitator for 40 mins.
6. Clean the sample with methanol and DI water followed by drying under nitrogen.
7. Sample is cured at 110 ^{o}C for 15 mins.

Step 2: hetero-bifunctional crossliner attachment

Required solvent : N-gamma-maleimidobutyryl(GMBS)

1. 0.0015 g GMBS is dissolved in 1ml DMSO then add 4ml methanol ((1ml DMSO and 4ml methanol)x4/5) in order to prepare 1mM GMBS solution.
2. Chip is left in GMBS solution for 2hrs.
3. Chip is rinsed in methanol without GMBS 5 times and dried under N_2

Step 3: Thiol labelled DNA attachment

Required material: thiol –labelled DNA , HEPES and EDTA buffer

1. Rinsing in HEPES and EDTA buffer (10mM HEPES and 5mM EDTA) 3 times
2. Immersing GMBS modified chip in (0.5uM) thiolated-DNA for at least 4 hours (glass bits cover sensor, drop DNA solution near edge of glass chip).
3. Rinse in HEPES and EDTA buffer 5 times, then dry by N_2

Step 4 : Complimentary DNA hybridization

Required material: Fluorescent-DNA, HEPES and EDTA buffer

1. Rinsing in 1mM Mercaptoethanol solution 5 times.
2. Rinsing in PBS solution (PH 7.4) 1 mins.
3. Fluorescent-DNA (10 uM) in HEPES and EDTA buffer is added to the chip, keep 1 hour at 4 degree.
4. Rinse in PBS solution (PH 7.4) 3 times

2. **Buffer preparation:**

10mM HEPES 5mM EDTA buffer:

1. add 2.38 g of HEPES and 1.46 g of EDTA into a bottle (1L)
2. add about 80ml of deionized waster to the beaker
3. add a stir bar to the beaker and leave it on a stir plate until completely dissolved
4. add NaOH to raise pH to 6.6
5. add enough deionized water to 1L

1×PBS buffer (PBS 10mM):

1. Start with 800ml of deionized water
2. Add 8g of NaCl
3. Add 0.2 g of KCl
4. Add 1.44 g of Na_2HPO_4
5. Add 0.24g of KH_2PO_4
6. Adjust the pH to 7.4 with HCL
7. Add distilled water to a total volume of 1 Litter

1mM Mercaptoethanol solution:

1. Put 10mM HEPES and 5m EDTA buffer in bottle about 99 ml
2. Use pipette to add 0.993 ml

Use pipette to add Mercaptoethanol (14.3 M)about 0.007ml (7ul)

Appendix D

1. Fabrication recipe:

- **PECVD SiON Deposition**

Gases mixture: SiH_4 (20sccm) + NH_3 (20sccm) + N_2 (980) + N_2O (210)

Power : 40W (100kHz)

Chamber pressure : 750 mT

Temperature: 350 ˚C

Deposition rate: 0.37 nm/s

Refractive index: 1.69 at 800nm

Optical loss (633nm) : 0.2 dB/cm

- **RIE etching**

This recipe alternate between etching and cooling step for each cycle in order to avoid burning ZEP resist.

Gas mixture (etch cycle): Ar (25sccm) + CHF_3 (25sccm)

Cycle etching time: 30s

Gas mixture (cool cycle): N_2 (68sccm)

Cycle cooling time: 90s

RF power (etch cycle): 200W

Temperature: 18 ˚C

Number of cycles: 32

Full wafer (6 inch) etching rate: 4.17 nm/cycle

Appendix E

1. Rsoft 3D model

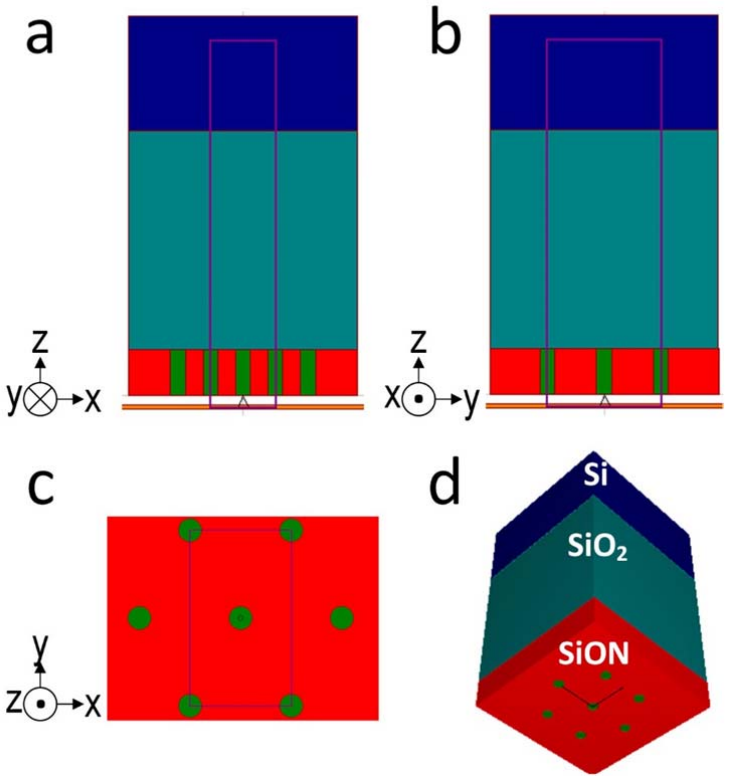

Figure 110 Rsoft 3D model of hexagonal lattice PCs for RCWA calculation

Figure 110 *shows the 3D Rsoft DiffractMOD model of a hexagonal lattice. The simulation window is depicted as purple lines and the boundary conditions are periodic along the x and y directions. The simulated incidence light wavelength was varied from 500nm to 900nm in 1nm increments. The incidence angle varied from 0° to 60° while the zero-order reflection was monitored. A key simulation parameter is the number of harmonics used to expand the refractive index and field in Fourier space. It was found that 5 harmonics achieved good refractive index resolution and resulted in reasonable simulationtime.*

References

[1] G. T. Reed, *Silicon photonics : the state of the art*. Wiley, 2008.

[2] D. Taillaert, P. Bienstman, and R. Baets, "Compact efficient broadband grating coupler for silicon-on-insulator waveguides.," *Opt. Lett.*, vol. 29, no. 23, pp. 2749–2751, 2004.

[3] D. Taillaert, F. Van Kaere, M. Ayre, W. Bogaerts, D. Van Thourhout, and P. bienstman and R. Baets, "Grating Couplers for Coupling between Optical Fibers and Nanophotonic Waveguides Grating Couplers for Coupling between Optical Fibers and Nanophotonic Waveguides," *J. Appl. Phys.*, vol. 45, no. 8A, pp. 6071–6077, 2006.

[4] N. Hattasan, B. Kuyken, F. Leo, E. Ryckeboer, D. Vermeulen, and G. Roelkens, "High-efficiency SOI fiber-to-chip grating couplers and low-loss waveguides for the short-wave infrared," *IEEE PHOTONICS Technol. Lett.*, vol. 24, no. 17, pp. 1536–1538, 2012.

[5] G. Roelkens *et al.*, "High efficiency diffractive grating couplers for interfacing a single mode optical fiber with a nanophotonic silicon-on-insulator waveguide circuit," *Appl. Phys. Lett.*, vol. 92, no. 13, pp. 131101, 2008.

[6] L. Gounaridis *et al.*, "Design of grating couplers and MMI couplers on the TriPleX platform enabling ultra-compact photonic-based biosensors," *Sensors Actuators B Chem.*, vol. 209, pp. 1057–1063, 2015.

[7] C. Li, H. Zhang, M. Yu, and G. Q. Lo, "CMOS-compatible high efficiency double-etched apodized waveguide grating coupler.," *Opt. Express*, vol. 21, no. 7, pp. 7868–74, 2013.

[8] Z. Cheng *et al.*, "Focusing subwavelength grating coupler for mid-infrared suspended membrane waveguide," *Opt. Lett.*, vol. 37, no. 7, pp. 1217–1219, 2012.

[9] L. B.Soldano and E. C. M. Pennings, "Optical Multi-Mode Interference Devices Based on Self-Imaging: Principles and Applications," *J. Light. Technol.*, vol. 13, no. 4, pp. 615–627, 1995.

[10] Z. Sheng *et al.*, "A Compact and Low-Loss MMI Coupler Fabricated With CMOS Technology," *IEEE Photonics J.*, vol. 4, no. 6, pp. 2272–2277, 2012.

[11] M. Tokushima, H. Kosaka, A. Tomita, and H. Yamada, "Lightwave propagation through a 120° sharply bent single-line-defect photonic crystal waveguide," *Appl. Phys. Lett.*, vol. 76, no. 8, pp. 952, 2000.

[12] M. Zhang, R. Malureanu, A. C. Krüger, and M. Kristensen, “1x3 beam splitter for TE polarization based on self-imaging phenomena in photonic crystal waveguides,” *Opt. Express*, vol. 18, no. 14, pp. 14944, 2010.

[13] D. Taillaert, H. Harold Chong, P. I. Borel, L. H. Frandsen, R. M. De La Rue, and R. Baets, “A compact two-dimensional grating coupler used as a polarization splitter,” *IEEE Photonics Technol. Lett.*, vol. 15, no. 9, pp. 1249–1251, 2003.

[14] L. Wu, M. Mazilu, J.-F. Gallet, T. F. Krauss, A. Jugessur, and R. M. De La Rue, “Planar photonic crystal polarization splitter,” *Opt. Lett.*, vol. 29, no. 14, pp. 1620, 2004.

[15] G. Manzacca, D. Paciotti, A. Marchese, M. S. Moreolo, and G. Cincotti, “2D photonic crystal cavity-based WDM multiplexer,” *Photonics Nanostructures - Fundam. Appl.*, vol. 5, no. 4, pp. 164–170, 2007.

[16] M. Lipson, “Guiding , Modulating , and Emitting Light on Silicon — Challenges and Opportunities,” *J. Light. Technol.*, vol. 23, no. 12, pp. 4222–4238, 2005.

[17] E. Yablonovitch, “Inhibited Spontaneous Emission in Solid-State Physics and Electronics,” vol. 58, no. 20, pp. 2059–2062, 1987.

[18] H. Yu *et al.*, “Ultracompact and high sensitive refractive index sensor based on Mach–Zehnder interferometer,” *Opt. Lasers Eng.*, vol. 56, pp. 50–53, 2014.

[19] K. Tiefenthaler and W. Lukosz, “Sensitivity of grating couplers as integrated-optical chemical sensors,” *J. Opt. Soc. Am. B*, vol. 6, no. 2, p. 209, 1989.

[20] A. Ramachandran *et al.*, “A universal biosensing platform based on optical micro-ring resonators,” *Biosens. Bioelectron.*, vol. 23, no. 7, pp. 939–944, 2008.

[21] R. Verma and B. D. Gupta, “Fiber optic SPR sensor for the detection of 3-pyridinecarboxamide (vitamin B3) using molecularly imprinted hydrogel,” *Sensors Actuators B Chem.*, vol. 177, pp. 279–285, 2013.

[22] F. Ciruela, “Fluorescence-based methods in the study of protein-protein interactions in living cells.,” *Curr. Opin. Biotechnol.*, vol. 19, no. 4, pp. 338–43, 2008.

[23] W. Liang, Y. Huang, Y. Xu, R. K. Lee, and A. Yariv, “Highly sensitive fiber Bragg grating refractive index sensors,” *Appl. Phys. Lett.*, vol. 86, no. 15, pp. 151122, 2005.

[24] T. Endo, K. Kerman, N. Nagatani, Y. Takamura, and E. Tamiya, “Label-Free Detection of Peptide Nucleic Acid - DNA Hybridization Using Localized Surface Plasmon Resonance Based Optical Biosensor,” *Anal. Chem.*, vol. 77, no. 21, pp. 6976–6984, 2005.

[25] K. E. Shafer-Peltier, C. L. Haynes, M. R. Glucksberg, and R. P. Van Duyne, “Toward a glucose biosensor based on surface-enhanced Raman scattering.,” *J. Am. Chem. Soc.*, vol. 125, no. 2, pp. 588–93, 2003.

[26] F. Vollmer, D. Braun, A. Libchaber, M. Khoshsima, I. Teraoka, and S. Arnold, “Protein detection by optical shift of a resonant microcavity,” *Appl. Phys. Lett.*, vol. 80, no. 21, pp. 4057–4059, 2002.

[27] S. John, “Strong localization of photons in certain disordered dielectric superlattices.,” *Physical review letters*, vol. 58, no. 23. pp. 2486–2489, 08-Jun-1987.

[28] T. F. Krauss, R. De La Rue, and S. Brand, “two dimensional photonic bandgap structures operating at near infrared wavelengths,” *Lett. to Nat.*, pp. 699–702, 1996.

[29] R. P. Huebener, “Well Ordered Lattice Structures in Crystals,” Springer International Publishing , pp. 15–33, 2016

[30] J. John D, S. G.Johnson, W. Joshua N, and R. D.Meade, *Photonic Crystal-Molding the flow of light*. Princeton university press, 2008.

[31] J. John D, S. G.Johnson, W. Joshua N, and R. D.Meade , *Photonic crystals: molding the flow of light*. Princeton university press, 2008.

[32] Z. Ze and S. Sashi, “Electromagnetic Wave Propagation in Periodeic Structures：Bloch Wave Solution of Maxwell’s Equations,” *Phys. Rev. Lett.*, vol. 65, no. 21, pp. 2650–2653, 1990.

[33] M. Centini *et al.*, “Dispersive properties of finite, one-dimensional photonic band gap structures: Applications to nonlinear quadratic interactions,” *Phys. Rev. E*, vol. 60, no. 4, pp. 4891–4898, 1999.

[34] T. Hattori, N. Tsurumachi, and H. Nakatsuka, “Analysis of optical nonlinearity by defect states in one-dimensional photonic crystals,” *J. Opt. Soc. Am. B*, vol. 14, no. 2, pp. 348,.1997.

[35] K. Xu, X. Zheng, C. Li, and W. She, “Design of omnidirectional and multiple channeled filters using one-dimensional photonic crystals containing a defect layer with a negative refractive index,” *Phys. Rev. E*, vol. 71, no. 6, pp. 66604, 2005.

[36] a. Chelnokov, K. Wang, S. Rowson, P. Garoche, and J.-M. Lourtioz, "Near-infrared Yablonovite-like photonic crystals by focused-ion-beam etching of macroporous silicon," *Appl. Phys. Lett.*, vol. 77, no. 19, pp. 2943, 2000.

[37] M. de Dood, B. Gralak, a. Polman, and J. Fleming, "Superstructure and finite-size effects in a Si photonic woodpile crystal," *Phys. Rev. B*, vol. 67, no. 3, pp. 35322, 2003.

[38] J. S. King, E. Graugnard, and C. J. Summers, "TiO2 Inverse Opals Fabricated Using Low-Temperature Atomic Layer Deposition," *Adv. Mater.*, vol. 17, no. 8, pp. 1010–1013, 2005.

[39] T. Kondo, S. Matsuo, S. Juodkazis, and H. Misawa, "Femtosecond laser interference technique with diffractive beam splitter for fabrication of three-dimensional photonic crystals," *Appl. Phys. Lett.*, vol. 79, no. 6, pp. 725–727, 2001.

[40] S. Shoji and S. Kawata, "Photofabrication of three-dimensional photonic crystals by multibeam laser interference into a photopolymerizable resin," *Appl. Phys. Lett.*, vol. 76, no. 19, pp. 2668–2670, 2000.

[41] M. Qi *et al.*, "A three-dimensional optical photonic crystal with designed point defects," *Nature*, vol. 429, no. 6991, pp. 538–542, 2004.

[42] G. I. N. Waterhouse and M. R. Waterland, "Opal and inverse opal photonic crystals: Fabrication and characterization," *Polyhedron*, vol. 26, no. 2, pp. 356–368, 2007.

[43] S. Y. Lin *et al.*, "A three-dimensional photonic crystal operating at infrared wavelengths," *Nature*, vol. 394, no. 6690, pp. 251–253, 1998.

[44] D. Shechtman, I. Blech, D. Gratias, and J. W. Cahn, "Metallic Phase with Long-Range Orientational Order and No Translational Symmetry," *Phys. Rev. Lett.*, vol. 53, no. 20, pp. 1951–1953, 1984.

[45] IUC, "International Union of Crystallography," *Int. Work. Magn. Magn. Mater. Their Appl. Thirteen. Eur. Crystallogr. Meet.*, vol. 48, no. 12, pp. 922–946, 1992.

[46] Y. S. Chan, C. T. Chan, and Z. Y. Liu, "Photonic Band Gaps in Two Dimensional Photonic Quasicrystals," *Phys. Rev. Lett.*, vol. 80, no. 5, pp. 956–959, 1998.

[47] C. Jin, B. Cheng, B. Man, Z. Li, and D. Zhang, "Two-dimensional dodecagonal and decagonal quasiperiodic photonic crystals in the microwave region," *Phys. Rev. B*, vol. 61, no. 16, pp. 10762–10767, 2000.

[48] M. E. Z. Jeremy J. Baumberg, Martin D. B. Charlton, Maria C. Netti, Gregory J. Parker, “Optical device,” 2001.

[49] M. E. Pollard, G. J. Parker, and M. D. B. Charlton, “Photonic band gaps of increasingly isotropic crystals at high dielectric contrasts,” in *Proc.of SPIE*, 2012, p. 82690W.

[50] F. Karim and A. N. M. Fakhruddin, “Recent advances in the development of biosensor for phenol: a review,” *Rev. Environ. Sci. Bio/Technology*, vol. 11, no. 3, pp. 261–274, 2012.

[51] S. P. Mohanty and E. Kougianos, “Biosensors: a tutorial review,” *IEEE Potentials*, vol. 25, no. 2, pp. 35–40, 2006.

[52] J. Wang, “DNA biosensors based on Peptide Nucleic Acid (PNA) recognition layers. A review,” *Biosens. Bioelectron.*, vol. 13, no. 7–8, pp. 757–762, 1998.

[53] U. Guth, W. Vonau, and J. Zosel, “Recent developments in electrochemical sensor application and technology—a review,” *Meas. Sci. Technol.*, vol. 20, no. 4, pp. 42002, 2009.

[54] U. Yogeswaran and S.-M. Chen, “A Review on the Electrochemical Sensors and Biosensors Composed of Nanowires as Sensing Material,” *Sensors*, vol. 8, no. 1, pp. 290–313, 2008.

[55] D. Lakshmi *et al.*, “Electrochemical Sensor for Catechol and Dopamine Based on a Catalytic Molecularly Imprinted Polymer-Conducting Polymer Hybrid Recognition Element,” *Anal. Chem.*, vol. 81, no. 9, pp. 3576–3584, 2009.

[56] X. Fan, I. M. White, S. I. Shopova, H. Zhu, J. D. Suter, and Y. Sun, “Sensitive optical biosensors for unlabeled targets: A review,” *Anal. Chim. Acta*, vol. 620, no. 1–2, pp. 8–26, 2008.

[57] X. D. Hoa, A. G. Kirk, and M. Tabrizian, “Towards integrated and sensitive surface plasmon resonance biosensors: A review of recent progress,” *Biosens. Bioelectron.*, vol. 23, no. 2, pp. 151–160, 2007.

[58] M. N. Velasco-Garcia, “Optical biosensors for probing at the cellular level: A review of recent progress and future prospects,” *Semin. Cell Dev. Biol.*, vol. 20, no. 1, pp. 27–33, 2009.

[59] Ron Blonder, Eugenii Katz, Yael Cohen, Norbert Itzhak, and Azalia Riklin, and I. Willner, “Application of Redox Enzymes for Probing the Antigen−Antibody Association at Monolayer Interfaces: Development of Amperometric Immunosensor Electrodes,” Anal. Chem. vol. 68, no.18, 68, pp. 3151–3157, 1996.

[60] E. Katz and I. Willner, “Amperometric amplification of antigen-antibody association at monolayer interfaces: design of immunosensor electrodes,” *J. Electroanal. Chem.*, vol. 418, no. 1–2, pp. 67–72, 1996.

[61] T. R. J. Holford, F. Davis, and S. P. J. Higson, “Recent trends in antibody based sensors,” *Biosens. Bioelectron.*, vol. 34, no. 1, pp. 12–24, 2012.

[62] P. B. Luppa, L. J. Sokoll, and D. W. Chan, “Immunosensors--principles and applications to clinical chemistry.,” *Clin. Chim. Acta.*, vol. 314, no. 1–2, pp. 1–26, 2001.

[63] D. R. Thévenot, K. Toth, R. A. Durst, and G. S. Wilson, “Electrochemical biosensors: recommended definitions and classification,” *Biosens. Bioelectron.*, vol. 16, no. 1–2, pp. 121–131, 2001.

[64] C. Lau, S. Reiter, W. Schuhmann, and P.Gründler , “Application of heated electrodes operating in a non-isothermal mode for interference elimination with amperometric biosensors,” *Anal. Bioanal. Chem.*, vol. 379, no. 2, pp. 255–260, 2004.

[65] B.Y. Wu *et al.*, “Amperometric glucose biosensor based on layer-by-layer assembly of multilayer films composed of chitosan, gold nanoparticles and glucose oxidase modified Pt electrode,” *Biosens. Bioelectron.*, vol. 22, no. 6, pp. 838–844, 2007.

[66] I. Wlllner and A. Rlklln, “Electrical Communication between Electrodes and NAD(P)+-Dependent Enzymes Using Pyrroloquinolinequinone-Enzyme Electrodes in a Self-Assembled Monolayer Configuration: Design of a New Class of Amperometric Biosensors,” *Anal. Chem*, vol. 66, pp. 1535–1539, 1994.

[67] A. Salimi, R. G. Compton, and R. Hallaj, “Glucose biosensor prepared by glucose oxidase encapsulated sol-gel and carbon-nanotube-modified basal plane pyrolytic graphite electrode,” *Anal. Biochem.*, vol. 333, no. 1, pp. 49–56, 2004.

[68] N. C. Foulds and C. R. Lowe, “Enzyme entrapment in electrically conducting polymers. Immobilisation of glucose oxidase in polypyrrole and its application in amperometric glucose sensors,” *J. Chem. Soc. Faraday Trans. Phys. Chem. Condens. Phases*, vol. 82, no. 4, pp.1259, 1986.

[69] S. Chen, J. G. Bomer, E. T. Carlen, and A. van den Berg, “Al $_2$ O $_3$ Silicon Nano ISFET with Near Ideal Nernstian Response,” *Nano Lett.*, vol. 11, no. 6, pp. 2334–2341, 2011.

[70] L. Bousse, S. Mostarshed, B. van der Schoot, and N. F. de Rooij, “Comparison of the hysteresis of Ta_2O_5 and Si_3N_4 pH-sensing insulators,” *Sensors Actuators B Chem.*, vol. 17, no. 2, pp. 157–164, 1994.

[71] M. J. Schöning and A. Poghossian, “Recent advances in biologically sensitive field-effect transistors (BioFETs).,” *Analyst*, vol. 127, no. 9, pp. 1137–1151, 2002.

[72] A. A. Shul, ga *et al.*, “Operation of an ISFET with non-insulated substrate directly exposed to the solution,” *Sensors Actuators B Chem.*, vol. 30, no. 2, pp. 101–105, 1996.

[73] P. G. Glavina A N D D Jed Harrison, P. G. Glavina, and D. Jed Harrison, “Preparation of integrated chemical sensors using commercial VLSI technology,” *J. Chem*, vol. 65, pp. 1072, 1987.

[74] J. A. Lee, S. Hwang, J. Kwak, S. Il Park, S. S. Lee, and K.-C. Lee, “An electrochemical impedance biosensor with aptamer-modified pyrolyzed carbon electrode for label-free protein detection,” *Sensors Actuators B Chem.*, vol. 129, no. 1, pp. 372–379, 2008.

[75] W. Lorenz, “Zur anwendung der transformations—impedanzspektrometrie,” *J. Electroanal. Chem.*, vol. 65, no. 1, pp. 141–153, Oct. 1975.

[76] X. Luo and J. J. Davis, “Electrical biosensors and the label free detection of protein disease biomarkers.,” *Chem. Soc. Rev.*, vol. 42, no. 13, pp. 5944–62, 2013.

[77] E. Tully, S. P. Higson, and R. O’Kennedy, “The development of a ‘labeless’ immunosensor for the detection of Listeria monocytogenes cell surface protein, Internalin B,” *Biosens. Bioelectron.*, vol. 23, no. 6, pp. 906–912, 2008.

[78] F. Khoshnoud and C. W. de Silva, “Recent advances in MEMS sensor technology – biomedical applications,” *IEEE Instrum. Meas. Mag.*, vol. 15, no. 1, pp. 8–14, Feb. 2012.

[79] R. E. Fernandez, S. Stolyarova, A. Chadha, E. Bhattacharya, and Y. Nemirovsky, “MEMS Composite Porous Silicon/Polysilicon Cantilever Sensor for Enhanced Triglycerides Biosensing,” *IEEE Sens. J.*, vol. 9, no. 12, pp. 1660–1666, 2009.

[80] Chun-Hao Chen *et al.*, “A Wireless Bio-MEMS Sensor for C-Reactive Protein Detection Based on Nanomechanics,” *IEEE Trans. Biomed. Eng.*, vol. 56, no. 2, pp. 462–470, 2009.

[81] P. D. Patel, “(Bio)sensors for measurement of analytes implicated in food safety: A review,” *TrAC - Trends Anal. Chem.*, vol. 21, no. 2, pp. 96–115, 2002.

[82] F. Tong, Y. Lian, H. Zhou, X. Shi, and F. He, “Multichannel Series Piezoelectric Quartz Crystal Cell Sensor for Real Time and Quantitative Monitoring of the Living Cell and Assessment of Cytotoxicity,” *Anal. Chem.*, vol. 86, no. 20, pp. 10415–10421, 2014.

[83] J. Homola, S. S. Yee, and G. Gauglitz, “Surface plasmon resonance sensors: review,” *Sensors Actuators B Chem.*, vol. 54, no. 1, pp. 3–15, 1999.

[84] B. Lee, “Review of the present status of optical fiber sensors,” *Opt. Fiber Technol.*, vol. 9, no. 2, pp. 57–79, 2003.

[85] M. Li, S. K. Cushing, and N. Wu, “Plasmon-enhanced optical sensors: a review,” *Analyst*, vol. 140, pp. 386–406, 2014.

[86] S. Y. Lee *et al.*, “Water-resistant flexible GaN LED on a liquid crystal polymer substrate for implantable biomedical applications,” *Nano Energy*, vol. 1, no. 1, pp. 145–151, 2012.

[87] M. Shahzad *et al.*, “Infrared surface plasmons on heavily doped silicon,” *J. Appl. Phys.*, vol. 110, no. 12, pp. 123105, 2011.

[88] H. W. Choi, Y. Sakata, Y. Kurihara, T. Ooya, and T. Takeuchi, “Label-free detection of C-reactive protein using reflectometric interference spectroscopy-based sensing system,” *Anal. Chim. Acta*, vol. 728, pp. 64–68, 2012.

[89] Oliver Birkert, Rolf Tünnemann, and Günther Jung, and G. Gauglitz, “Label-Free Parallel Screening of Combinatorial Triazine Libraries Using Reflectometric Interference Spectroscopy,” Anal. Chem., vol.74, no.4, pp.834-840, 2002.

[90] Matthias Sauer *et al.*, “Interaction of Chemically Modified Antisense Oligonucleotides with Sense DNA: A Label-Free Interaction Study with Reflectometric Interference Spectroscopy,” Anal. Chem., Vol.71, pp.2850-2857,1999.

[91] Aurel Ymeti *et al.*, “Fast, Ultrasensitive Virus Detection Using a Young Interferometer Sensor,” Nano Lett , vol.7, pp. 394-397, 2007.

[92] Z. Qi, S. Zhao, F. Chen, and S. Xia, “Integrated Young interferometer sensor with a channel-planar composite waveguide sensing arm,” *Opt. Lett.*, vol. 34, no. 14, pp. 2213, 2009.

[93] K. Schmitt, B. Schirmer, C. Hoffmann, A. Brandenburg, and P. Meyrueis, “Interferometric biosensor based on planar optical waveguide sensor chips for label-free detection of surface bound bioreactions,” *Biosens. Bioelectron.*, vol. 22, no. 11, pp. 2591–2597, 2007.

[94] M. A. Brusatori and P. R. Van Tassel, “Biosensing under an applied voltage using optical waveguide lightmode spectroscopy,” *Biosens. Bioelectron.*, vol. 18, no. 10, pp. 1269–1277, 2003.

[95] T. . Hug, J. . Prenosil, and M. Morbidelli, “Optical waveguide lightmode spectroscopy as a new method to study adhesion of anchorage-dependent cells as an indicator of metabolic state,” *Biosens. Bioelectron.*, vol. 16, no. 9, pp. 865–874, 2001.

[96] E. Németh, N. Adányi, A. Halász, M. Váradi, and I. Szendrő, “Real-time study of the effect of different stress factors on lactic acid bacteria by electrochemical optical waveguide lightmode spectroscopy,” *Biomol. Eng.*, vol. 24, no. 6, pp. 631–637, 2007.

[97] P. H. Paul and G. Kychakoff, “Fiber-optic evanescent field absorption sensor,” *Appl. Phys. Lett.*, vol. 51, no. 1, pp. 12–14, 1987.

[98] A. Banerjee *et al.*, “Fiber optic sensing of liquid refractive index,” *Sensors Actuators B Chem.*, vol. 123, no. 1, pp. 594–605, 2007.

[99] J. Melendez *et al.*, “A commercial solution for surface plasmon sensing,” *Sensors Actuators B Chem.*, vol. 35, pp. 212–216, 1996.

[100] X. Jiang *et al.*, “Immunosensors for detection of pesticide residues,” *Biosens. Bioelectron.*, vol. 23, no. 11, pp. 1577–1587, 2008.

[101] H. Yu *et al.*, “Ultracompact and high sensitive refractive index sensor based on Mach – Zehnder interferometer,” *Opt. Lasers Eng.*, vol. 56, pp. 50–53, 2014.

[102] G. Veronis and S. Fan, “Bends and splitters in metal-dielectric-metal subwavelength plasmonic waveguides,” *Appl. Phys. Lett.*, vol. 87, no. 13, pp. 131102, 2005.

[103] P. Leonard *et al.*, “Advances in biosensors for detection of pathogens in food and water,” *Enzyme Microb. Technol.*, vol. 32, no. 1, pp. 3–13, 2003.

[104] R. Jha and A. K. Sharma, “High-performance sensor based on surface plasmon resonance with chalcogenide prism and aluminum for detection in infrared.,” *Opt. Lett.*, vol. 34, no. 6, pp. 749–51, 2009.

[105] O. R. Bolduc, L. S. Live, and J.-F. Masson, “High-resolution surface plasmon resonance sensors based on a dove prism,” *Talanta*, vol. 77, no. 5, pp. 1680–1687, 2009.

[106] J. Ladd, A. D. Taylor, J. Homola, and S. Jiang, “Detection of botulinum neurotoxins in buffer and honey using a surface plasmon resonance (SPR) sensor,” *Sensors Actuators B Chem.*, vol. 130, no. 1, pp. 129–134, 2008.

[107] J. Dostálek *et al.*, “Surface plasmon resonance biosensor based on integrated optical waveguide,” *Sensors Actuators B Chem.*, vol. 76, no. 1, pp. 8–12, 2001.

[108] C. R. Lavers and J. S. Wilkinson, “A waveguide-coupled surface-plasmon sensor for an aqueous environment,” *Sensors Actuators B Chem.*, vol. 22, no. 1, pp. 75–81, 1994.

[109] A. Suzuki, J. Kondoh, Y. Matsui, S. Shiokawa, and K. Suzuki, “Development of novel optical waveguide surface plasmon resonance (SPR) sensor with dual light emitting diodes,” *Sensors Actuators B Chem.*, vol. 106, no. 1, pp. 383–387, 2005.

[110] E. Brynda, “Novel spectral fiber optic sensor based on surface plasmon resonance,” *Sens. Actuators*, vol. 74, pp. 106–111, 2001.

[111] J. Dostálek, J. Homola, and M. Miler, “Rich information format surface plasmon resonance biosensor based on array of diffraction gratings,” *Sensors Actuators B Chem.*, vol. 107, no. 1, pp. 154–161, 2005.

[112] C. Valsecchi and A. G. Brolo, “Periodic metallic nanostructures as plasmonic chemical sensors,” *Langmuir*, vol. 29, no. 19, pp. 5638–5649, 2013.

[113] Michelle A. Brusatori, and Yanrong Tie, and P. R. Van Tassel, “Protein Adsorption Kinetics under an Applied Electric Field: An Optical Waveguide Lightmode Spectroscopy Study,” *Langmuir*, vol. 19, pp. 5089–5097, 2003.

[114] N. J. Tao, S. Boussaad, W. L. Huang, R. a. Arechabaleta, and J. D’Agnese, “High resolution surface plasmon resonance spectroscopy,” *Rev. Sci. Instrum.*, vol. 70, no. 12, pp. 4656, 1999.

[115] G. a J. Besselink, R. P. H. Kooyman, P. J. H. J. Van Os, G. H. M. Engbers, and R. B. M. Schasfoort, “Signal amplification on planar and gel-type sensor surfaces in surface plasmon resonance-based detection of prostate-specific antigen,” *Anal. Biochem.*, vol. 333, pp. 165–173, 2004.

[116] A. D. Taylor, Q. Yu, S. Chen, J. Homola, and S. Jiang, “Comparison of E. coli O157:H7 preparation methods used for detection with surface plasmon resonance sensor,” *Sensors Actuators, B Chem.*, vol. 107, pp. 202–208, 2005.

[117] “SPR label-free analysis - GE Healthcare Life Sciences.” [Online]. Available: https://www.gelifesciences.com/en/gb/shop/protein-analysis/spr-label-free-analysis. [Accessed: 07-Mar-2018].

[118] P. V. Lambeck and R. V. Heideman, “Remote opto-chemical sensing with extreme sensitivity: Design, fabrication and performance of a pigtailed integrated optical phase-modulated Mach-Zehnder interferometer system,” *Sensors Actuators, B Chem.*, vol. 61, pp. 100–127, 1999.

[119] a. Brandenburg, “Differential refractometry by an integrated-optical Young interferometer,” *Sensors Actuators B Chem.*, vol. 39, no. 1–3, pp. 266–271, 1997.

[120] V. S. Lin, K. Motesharei, K. P. Dancil, M. J. Sailor, and M. R. Ghadiri, “A porous silicon-based optical interferometric biosensor.,” *Science* , vol. 278, no. 5339, pp. 840–843, 1997.

[121] “ForteBio Octet RED96e System.” [Online]. Available: https://www.fortebio.com/octet-RED96e.html. [Accessed: 07-Mar-2018].

[122] H. J. Watts, C. R. Lowe, and D. V Pollard-Knight, “Optical biosensor for monitoring microbial cells.,” *Anal. Chem.*, vol. 66, no. 15, pp. 2465–2470, 1994.

[123] N. Skivesen, R. Horvath, S. Thinggaard, N. B. Larsen, and H. C. Pedersen, “Deep-probe metal-clad waveguide biosensors,” *Biosens. Bioelectron.*, vol. 22, no. 7, pp. 1282–1288, 2007.

[124] R. Horváth, H. C. Pedersen, N. Skivesen, D. Selmeczi, and N. B. Larsen, “Optical waveguide sensor for on-line monitoring of bacteria.,” *Opt. Lett.*, vol. 28, no. 14, pp. 1233–1235, 2003.

[125] K. Schroeder, W. Ecke, R. Mueller, R. Willsch, and A. Andreev, “A fibre Bragg grating refractometer,” *Meas. Sci. Technol.*, vol. 12, no. 7, pp. 757–764, 2001.

[126] H. Tazawa, T. Kanie, and M. Katayama, “Fiber-optic coupler based refractive index sensor and its application to biosensing,” *Appl. Phys. Lett.*, vol. 91, no. 11, pp. 113901, 2007.

[127] L. B. Soldano and E. C. M. Pennings, “Optical multi-mode interference devices based on self-imaging: principles and applications,” *J. Light. Technol.*, vol. 13, no. 4, pp. 615–627, 1995.

[128] C. Hsu, S. Member, H. Chen, and W. Wang, “Compact Y -Branch Power Splitter Based on Simplified Coherent Coupling,” *IEEE PHOTONICS THECHNOLOGY Lett.*, vol. 15, no. 8, pp. 1103–1105, 2003.

[129] K. K. Chung, H. P. Chan, and P. L. Chu, “A 1×4 polarization and wavelength independent optical power splitter based on a novel wide-angle low-loss Y-junction,” *Opt. Commun.*, vol. 267, no. 2, pp. 367–372, 2006.

[130] S. H. Tao, Q. Fang, J. F. Song, M. B. Yu, G. Q. Lo, and D. L. Kwong, “Cascade wide-angle Y-junction 1 x 16 optical power splitter based on silicon wire waveguides on silicon-on-insulator.,” *Opt. Express*, vol. 16, no. 26, pp. 21456–21461, 2008.

[131] T. F. Krauss, “Planar photonic crystal waveguide devices for integrated optics,” *Phys. status solidi*, vol. 197, no. 3, pp. 688–702, 2003.

[132] S. J. Pearce, M. E. Pollard, S. Z. Oo, R. Chen, and M. D. B. Charlton, “Nanostructured surface enhanced Raman scattering sensor platform with integrated waveguide core,” *Appl. Phys. Lett.*, vol. 105, no. 18, p. 181101, Nov. 2014.

[133] L. Yang, B. Yan, W. R. Premasiri, L. D. Ziegler, L. D. Negro, and B. M. Reinhard, “Engineering Nanoparticle Cluster Arrays for Bacterial Biosensing: The Role of the Building Block in Multiscale SERS Substrates,” *Adv. Funct. Mater.*, vol. 20, no. 16, pp. 2619–2628, 2010.

[134] L. Erwin, *Loewen Diffraction Grating Handbook*. 2005.

[135] M. G. Moharam and T. K. Gaylord, “Diffraction analysis of dielectric surface-relief gratings,” *J. Opt. Soc. Am.*, vol. 72, no. 10, pp. 1385, 1982.

[136] C. I. Aguirre, E. Reguera, and A. Stein, “Tunable Colors in Opals and Inverse Opal Photonic Crystals,” *Adv. Funct. Mater.*, vol. 20, no. 16, pp. 2565–2578, 2010.

[137] G. J. Parker, M. E. Zoorob, M. D. B. Charlton, J. J. Baumberg, and M. C. Netti, “Complete photonic bandgaps in 12-fold symmetric quasicrystals,” *Nature*, vol. 404, no. 6779, pp. 740–743, 2000.

[138] H. Sai, Y. Kanamori, K. Arafune, Y. Ohshita, and M. Yamaguchi, “Light trapping effect of submicron surface textures in crystalline Si solar cells,” *Prog. Photovoltaics Res. Appl.*, vol. 15, no. 5, pp. 415–423, Aug. 2007.

[139] M. G. Moharam and T. K. Gaylord, “Rigorous coupled-wave analysis of planar-grating diffraction,” *J. Opt. Soc. Am.*, vol. 71, no. 7, pp. 811, 1981.

[140] M. A. Kaliteevski, S. Brand, R. A. Abram, T. F. Krauss, R. DeLa Rue, and P. Millar, “Two-dimensional Penrose-tiled photonic quasicrystals: from diffraction pattern to band structure,” *Nanotechnology*, vol. 11, no. 4, pp. 274–280, 2000.

[141] R. Magnusson *et al.*, "Photonic devices enabled by waveguide-mode resonance effects in periodically modulated films," in *SPIE proceeding*, 2003, pp. 20–34.

[142] A. Mekis *et al.*, "A Grating-Coupler-Enabled CMOS Photonics Platform," *IEEE J. Sel. Top. Quantum Electron.*, vol. 17, no. 3, pp. 597–608, 2011.

[143] Y. Nazirizadeh *et al.*, "Sensitivity optimization of injection-molded photonic crystal slabs for biosensing applications," *Opt. Mater. Express*, vol. 3, no. 5, pp. 556, 2013.

[144] X. Wei and S. M. Weiss, "Guided mode biosensor based on grating coupled porous silicon waveguide.," *Opt. Express*, vol. 19, no. 12, pp. 11330, 2011.

[145] W. Lukosz and K. Tiefenthaler, "Sensitivity of integrated optical grating and prism couplers as (bio)chemical sensors," *Sensors and Actuators*, vol. 15, no. 3, pp. 273–284, 1988.

[146] A. Brandenburg and A. Gombert, "Grating couplers as chemical sensors: a new optical configuration," *Sensors Actuators B Chem.*, vol. 17, no. 1, pp. 35–40, 1993.

[147] S. Grego, A. M. Patel, B. R. Stoner, Y. Cao, and T. J. Suleski, "Novel grating-based optical waveguide device for sensor applications," Proc. of SPIE, vol. 6218, 621810-1, 2006.

[148] E. Hallynck and P. Bienstman, "Photonic crystal biosensor based on angular spectrum analysis," *Opt. Express*, vol. 18, no. 17, pp. 18164, 2010.

[149] W. Lukosz, T. . Brenner, V. Briauet, P. M. Nellen, and P. Zeller, "Output Grating Couplers On Planar Waveguides As Integrated Optical Sensors," Sensor and Actuators B: 1989, pp.585-588, 1990.

[150] A. Mekis, A. Dodabalapur, R. E. Slusher, and J. D. Joannopoulos, "Two-dimensional photonic crystal couplers for unidirectional light output.," *Opt. Lett.*, vol. 25, no. 13, pp. 942–944, 2000.

[151] N. Kaneda, B. Houshmand, and T. Itoh, "FDTD analysis of dielectric resonators with curved surfaces," *IEEE Trans. Microw. Theory Tech.*, vol. 45, no. 9, pp. 1645–1649, 1997.

[152] Q. Liu *et al.*, "Mach-Zehnder interferometer (MZI) point-of-care system for rapid multiplexed detection of microRNAs in human urine specimens," *Biosens. Bioelectron.*, vol. 71, pp. 365–372, 2015.

[153] C. Biosensors, L. L. Chan, M. Pineda, J. T. Heeres, P. J. Hergenrother, and B. T. Cunningham, "A General Method for Discovering Inhibitors of Protein-DNA Interactions Using Photonic Crystal Biosensors," vol. 3, no. 7, pp. 437–448, 2008.

[154] D. J. Sirbuly, A. Tao, M. Law, R. Fan, and P. Yang, “Multifunctional Nanowire Evanescent Wave Optical Sensors,” *Adv. Mater.*, vol. 19, no. 1, pp. 61–66, 2007.

[155] B. A. Sexton, B. N. Feltis, and T. J. Davis, “Characterisation of gold surface plasmon resonance sensor substrates,” *Sensors Actuators A Phys.*, vol. 141, no. 2, pp. 471–475, 2008.

[156] S. M. George, “Atomic Layer Deposition: An Overview,” *Chem. Rev.*, vol. 110, no. 1, pp. 111–131, 2010.

[157] R. De Palma *et al.*, “Formation of dense self-assembled monolayers of (n-decyl)trichlorosilanes on Ta/Ta2O5,” *Langmuir*, vol. 23, no. 2, pp. 443–451, 2007.

[158] D. D. K. Schwartz, “Mechanisms and kinetics of self-assembled monolayer formation,” *Annu. Rev. Phys. Chem.*, vol. 52, pp. 107–137, 2001.

[159] J. Xiang, P. Zhu, Y. Masuda, and K. Koumoto, “Fabrication of self-assembled monolayers (SAMs) and inorganic micropattern on flexible polymer substrate.,” *Langmuir*, vol. 20, no. 8, pp. 3278–83, 2004.

[160] Y. Wang and M. Lieberman, “Growth of ultrasmooth octadecyltrichlorosilane self-assembled monolayers on SiO2,” *Langmuir*, vol. 19, no. 4, pp. 1159–1167, 2003.

[161] J. Wang, “SURVEY AND SUMMARY: From DNA biosensors to gene chips,” *Nucleic Acids Res.*, vol. 28, no. 16, pp. 3011–3016, 2000.

[162] A. N. Chryssis, S. S. Saini, S. M. Lee, Hyunmin Yi, W. E. Bentley, and M. Dagenais, “Detecting hybridization of DNA by highly sensitive evanescent field etched core fiber Bragg grating sensors,” *IEEE J. Sel. Top. Quantum Electron.*, vol. 11, no. 4, pp. 864–872, 2005.

[163] L. Chrisey, G. U. Lee, and C. E. O’Ferrall, “Covalent attachment of synthetic DNA to self-assembled monolayer films,” *Nucleic Acids Res.*, vol. 24, no. 15, pp. 3031–3039, 1996.

[164] R. G. Cotton, “Methods in clinical molecular genetics,” *Eur. J. Pediatr.*, vol. 159, no. S3, pp. S179–S182, 2000.

[165] E. Paleček, M. Fojta, M. Tomschik, and J. Wang, “Electrochemical biosensors for DNA hybridization and DNA damage,” *Biosens. Bioelectron.*, vol. 13, no. 6, pp. 621–628, 1998.

[166] P. Wu, P. Hogrebe, and D. W. Grainger, “DNA and protein microarray printing on silicon nitride waveguide surfaces,” *Biosens. Bioelectron.*, vol. 21, no. 7, pp. 1252–1263, Jan. 2006.

[167] S. Gon, B. Fang, and M. M. Santore, “Interaction of Cationic Proteins and Polypeptides with Biocompatible Cationically-Anchored PEG Brushes,” Macromolecules, vol.44, pp.8161-8168, 2011.

[168] L. De Stefano *et al.*, “Porous silicon-based optical microsensor for the detection of l-glutamine,” *Biosens. Bioelectron.*, vol. 21, no. 8, pp. 1664–1667, 2006.

[169] S. G. Patching, “Surface plasmon resonance spectroscopy for characterisation of membrane protein–ligand interactions and its potential for drug discovery,” *Biochim. Biophys. Acta - Biomembr.*, vol. 1838, no. 1, pp. 43–55, 2014.

[170] O. Tokel, F. Inci, and U. Demirci, “Advances in Plasmonic Technologies for Point of Care Applications,” *Chem. Rev.*, vol. 114, no. 11, pp. 5728–5752, 2014.

[171] W. M. bin M. Yunus and A. bin A. Rahman, “Refractive index of solutions at high concentrations,” *Appl. Opt.*, vol. 27, no. 16, pp. 3341, 1988.

[172] A. Nathan, S. Zalipsky, S. I. Ertel, S. N. Agathos, M. L. Yarmush, and J. Kohn, “Copolymers of Lysine and Polyethylene Glycol: A New Family of Functionalized Drug Carriers,” *Bioconjugate Chem*, vol. 4, pp. 54–62, 1993.

[173] S. Faraasen, M. Textor, H. P. Merkle, and E. Walter, “Ligand-Specific Targeting of Microspheres to Phagocytes by Surface Modification with Poly(L-Lysine)-Grafted Poly(Ethylene Glycol) Conjugate,” *Pharm. Res.*, vol. 20, no. 2, pp. 237–246, 2003.

[174] A. Garcia-Valenzuela, J. Gardner, and M. Tabib-Azar, “Improvement of the theoretical minimum detectable angle of the optical beam deflection method,”SPIE, vol.2686, pp. 146–156, 1996.

[175] “UV-Curable Hybrid Polymers for Micro Optical Components.” [Online]. Available: www.microresist.com. [Accessed: 29-Aug-2017].

[176] T. W. Odom, J. C. Love, D. B. Wolfe, K. E. Paul, and G. M. Whitesides, “Improved Pattern Transfer in Soft Lithography Using Composite Stamps.,” Langmuir , vol.18, pp.5314-5320,2002.